FEATURE ANALYSIS OF FUNCTIONAL MRI DATA FOR MAPPING EPILEPTIC NETWORKS

A Dissertation
Presented to
The Academic Faculty

By

Lauren S. Burrell

In Partial Fulfillment
Of the Requirements for the Degree
Doctor of Philosophy in the
School of Electrical and Computer Engineering

Georgia Institute of Technology
December 2008

FEATURE ANALYSIS OF FUNCTIONAL MRI DATA FOR MAPPING EPILEPTIC NETWORKS

Approved by:

Dr. George Vachtsevanos, Advisor
School of Electrical and Computer Engineering
Georgia Institute of Technology

Dr. Thomas Michaels
School of Electrical and Computer Engineering
Georgia Institute of Technology

Dr. Oskar Skrinjar
Wallace H. Coulter Department of Biomedical Engineering
Georgia Institute of Technology

Dr. Javier Echauz
BioQuantix Corporation

Dr. Anthony Yezzi
School of Electrical and Computer Engineering
Georgia Institute of Technology

Date Approved: September 5, 2008

To my parents and brother for their unconditional love and support throughout the years, without which I would have never made it this far.

ACKNOWLEDGEMENTS

I would like to thank my advisor Dr. George Vachtsevanos for his guidance during this process. I would also like to thank Dr. Brian Litt and Dr. Simon Glynn for providing insight into the medical aspects of this research. Additionally, I would like to thank the members of my dissertation committee, Dr. Oskar Skrinjar, Dr. Anthony Yezzi, Dr. Thomas Michaels, and Dr. Javier Echauz, for their comments and suggestions. Dr. Hiram Firpi, Dr. Andrew Gardner, and Dr. George Georgoulas have also provided insight and advice during this process.

My colleagues and friends in the Intelligent Control Systems Laboratory, Jacqueline Fairley, Otis Smart, and Matthew Wiggins have also helped by engaging in technical discussions with me and by just commiserating with me from time to time.

Last but certainly not least I would like to thank my parents, Leslie C. and Marlene Burrell without whom I would have never made it through graduate school. They have encouraged me every step of the way and have always believed that I could do it. Their love for me and confidence in me have enabled me to persevere when I did not think I could do it. I would also like to thank my big brother Sean who also listened to me complain when I was down and was there to bolster me when I needed it.

TABLE OF CONTENTS

LIST OF TABLES

LIST OF FIGURES

LIST OF ACRONYMS

AED	Antiepileptic Drug
ASL	Arterial Spin Labeling
AUC	Area Under the Curve
BOLD	Blood Oxygen Level Dependent
CASL	Continuous Arterial Spin Labeling
CBF	Cerebral Blood Flow
EEG	Electroencephalogram
FIM	Frequent Itemset Mining
fMRI	Functional Magnetic Resonance Imaging
GA	Genetic Algorithm
GLM	General Linear Model
GP	Genetic Programming
HRF	Hemodynamic Response Function
ICA	Independent Component Analysis
IED	Interictal Epileptiform Discharge
IEEG	Intracranial EEG
k-NN	*k*-Nearest Neighbor
MEG	Magnetoencephalography
MTL	Mesial Temporal Lobe
PCA	Principal Component Analysis
PDF	Probability Density Function
PET	Positron Emission Tomography
ROC	Receiver Operating Characteristic

ROI	Region of Interest
RTC	Reference Time Course
SNR	Signal-to-Noise Ratio
SPECT	Single Photon Emission Computed Tomography
SPM	Statistical Parametric Mapping
SVM	Support Vector Machine
TCA	Temporal Clustering Analysis
TLE	Temporal Lobe Epilepsy

SUMMARY

This research focused on the development of a methodology for analyzing functional magnetic resonance imaging (fMRI) data collected from patients with epilepsy in order to map epileptic networks. Epilepsy, a chronic neurological disorder characterized by recurrent, unprovoked seizures, affects up to 1% of the world's population. Antiepileptic drug therapies either do not successfully control seizures or have unacceptable side effects in over 30% of patients. Approximately one-third of patients whose seizures cannot be controlled by medication are candidates for surgical removal of the affected area of the brain, potentially rendering them seizure free. Accurate localization of the epileptogenic focus, i.e., the area of seizure onset, is critical for the best surgical outcome. Currently, the most widely used tool for localization of the epileptogenic zone is scalp electroencephalogram (EEG), which has high temporal resolution but suffers from poor spatial resolution. The investigation of fMRI data, which has superior spatial resolution, could potentially improve upon a clinician's ability to map the epileptic network.

The research presented in this dissertation aimed to develop a set of fMRI data features that could be used to distinguish between normal brain tissue and the epileptic focus. To determine the best combination of features from various domains for mapping the focus, genetic programming and several feature selection methods were employed. These composite features were subsequently used to train a classifier capable of discriminating between the two classes of voxels. The classifier was then applied to a separate testing set in order to generate maps showing brain voxels labeled as either

normal or epileptogenic based on the best feature or set of features. It should be noted that although this work focuses on the application of fMRI analysis to epilepsy data, similar techniques could be used when studying brain activations due to other sources.

In vivo data collected from temporal lobe epilepsy (TLE) patients and healthy controls were examined in this work. The resultant maps, which could not be assessed quantitatively because the true epileptic foci were unknown, were investigated qualitatively and compared to the suspected epileptic foci determined clinically. The maps were also compared to the foci found using 2dTCA (two-dimensional temporal clustering analysis), which also aims to identify areas of brain activations in fMRI without the need for simultaneous EEG data.

In addition to investigating in vivo data with uncertain epileptic foci, phantom (simulated) data were created and processed to provide quantitative measures of the efficacy of the techniques. The areas of activation in the generated maps were compared to the known regions of simulated activity. The results demonstrated the high accuracy with which the voxels embedded with simulated activations could be distinguished from those with only baseline activity and compared favorably with the 2dTCA generated maps. In fact, the methodology presented here was able to accurately map the areas of activation in cases where 2dTCA failed.

The contributions of this research include: (1) a novel feature-based methodology for localizing areas of brain activation in fMRI data that does not rely on knowledge of event timings like previously examined techniques; (2) selection and fusion of fMRI features from multiple domains for distinguishing between normal and epileptic activity; (3) demonstration of the ability to locate epileptic brain regions in fMRI data from

temporal lobe epilepsy patients using this novel method and comparison to the state of the art; and (4) validation of the system through the creation of a synthetic fMRI database with known areas of activation and application of the methodology to demonstrate its effectiveness.

CHAPTER 1

INTRODUCTION

1.1 Motivation

Epilepsy, a chronic neurological disorder characterized by recurrent, unprovoked seizures, affects approximately 1% of the world's population [1]. Epileptic seizures are caused by sudden bursts of electrical activity in the brain that disrupt normal brain function. These brief electrical disturbances can result in abnormal sensations, changes in awareness or behavior, loss of consciousness, and convulsions. Uncontrolled epilepsy can lead to depression, anxiety, and loss of cognitive function and is associated with higher national healthcare costs [2].

The most common form of treatment for epilepsy is antiepileptic drug (AED) therapy. For 30 to 40% of epilepsy patients, these AEDs either cannot effectively control seizures or have intolerable side effects [2]. Some patients for whom drug therapy is ineffective are candidates for resective surgery. These surgical candidates generally have seizures that originate in one specific area of the brain, which can then be removed and potentially end the seizures. Unfortunately, only 60 to 80% of patients are rendered seizure-free following surgical resection [3]. Implantable neurostimulation devices are another alternative to AEDs and are currently a hot area of study in epilepsy research. These devices directly stimulate the affected areas of the brain to stop the propagation of the abnormal electrical activity and prevent seizures. Both surgical and neurostimulation therapies rely on accurate localization of the areas of seizure onset in order for treatment to be effective.

Functional magnetic resonance imaging (fMRI) indirectly measures neural activity by monitoring changes in blood flow, blood oxygenation, and blood volume. This research focuses on analyzing fMRI data from epilepsy patients in order to localize the source of epileptic seizures, thereby potentially providing physicians an alternative to low-resolution scalp electroencephalogram (EEG) recordings and high-resolution, but highly invasive intracranial EEG for determining the origin of epileptic activity.

1.2 Problem Definition

Although epilepsy surgeries have been performed for well over a century, to date no noninvasive method exists for precisely defining the epileptogenic zone, i.e., the area of cortex requisite for epileptic seizure generation [4]. The primary objective of this research is to develop a feature-based fMRI voxel time series analysis technique for recognizing areas of epileptic activity in order to facilitate the mapping of epileptic networks. To this end, features are extracted from fMRI data and used to classify brain regions as either belonging to the epileptic network or not. In contrast to previous work in the area of epileptic focus localization using fMRI, this method is not dependent on the determination of the timing of individual epileptic events in order to perform standard statistical parametric mapping (SPM) analysis [5, 6], which locates the areas of brain activation through mass-univariate statistical tests. Instead this technique relies on finding features that characterize the abnormal activity and distinguish dysfunctional brain regions from healthy ones.

This work presents an integrated framework for preprocessing, feature extraction, feature fusion, and classification of fMRI data from epilepsy patients. This novel

methodology is validated through the analysis of synthetic fMRI data designed to resemble real data with embedded interictal activity. The examination of synthetic data is crucial because the true epileptogenic zones in the real data are unknown, so the efficacy of the techniques cannot be inferred from the investigation of real data alone. For the subjects involved in this study, all that is known about them is that they have suspected temporal lobe epilepsy. Exactly which parts of the temporal lobe are epileptogenic and whether or not there is epileptic activity in other brain regions is not certain. Analyzing synthetic data with known areas of activation allows for quantitative testing of the methodology and ensures that it is statistically rigorous. Additionally these methods will be compared with current standard approaches to fMRI analysis.

1.3 Methods Overview

Figure 1.1 provides a graphical representation of the system for localizing abnormal activity in resting fMRI data from epilepsy patients. Resting images are recorded while the subject is not performing any actions in the scanner. Resting data are studied in this work so that task related activations do not obscure the underlying spontaneous epileptic activity.

The system illustrated below includes three main steps: image preprocessing, feature extraction, and classification of the voxels. The raw images are initially preprocessed to reduce noise and remove artifacts. Physiological noise due to respiration and cardiac interference and scanner noise often mask signal changes due to brain activity and must be addressed before these signals can be analyzed. Once the signals have been enhanced, features are extracted from the voxel time series to define signal

characteristics capable of distinguishing epileptic and non-epileptic activity. These features are chosen from multiple domains including the time, frequency, statistical, and mutual information domains. Individual features as well as combinations of features are investigated for their abilities to discriminate between normal and epileptic activity. After the features are extracted from the images, they are used as inputs to a classifier to determine the locations of the epileptic activity. The final output of the system is an image highlighting the areas belonging to the epileptic network.

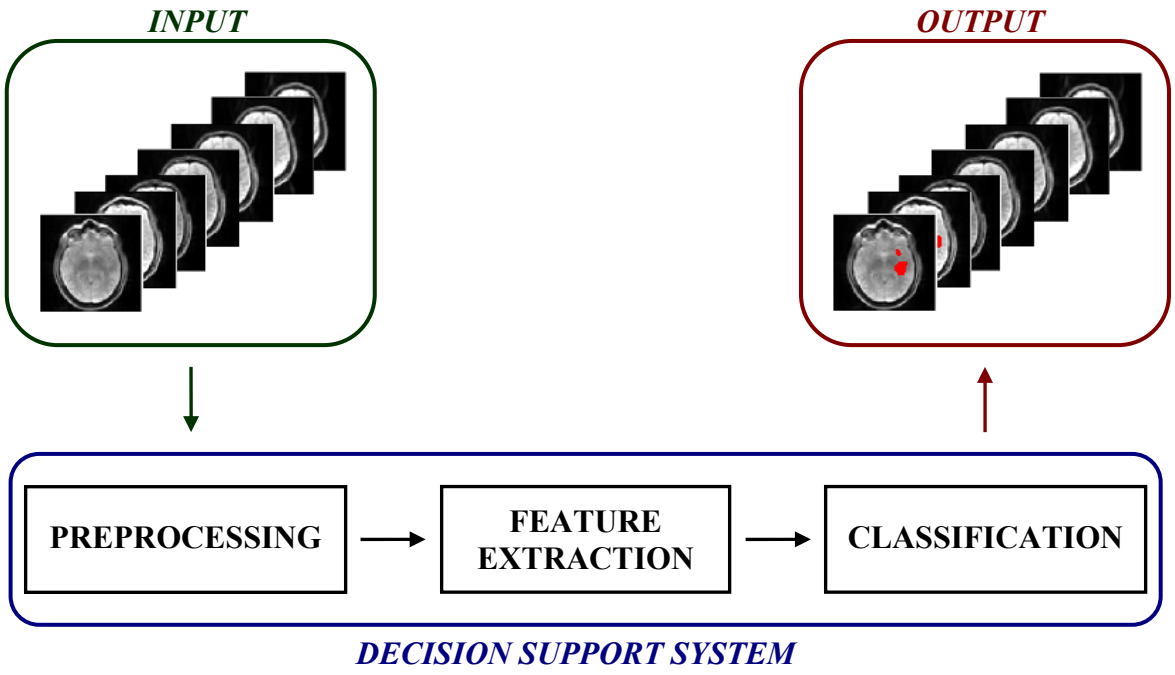

Figure 1.1 Diagram of the system for localizing epileptic activity in fMRI data. The input data are initially preprocessed to reduce noise and artifacts. Then features are extracted, and the brain regions are classified as normal or as containing epileptic activity. The output of the system is an image highlighting the dysfunctional areas.

1.4 Contributions

This research provides an architecture for identifying regions of epileptiform activity in the functional imaging data of epilepsy patients. The brain activity in resting fMRI data is characterized through feature analysis and then classified as normal or epileptic based on the feature values. Although this research focuses on the examination of fMRI data for localizing epileptic activity, the same methodology could be applied to any fMRI study. The contributions of this research include:

- A novel feature-based methodology for localizing areas of brain activation in fMRI data that does not rely on knowledge of event timings like previously examined techniques.
- Selection and fusion of fMRI features from multiple domains for distinguishing between normal and epileptic activity.
- Demonstration of the ability to locate epileptic brain regions in fMRI data from temporal lobe epilepsy patients using this novel method and comparison to the state of the art.
- Validation of the system through the creation of a synthetic fMRI database with known areas of activation and application of the methodology to demonstrate its effectiveness.

1.5 Organization of the Dissertation

Chapter 2 provides additional background information on epilepsy and treatment of this disorder. An overview of fMRI, EEG, and other functional neuroimaging tools

used in the diagnostic assessment of epilepsy patients is also provided. Finally, applications of these tools in previous research studies are reviewed.

Chapter 3 covers the research methodology in greater detail. Specifically, it discusses the image preprocessing steps, feature extraction, the choice of features for this application, and classification of the brain regions as healthy or dysfunctional based on these features.

Chapters 4 and 5 present the results of applying this methodology to synthetic fMRI data and real epilepsy patient data, respectively. These chapters also compare the results of this methodology to those obtained using conventional fMRI analysis techniques.

Finally, Chapter 6 provides concluding remarks and possible future extensions of this research.

CHAPTER 2

ORIGIN AND HISTORY OF THE PROBLEM

This chapter provides background information on epilepsy and reviews available therapies and standard neuroimaging tools used for patient assessment. It also presents a detailed review of the techniques that have been applied previously to the problem of epileptic focus localization. An emphasis is placed on the role of fMRI in this area.

2.1 Epilepsy

Epilepsy is the most prevalent neurological disorder in children and the third most prevalent in adults after strokes and Alzheimer's disease [7]. Recurrent, unprovoked seizures characterize epilepsy, which affects approximately 1% of the population worldwide. About 70% of epilepsy cases are idiopathic, meaning the origin of the condition is undetermined. Frequently identified causes in the remaining cases include brain tumors, stroke, head trauma, poisoning, substance abuse, infection, brain malformations, prenatal injuries, and genetic factors [7]. Although researchers have been able to identify causes of epilepsy, years of extensive study have failed to yield a consensus on the mechanisms underlying seizure generation.

2.1.1 Epileptic Seizures

Seizures are disturbances in brain function resulting from abnormal hypersynchronous discharging of cortical neurons. The physical manifestations of this abnormal firing vary depending on the location and extent of the brain tissue involved.

Symptoms of seizures include involuntary limb movements, peculiar sensations, lapses in awareness, loss of consciousness, unusual or repetitive behaviors, and convulsions. Seizures generally resolve themselves within a few seconds to a few minutes, but occasionally they can persist much longer. Thirty minutes or more of uninterrupted seizure activity is known as status epilepticus, which literally means continuous state of seizure [7]. Convulsive status epilepticus can lead to brain damage and even death and must be treated immediately.

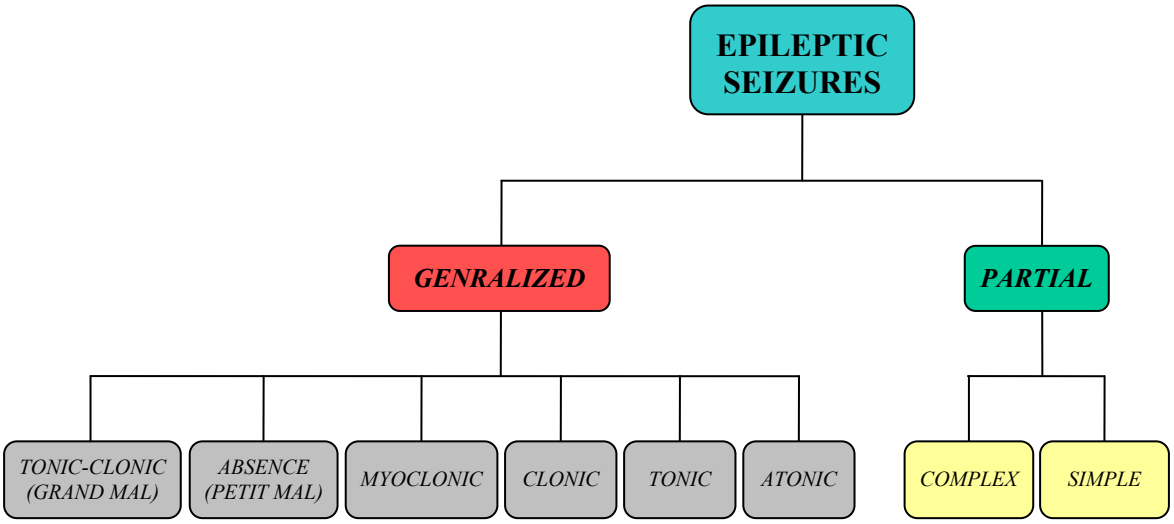

Figure 2.1 Epileptic seizure taxonomy defined by the International League Against Epilepsy in 1981.

The International League Against Epilepsy adopted the current system for classifying epileptic seizures in 1981 [8]. This system bases seizure classification on clinical and EEG observations and the extent of brain involvement. As shown in Figure 2.1, under this system all epileptic seizures fall into two main categories: generalized and partial seizures. Generalized seizures originate simultaneously on both sides of the brain,

while partial seizures are limited to a specific area of one hemisphere. Although partial seizures originate in a focal area of the brain, it is possible for them to spread to other brain regions, leading to a secondary generalized seizure.

Generalized seizures can be further divided into six major categories: tonic-clonic, absence, myoclonic, clonic, tonic, and atonic seizures. Tonic seizures are associated with stiffening of the limbs. Clonic seizures result in rhythmic, jerking movements often accompanied by impairment of consciousness. Myoclonic seizures are characterized by brief, arrhythmic jerking movements. Atonic seizures cause brief losses of muscle tone, often resulting in collapses and injuries. Absence seizures are lapses in awareness, often accompanied by staring, that last only a few seconds and begin and end abruptly. Finally, tonic-clonic seizures, the most common generalized seizures, consist of tonic phases followed by clonic phases.

Partial seizures can affect movement, emotions, and sensory functions. Complex partial seizures lead to the loss or impairment of consciousness during the event, while simple partial seizures do not. Partial seizures are the most common type experienced by epilepsy patients, including people with temporal lobe epilepsy (TLE), the syndrome under investigation in this research.

2.1.2 Epilepsy Therapy

The best course of treatment for an epilepsy patient depends on the nature of that person's epilepsy syndrome. Epileptic syndromes are classified based on seizure type, typical EEG patterns, clinical behavior, and the origin of the dysfunction, as well as other factors. In the majority of cases, the first course of treatment is antiepileptic drug (AED) therapy. Unfortunately, 30 to 40% of patients have intractable epilepsy—meaning their

seizures cannot be adequately controlled with medication—or suffer significant adverse reactions to the drugs [2]. In these cases, alternative methods of treatment must be considered. For instance, the ketogenic diet, which is very high in fats and low in carbohydrates and proteins, has proven effective in treating children with epilepsy [9].

Some patients with intractable partial seizures are candidates for surgery depending on the location of seizure onset. TLE, one of the most common epilepsy syndromes, is often amenable to surgery. In fact, resective surgery has been found to be superior to prolonged AED therapy in TLE patients [10]. Different sources offer widely varying statistics on the efficacy of surgery, but generally surgery has high seizure freedom rates [4]. However, despite the high probability of success, resective surgery is not without significant risks. Potential side effects of surgery vary depending on the epileptic focus but include partial loss of memory, language, and motor function, loss of vision, infection, and even death. Thankfully, complications are rare and arise in only 4% of surgical cases [11].

Approximately 25% of those diagnosed with epilepsy cannot achieve seizure control through medication or surgery [11]. Research into neurostimulation techniques that supply local therapy to the brain for seizure cessation has demonstrated the safety and great potential of such devices to help patients with intractable epilepsy. Vagus nerve stimulation [12, 13] and trigeminal nerve stimulation [14] devices direct short electrical bursts into the brain via nerves in the neck and face, respectively. Other implantable devices deliver electrical stimulation directly into deep brain regions for seizure abatement [15-18]. Transcranial magnetic stimulation, a noninvasive tool that uses a powerful magnet outside of the skull to deliver magnetic pulses for brain

stimulation, is another potential treatment for epilepsy currently under investigation [19, 20]. Focal cooling devices have shown promise in terminating seizures in cases of intractable neocortical epilepsy, which often cannot be treated surgically [21-23].

Accurate localization of the epileptogenic zone, i.e., the area of cortex requisite for epileptic seizure generation, is key to ensuring the success of surgery and neurostimulation techniques. Epilepsy surgeries have been performed since the late 1800's, but there still does not exist a noninvasive method for precisely pinpointing the epileptogenic zone [4]. Removal of this brain region is necessary and sufficient for ending seizures. The closely related seizure onset zone, i.e., the area of cortex that generates clinical seizures, is often used by physicians as a surrogate for the epileptogenic zone because it can be measured using various functional neuroimaging techniques. Resecting the seizure onset zone will not necessarily eliminate seizures but is often sufficient for improving an epilepsy patient's quality of life.

2.2 Electroencephalography

Electroencephalography is a neurophysiologic tool for measuring electrical activity in the brain. The resulting trace, known as an electroencephalogram (EEG), represents a summation of extra-cellular potentials from a large number of neurons. The first publication on EEG recordings from human subjects was released in 1929, and the clinical field of electroencephalography began soon after in 1935 [24]. Since then, the EEG has become the primary tool used in diagnosing and studying epilepsy syndromes.

During EEG recordings, electrical activity is measured through scalp electrodes, grid or strip electrodes placed directly on the cerebral cortex, or depth electrodes inserted

into the brain. While scalp EEG is valuable because it is noninvasive, it suffers from low spatial resolution and is highly susceptible to motion, muscular, and recording artifacts. Scalp EEG has an effective monitoring depth of only about 1 cm below the surface of the brain. The recorded signals are distorted and have much of their high frequency activity filtered out by the intervening tissue, skull, and cerebrospinal fluid. Additionally, the inverse problem of determining the unique generators of epileptic events using distant scalp potentials makes precise localization of the epileptic cortex using scalp EEG alone unreliable [25].

In contrast to noisy scalp EEG signals, the intracranial EEG (IEEG) is relatively free of artifacts and has a high signal-to-noise ratio. Intracranial electrodes are surgically implanted directly into subcortical regions (e.g., the mesial temporal lobe) to observe areas at depths greater than 1 cm from the surface that cannot be readily imaged by surface electrodes, consequently intracranial monitoring often detects neural activity that is not visible or well localized in scalp recordings [26]. The IEEG is clearly a powerful tool in the study of epilepsy, but the collection of IEEG data is restricted by clinical necessity because of its highly invasive nature and the potential for complications. The recording of IEEG signals is governed by strict protocols and is reserved for presurgical evaluation when less invasive methods fail to definitively pinpoint the seizure onset zone.

The study of EEG signals frequently entails analysis of the morphology of the waveforms or examination of specific frequency bands believed to be involved in ictogenesis, i.e., seizure generation. Irregular morphological signatures (e.g., spikes, sharp waves, spike-and-waves, bursts, etc.) and high frequency oscillations have been

analyzed by researchers to detect and predict ictal (seizure) onset [27-34]. Figure 2.2 shows an IEEG recording of seizure activity acquired from an epilepsy patient.

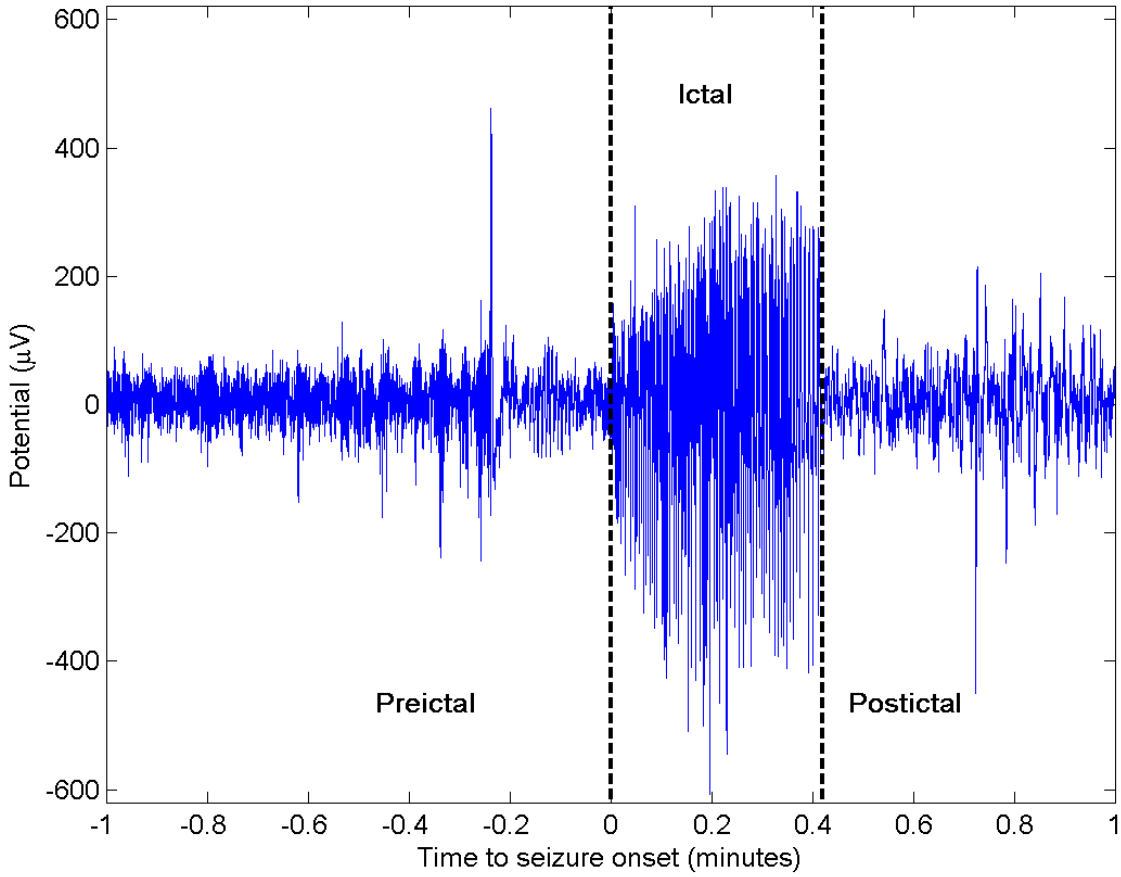

Figure 2.2 An IEEG focus channel showing preictal (before seizure), ictal (seizure), and postictal (after seizure) periods.

2.3 Functional Magnetic Resonance Imaging

Functional magnetic resonance imaging (fMRI) is a noninvasive neuroimaging technique that measures hemodynamic changes resulting from changes in the level of neuronal activity. Through the analysis of fMRI data, which consist of sequences of images acquired over time, the spatiotemporal dynamics of brain activation can be

explored. The contrast in these images is attributable to differences in tissue function rather than structure, which is imaged in anatomical MRI. High-resolution anatomical scans enable identification of any structural abnormalities that might be present, while functional scans provide useful information about neural activity. This information is especially helpful in the absence of any structural irregularities, which would explain the atypical brain function. Two-dimensional cross-sections (known as slices) of functional and structural MRI scans are shown in Figure 2.3. The structural image has noticeably higher spatial resolution.

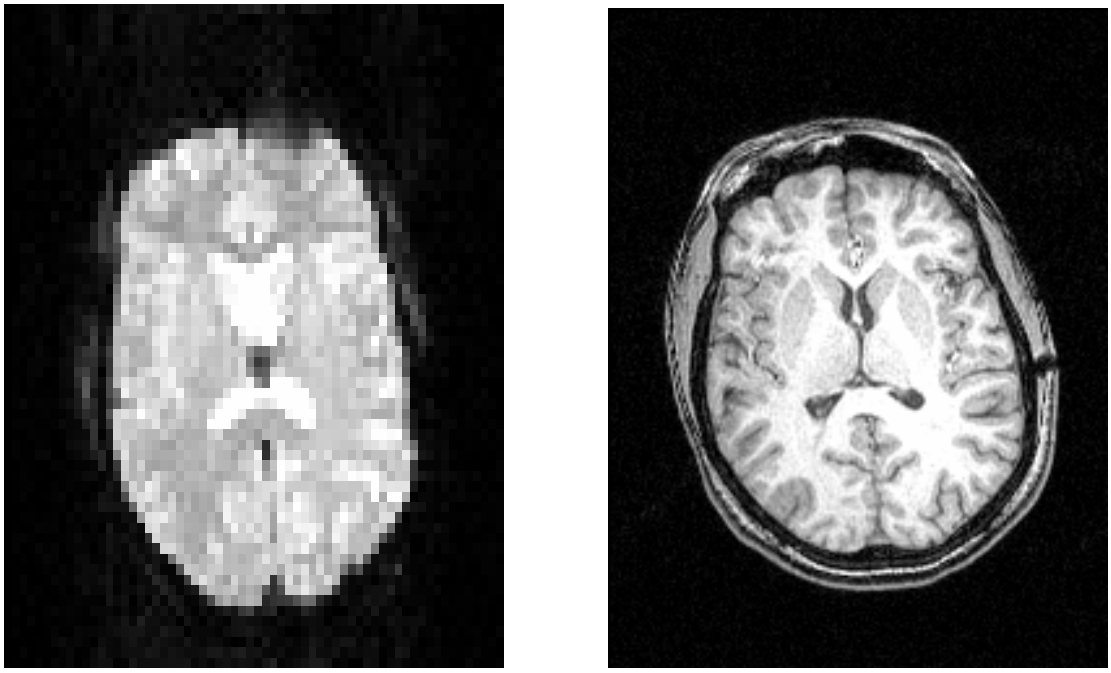

Figure 2.3 Single slices from functional (*left*) and anatomical (*right*) MRI slices. The spatial resolution of the functional image is about 3.5 mm per voxel while the resolution of the anatomical image is 1 mm per voxel.

In fMRI, the voxel size is limited by the tradeoff between small voxel dimension and high signal-to-noise ratio (SNR) [35]; however, even with this constraint, the spatial

resolution of fMRI is still relatively high—on the order of a few millimeters. The temporal resolution of fMRI in human studies is generally in the range of 1 to 3 seconds per three-dimensional image. It is constrained by the necessity of using relatively low magnetic field strengths for safety purposes. Currently most human scans are conducted at magnetic field strengths of 3T (Tesla), although 7T scanners are also commercially available. The higher field strengths used in animal studies have resulted in temporal resolutions of 100 milliseconds, which is much closer to the temporal resolution of EEG. Although fMRI has lower temporal resolution than EEG, its noninvasive nature, good spatial resolution, and the ability to monitor the entire brain simultaneously make it quite useful in localizing epileptic activity. Intracranial recordings can also locate activity with high precision, but the spatial sampling with intracranial electrodes is limited by the number of electrodes that can implanted, which means that the entire seizure onset zone is not necessarily fully covered during monitoring [4].

Functional MRI indirectly measures neural activity through the detection of changes in blood flow, blood volume, and oxygen consumption. Active nerve cells consume extra oxygen, thus causing an increasing need for oxygenated blood. As regional brain function increases, there is a corresponding increase in regional cerebral blood flow (CBF). Blood oxygen level dependent (BOLD) fMRI exploits variations in the relative concentrations of oxyhemoglobin and deoxyhemoglobin that accompany changes in neural activity. The differences in the magnetic properties of these substances provide contrast in BOLD images. Arterial spin labeling (ASL) perfusion fMRI contrast is also a reflection of blood flow changes. During ASL perfusion scans, arterial blood water proximal to the area of interest is electromagnetically labeled by a radiofrequency

pulse to allow tracking of the CBF. Immediately after imaging of the pre-labeled spins, control images without labeled spins are acquired. Through pairwise subtraction of these label and control pairs, the effects of labeling can be determined, and blood flow can be measured quantitatively.

In [36], Detre and Wang provide a comparison of the imaging characteristics of BOLD and ASL perfusion fMRI. BOLD fMRI generally has higher SNR and temporal resolution and larger signal changes due to activation than ASL perfusion. The sampling rate of BOLD fMRI is 1-3 seconds per image, while the sampling rate of ASL perfusion fMRI is 3-8 seconds. The temporal resolution of perfusion fMRI is limited by the transit time of the labeled spins and the need to collect two scans (label and control) per perfusion image. BOLD contrast is also easier to measure, so it is the more widely used technique. Despite the aforementioned drawbacks, ASL perfusion contrast has several characteristics that make it useful for visualizing dynamic changes due to spontaneous neural activity. For one, the ASL imaging approach provides physiological measures of CBF, while the BOLD technique only provides information about relative changes in blood oxygenation. Additionally, ASL has the ability to measure resting function, which cannot be easily observed with BOLD contrast. ASL also has stable noise characteristics over the entire frequency spectrum and is not susceptible to baseline drift as BOLD is, so slow changes in neural activity over long periods of time can be reliably detected using ASL perfusion.

A major application of fMRI is the study of task-related functional activation. In these studies, the subjects perform a specified task during scanning in order to locate the area of the brain responsible for that activity. For example, a subject might perform a

finger tapping exercise in the scanner to image the brain regions involved in that action. The most commonly applied experimental paradigms in the examination of task-related fMRI activation are block and event-related designs. Block designs involve trials of alternating periods of task and control conditions to evoke sustained functional responses. The control blocks are designed to induce the same responses as the task stimuli, except for the cognitive or sensorimotor process of interest. The differences between the responses to these two conditions can then be attributed to the task. Block designs maximize sensitivity by generating large, sustained signal changes, but individual task responses cannot be isolated with this type of experimental design. Conversely, event-related designs are devised to study responses to individual task stimuli and allow the activation due to these stimuli to be isolated. The major difficulty with performing event-related studies is that statistical analysis of such data requires an accurate model of the hemodynamic response, which is not easily characterized [35]. Block data analysis, on the other hand, is not as dependent on an accurate hemodynamic model. More information about block and event-related analysis is given in Appendix A on statistical parametric mapping (SPM).

2.4 Additional Functional Neuroimaging Techniques

EEG and fMRI are only two of the many neuroimaging modalities that have been investigated for the purpose of epileptic focus localization. Other common tools include magnetoencephalography (MEG), positron emission tomography (PET), and single photon emission computed tomography (SPECT). Often they are used in conjunction with EEG to improve the localization of pathological events.

Like EEG, MEG directly traces neuronal activity with high temporal resolution, but instead of measuring potential differences in the brain, it measures magnetic fields due to current flow. The first MEG recordings were made in 1968 using a one-sensor magnetometer [37]. Until the mid 1980's, MEG equipment provided incomplete coverage of the brain because the machines were limited to only a few sensors, so data from multiple brain regions had to be acquired successively, which was time consuming [38]. However, improvements in the technology have led to MEG scanners with hundreds of sensors and resulted in whole-scalp coverage.

The clinical applications of MEG remain controversial [38]. The fact that MEG signals are not distorted by the dura, skull, and scalp gives it a potential advantage over EEG in source localization; however, this has not always proven to be the case. Researchers first reported on the use of MEG to localize epileptiform discharges in human subjects in 1982 [39]. Since then, research has shown that EEG and MEG provide complementary information about interictal epileptiform discharges (IEDs). Some discharges detected using EEG are not evident in corresponding MEG recordings and vice versa [40]. MEG is more sensitive to neocortical spike sources [40-42], while EEG provides more comprehensive cortical coverage [4, 40]. In studies of TLE, Baumgartner et al. and Leijten et al. found that MEG cannot consistently detect activity limited to mesial temporal structures [41, 42], thereby limiting its applications in the assessment of TLE. These limitations and the high cost of MEG, continue to constrain the use of this noninvasive method for source localization.

Unlike MEG, which is still largely experimental, PET and SPECT have well-established roles in the evaluation of epilepsy patients. Both PET and SPECT are nuclear

medicine imaging techniques, and as such, they involve exposure to ionizing radiation, although at low concentrations. This risk of radiation limits their use to clinical necessity. Depending on the tracer used, PET can measure interictal brain metabolism or CBF. SPECT measures both ictal and interictal CBF. When scalp EEG cannot determine the seizure onset zone, one or both of these imaging modalities are often used to localize epileptic activity.

Early PET studies showed that areas of interictal cortical hypometabolism were concordant with the epileptogenic zone lateralization [43, 44]. SPECT scanning as a presurgical diagnostic tool was originally introduced as a cheaper alternative to PET for measuring local CBF changes, which are closely coupled to regional metabolic changes [4]. Interictal PET and ictal SPECT have demonstrated high sensitivity and specificity to temporal lobe epilepsy abnormalities but lower sensitivity to extratemporal abnormalities [45]. When combined with ictal EEG and other clinical information, these neuroimaging techniques improve the precision of localization and the understanding of pathological activity.

2.5 Applications of fMRI in Epilepsy Research

In recent years, an increasing number of studies on the applications of fMRI in epilepsy have been conducted in hopes of exploiting the noninvasive nature of fMRI and the widespread availability of MRI scanners. These applications include presurgical evaluation of task-correlated memory and language function and localization of interictal activity.

A potential complication of temporal lobectomy is the loss of memory and language functions. The intracarotid amobarbital test (IAT), also known as the Wada test, is the standard diagnostic tool for presurgical lateralization of memory and language. During the test, portions of one brain hemisphere are anesthetized so that function in the other hemisphere can be tested independently. Though this test is highly accurate, it is invasive and therefore potentially risky. Many researchers have investigated the application of fMRI as a noninvasive alternative to IAT. Desmond et al. [46] and Binder et al. [47] both reported strong agreement between the language laterality determined using fMRI and IAT on epilepsy patients. These studies involved using different tasks to activate regions of the brain responsible for language function in order to lateralize language dominance. Detre et al. performed a visual scene encoding task activation study for lateralizing memory function and also found excellent agreement between the fMRI and IAT results [48].

In addition to performing these task related localization studies for presurgical evaluation, researchers have also explored possible uses of fMRI in determining the sources of interictal epileptic activity. Detre et al. detected localized signal intensity changes in the BOLD fMRI time courses of a focal epilepsy patient [49]. They took a simple analysis approach wherein percentage change images were visually inspected to find areas of significant signal change. Through this time series analysis, they identified focal fluctuations that correlated well with the epileptogenic zones found using ictal SPECT and IEEG. Subsequent region of interest analysis found two highly stereotyped events indicative of subclinical seizures. Krings et al. performed a similar study of a patient with a mass lesion who experienced a simple partial seizure during scanning [50].

Analysis of the percentage change in the BOLD signal revealed seizure related hemodynamic changes in the area of the lesion. Though this method proved useful in these two studies for mapping ictal activity with fMRI in a single patient, a technique for identifying interictal activity would be more valuable since ictal activity during fMRI scans is uncommon and can result in large movement artifacts that corrupt the images. Also, a more sophisticated methodology may be needed for analyzing data collected from patients with more diffuse epileptic networks than those studied in [49, 50].

To date, most studies of fMRI use in epilepsy have focused on examining changes in the BOLD signal associated with interictal epileptic activity. Wolf et al. were able to detect mesial temporal lobe hypoperfusion (reduced blood flow) in epilepsy patients using ASL perfusion data [51]. Twelve patients with medically refractory TLE and twelve healthy subjects were scanned using continuous ASL perfusion. The authors found that in the control participants, the normalized mesial temporal lobe CBF (found by dividing the regional mean by the global CBF) tended to be significantly higher on the left than the right side. There was evidence of hypoperfusion ipsilateral to, i.e., on the same side as, the epileptogenic temporal lobe in eleven of the twelve patients. Asymmetry indices—measures of the differences in the mean CBF values between the two lobes—were not significantly different in patients and controls, but the asymmetry index proved useful in clinical lateralization. The ASL perfusion lateralization agreed with the PET lateralization for all but one patient who underwent a standard FDG-PET scan, which measures brain metabolism. These results demonstrate that clinical lateralization of TLE patients can, in most cases, be determined by the presence of hypoperfusion in the ipsilateral MTL.

The employment of both EEG and fMRI in the localization of interictal activity allows one to combine the high temporal resolution of EEG and the high spatial resolution of fMRI for a better understanding of the spatiotemporal dynamics of IEDs. This fusion provides the ability to directly correlate regional fMRI signal changes to epileptic spikes in the EEG. The technical problems of acquiring simultaneous EEG and fMRI have been solved, and the data can be safely acquired using specialized equipment [52]. The use of MR-compatible electrodes, safety resistors, and fiber optic isolation protects the patient, and shielding the electronics minimizes the effects of the EEG recording on the image quality. A more difficult problem to address is the creation of large artifacts in the EEG signal during simultaneous image acquisition. The voltages of the time-varying magnetic fields completely obscure the EEG rendering the data useless in the absence of any postprocessing. For this reason, most EEG/fMRI recordings have been interleaved until recently [53-56].

Jäger et al. developed a spike-related fMRI method to detect epileptiform activity [57]. The EEG recordings were monitored online by a neurologist, and BOLD fMRI recordings were initiated 3–5 seconds after an epileptic discharge. The image acquisition was delayed to ensure that EEG events did not influence image contrast. There is an approximately 3 second delay in BOLD signal changes after an event, so the imaging delay did not result in the loss of contrast data after the EEG event. Ballistocardiographic contamination (artifacts in the EEG due to the beating of the heart) was removed using subtraction techniques. The authors found significant increases in the BOLD signal intensity, with a peak 6–7 seconds after the spike detection. The signal then decreased and returned to normal after about 18 seconds. These results showed promise for

understanding the hemodynamic response to interictal events, but the problem with this technique is the lack of baseline imaging data and preictal and postictal data. Continuous, simultaneous EEG and fMRI recordings clearly provide more useful information than EEG-triggered fMRI.

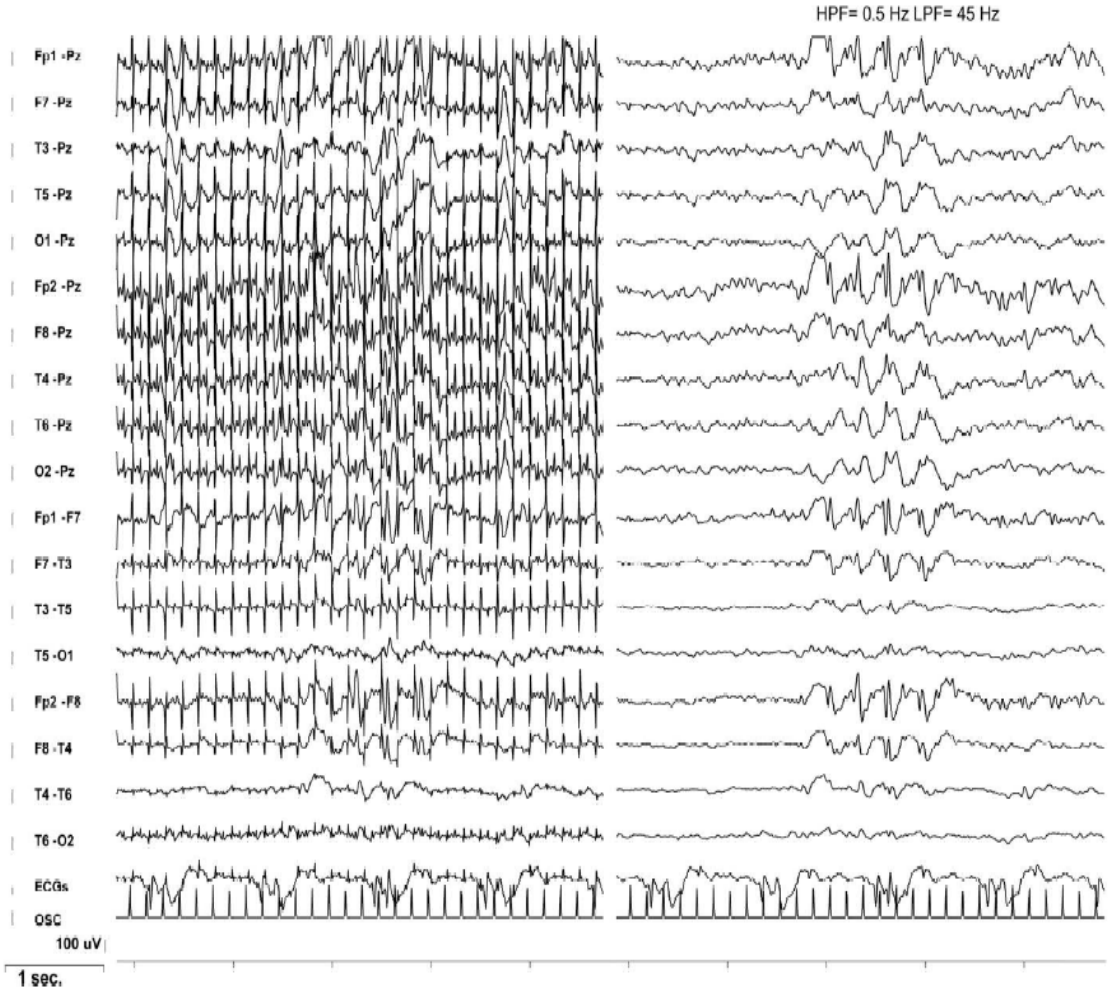

Figure 2.4 This figure from [52] illustrates the effects of imaging artifacts on scalp EEG recorded during simultaneous acquisition of EEG and fMRI. The traces on the left are the raw acquired data, and the signals on the right are the same traces after the removal of imaging and pulse artifacts.

With more advanced hardware and improved postprocessing techniques for imaging artifact removal, continuous acquisition of both fMR images and EEG is now possible. In [58], Bénar et al. discuss various techniques for removal of the ballistocardiogram and gradient artifacts from the EEG. Previously subtraction techniques and spatial filtering had been used to eliminate the ballistocardiogram [59]. Bénar et al. present spatial filtering techniques based on principal component analysis (PCA) and independent component analysis (ICA). They found that spatial filtering using ICA tended to yield better results than PCA. Bénar et al. also developed a methodology for removing the gradient artifact [58]. The procedure entailed building a model of the artifact and subtracting it from each frame of the EEG. They compared their technique to the Fourier method developed by Hoffmann et al. in [60] and found that their subtraction filter worked better than the Fourier method in most cases and worked as well in all other cases. The Fourier method involved computing the FFT of segments of EEG and setting to zero Fourier coefficients corresponding to frequencies for which the FFT amplitude differed from the baseline spectrum by more than a certain factor. These reports demonstrate that with appropriate postprocessing, high-quality simultaneous EEG/fMRI data can be generated. Figure 2.4 shows an example of scalp EEG recorded during simultaneous fMRI acquisition and how the signal quality can be greatly improved by artifact removal techniques.

Early investigations demonstrated the potential to localize interictal activity both temporally and spatially with simultaneous EEG/fMRI data. Baudewig et al. were able to locate areas of epileptic activity in a subject with generalized epilepsy by linking EEG abnormalities to BOLD signal changes [61]. In this study, they identified segments of

epileptic activity in the EEG and then correlated the epileptic events with specific images. For each of these images, they then measured the BOLD signal intensity change to find the activated pixels in each image. Lemieux et al. found areas of activation in a patient with partial and secondary generalized seizures through event-related SPM analysis of the data. The activated areas were concordant with scalp and intracranial EEG findings. Though they show the potential usefulness of simultaneous EEG and fMRI recordings in epilepsy research, the small scope of these studies makes drawing conclusions about the utility of these methodologies impossible.

Since the report by Lemieux et al. in 2001, various similar works on localizing the BOLD response to interictal scalp EEG discharges using event-related SPM analysis have been published. Researchers have pinpointed areas of activation in both focal epilepsy [62-69] and generalized epilepsy [70-73] patients with frequent interictal events. A major limitation to this approach is that IEDs visible on scalp EEG do not always have a significant hemodynamic correlate. In fact, most of these studies only reported such a relationship in approximately 50% of patients. Epileptic focus localization with this technique is not possible for patients with infrequent IEDs or those without adequate hemodynamic changes due to IEDs. Additionally, interictal events not evident in the EEG recordings may produce noticeable hemodynamic changes but cannot be evaluated with this methodology.

Combining EEG and fMRI in the localization of epileptiform generators has shown promise, but the equipment necessary to acquire simultaneous EEG and fMRI data is not widely available. The aforementioned constraints on patients who can be assessed with this manner also restrict its usefulness. Until resources become more accessible and

the methodology can be applied a larger subset of patients, analysis of fMRI without concurrent EEG may serve as a suitable alternative. Data-driven techniques such as independent component analysis (ICA) and temporal clustering analysis (TCA) have been explored for this purpose [74-76].

Morgan et al. investigated the use of TCA to localize interictal epileptic activity in resting BOLD images without the need for simultaneous EEG recordings [77]. TCA for the processing of fMRI was introduced by Liu et al. in a study on the BOLD signal changes in subjects after drinking a glucose solution [78]. The goal of TCA is to establish the times at which significant numbers of voxels have a BOLD response of interest. Later modifications to the technique aimed to improve sensitivity and allow detection of multiple activation cycles, which could not be uncovered previously [79, 80].

In their study, Morgan et al. examined six TLE patients and three patients whose seizure localization had not yet been confirmed by successful surgery [77]. A histogram of the number of voxels reaching their maximum intensities at each point in time was created for each subject. Peaks in the histogram were identified as time points with at least 100 voxels attaining a maximum intensity. These peaks found using TCA were then convolved with a BOLD hemodynamic response function to create a model of the BOLD signal response curve for that data series. Traditional event-related SPM analysis was then carried out on the modeled BOLD response curves to find the areas of activation. The regions of activation found using TCA and SPM were concordant with the abnormal regions identified using standard EEG and PET analysis. One possible criticism of this technique is that the peaks in the histogram are not necessarily due to epileptic activity.

In fact, voxels randomly reaching their maxima during a peak are incorrectly considered to be activated.

Hamandi et al. compared the localization results of the TCA method detailed by Morgan et al. with those obtained using an EEG correlated fMRI analysis routine [81]. Eight patients with clear epileptic foci were chosen for this study. They showed that areas of activation found with TCA did not correspond to the known focus and were not concordant with EEG/fMRI localizations. They also found that temporal clusters often coincided with times of excessive head motion, leading to a high probability of false positive activations. Another major drawback of TCA as presented by Morgan et al. is that voxels with more than one peak in activity can only be assigned to one temporal cluster, which limits the sensitivity of the algorithm. The assessment of Hamandi et al. highlights some of the shortcomings of TCA [81].

To address the criticisms of the TCA technique, Morgan et al. developed a two-dimensional TCA algorithm (2dTCA) [76]. The most significant difference between the original TCA method and 2dTCA is in the construction of the histograms used for temporal clustering. 2dTCA creates a two-dimensional histogram of the number of voxels with significant BOLD peaks. Along the *x*-axis is the time of the first peak, and along the *y*-axis is the number of voxels with a BOLD peak at each point in time. Voxels with the same initial peak time contribute to the same column of the histogram. In this way, voxels with similar transient responses are grouped together, and activations due to separate interictal events can be evaluated. The authors used these event timings as regressors in an SPM analysis and also added information about motion during scanning to the model to reduce the effects of spurious activations due to patient motion. The

analysis of simulated fMRI data showed increased sensitivity over conventional TCA but fewer false activations due to motion [76]. A study of in vivo data from 17 epilepsy patients demonstrated the ability to detect temporal lobe activations in 16 subjects (94%) [75]. fMRI activation was concordant with EEG findings in 64% of subjects, which is significantly better than the average of 49% concordance in combined EEG/fMRI studies. Some issues that need to be addressed are the unknown nature of 2dTCA activations, which could be explored through analysis of EEG-correlated fMRI, and the best way to cluster voxels with similar transient responses. Two voxels experiencing their first significant peaks at the same time may have widely varying responses thereafter, and conversely, voxels with very similar overall responses but different initial peak times will not be grouped. Improving the method of secondary clustering may improve the sensitivity and specificity of the technique.

In conclusion, applications of fMRI in epilepsy have shown promise for its clinical utility, but there is still much room for improvement. Analysis of features of fMRI data may improve the understanding of the hemodynamic response to interictal activity and improve the accuracy of IED localization.

CHAPTER 3

RESEARCH METHODOLOGY

This chapter presents a detailed explanation of the methods employed in this work for detecting areas of epileptic activity in fMRI data. As illustrated in Figure 1.1, the process is divided into three main stages: 1) data preprocessing to reduce imaging noise and artifacts; 2) feature processing for dimensionality reduction and characterization of the data; and 3) classification of individual brain voxels as members of the epileptic network or normal brain tissue based on their feature values. This chapter also provides information about the real fMRI patient data examined in this study and describes the synthetic data generation procedure.

3.1 Datasets

Because this work explores a novel method for analyzing areas of activation in fMRI data, rigorous verification and validation of the techniques are necessary to prove their utility. To that end, in addition to examining real data from human subjects with nebulous epileptogenic zones, phantom data—simulated data modeled to closely resemble actual patient data—with known areas of activation are examined for statistical validation of the methodology.

3.1.1 Real Subject Data

Resting ASL perfusion fMRI scans of five temporal lobe epilepsy patients and three healthy controls were obtained from the Center for Functional Neuroimaging at the

University of Pennsylvania. All subjects provided informed consent in accordance with Institutional Review Board guidelines. The three healthy subjects were analyzed to serve as controls for this experiment. All subjects were made comfortable using head padding and told to sleep. Increased interictal epileptiform activity on EEG often accompanies sleep in patients with temporal lobe epilepsy [82], so it was hypothesized that allowing the subjects to sleep would increase the likelihood of epileptic activity during the scan. However, without simultaneous EEG recordings, the legitimacy of this hypothesis could not be assessed. After scanning, all subjects reported falling asleep during the scan, but no information was available about when they fell asleep or the stage of sleep attained.

The resting perfusion images were collected during consecutive 10-minute scanning sessions at 3T with a repetition time of 3 seconds. All subjects, except for one control (Con1) and one patient (Pt5), were scanned for a total of 40 minutes. Con1 and Pt5 were scanned for only 20 and 30 minutes, respectively, due to time constraints on scanner availability. Each 10-minute functional dataset contains a total of 200 images. The raw ASL images consist of 16 slices that are 64 × 64 voxels in size with a voxel resolution of 3.44 × 3.44 × 7.50 mm^3. The odd numbered scans in each set are label images, and the even numbered scans are control images.

Prior to the functional scanning, each of the five patients had EEG recordings taken that showed interictal spikes in one temporal lobe. During extended video EEG monitoring, all but one, Pt4, had seizures clearly originating in a single temporal lobe. One left temporal and two right temporal seizures were recorded for this patient. Anatomical MRI scans showed right mesial temporal sclerosis—a lesion commonly found in adults with TLE—in Pt2 and bilateral hippocampal volume loss in Pt5, with the

right hippocampus being smaller than the left. The other three patients had normal brain structure. Four of the five patients also underwent PET scanning to look for evidence of hypometabolism in the temporal lobe, which is common in TLE patients. Pt4 had a normal PET scan. Pt1 and Pt5 showed hypometabolism in the temporal lobe in which the seizures were recorded, and Pt2 exhibited hypometabolism in the epileptogenic hemisphere but not the temporal lobe itself. Neurologists combined this clinical information to determine the seizure onset side for each patient. For Pt4, it was not completely clear whether the disease was bilateral or unilateral, but the presumed epileptogenic zone was chosen. The clinical information for each of the patients is summarized in Table 3.1.

Table 3.1 Summary of the clinical information for the five mesial temporal lobe epilepsy patients examined in this work.

Subject	EEG	MRI	PET
Pt1	Left side interictal spikes; Left temporal seizures	Normal	Hypometabolism in left temporal lobe
Pt2	Right side interictal spikes; Right temporal seizures	Right mesial temporal sclerosis	Hypometabolism in right temporal lobe
Pt3	Left side interictal spikes; Left temporal seizures	Normal	—
Pt4	Right side interictal spikes; 2 right temporal, 1 left temporal seizure	Normal	Normal
Pt5	Left side interictal spikes; Left temporal seizures	Bilateral hippocampal volume loss	Hypometabolism in left temporal lobe

3.1.2 Phantom Data

The first step in the process of generating the synthetic fMRI data was the creation of the baseline series, i.e., a set of low noise images without activations or motion artifacts. The same baseline dataset was used for all generated phantoms. The baseline series was formed by computing the mean label and control images from a scanned subject's ASL perfusion dataset. The images were motion corrected and spiking artifacts were removed prior to calculating their means. These preprocessing steps are discussed in detail in Section 3.2. The mean images were then replicated 400 times each and interleaved to create a baseline set consisting of 800 alternating label and control images. The perfusion series—a set of images produced by subtracting each label image from the subsequent control image—had constant values in all of its voxel time courses. The voxel time course, a signal corresponding to a voxel's intensity as a function of time, is obtained by extracting the voxel intensity from the images at each point in time as illustrated in Figure 3.1. The baseline image series with constant time courses formed the basis for the synthetic datasets.

An accurate model of the hemodynamic response function (HRF), i.e., the fMRI signal change resulting from a single brief stimulus in the brain, is necessary to produce realistic phantom fMRI datasets. The nature of the hemodynamic response to neural activity has been widely explored by researchers, but no one HRF model that fits all human subjects has been found because HRFs vary greatly from person to person and also vary within a subject from one brain region to another [83]. Differences in the shapes of the HRFs, time-to-onset following stimulus, maximum signal change, time-to-peak, and the full width at half maximum (FWHM) of the response have been reported in

both BOLD and perfusion fMRI studies [84, 85]. A post-peak undershoot (a drop in the signal intensity below the baseline value) with variable degree and timing among subjects has also been observed in many empirical HRFs but is not always present. The presence of an 'initial dip' in the fMRI signal due to an increase in oxygen consumption following stimulus and prior to the signal peak has been observed as well in some BOLD studies, but its existence is not universally accepted [36].

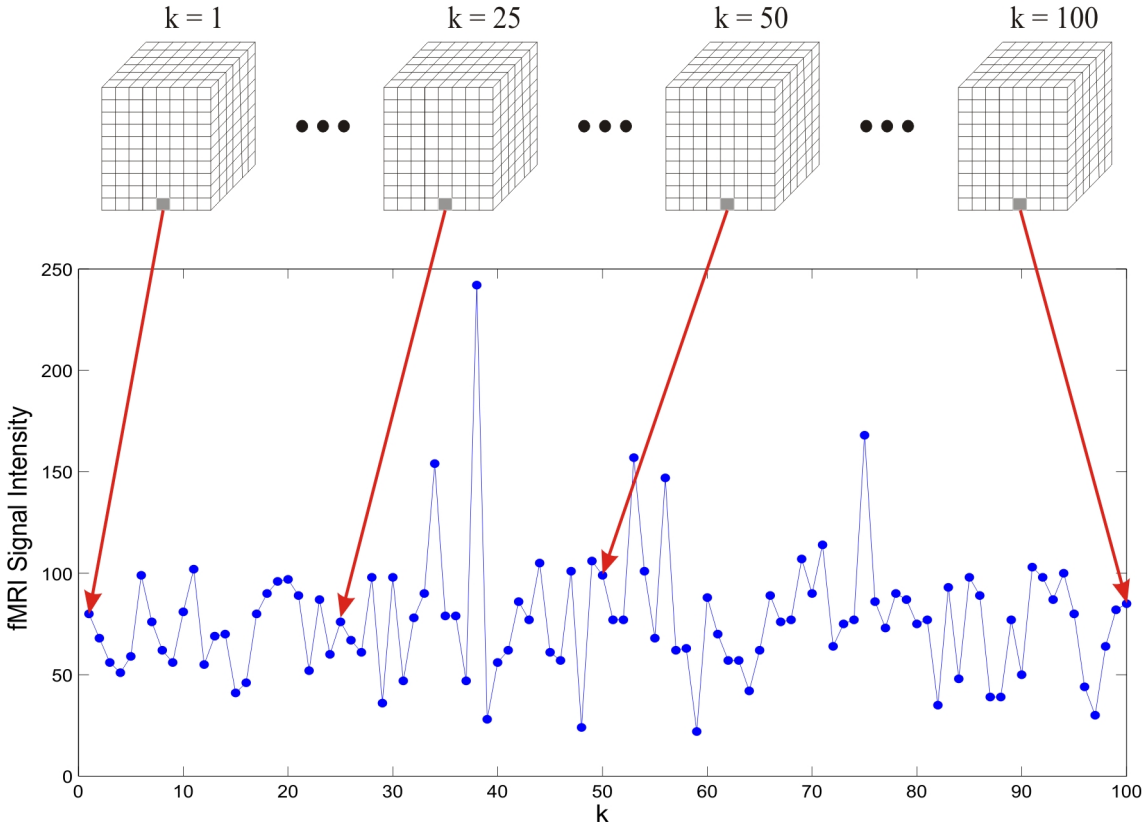

Figure 3.1 An illustration of the voxel time course extraction procedure.

In their work, Friston et al. found that the BOLD HRF can be modeled with a Poisson function [86], while Boynton et al. determined that a gamma function provided a

more appropriate model [87]. The gamma function model has been shown to account for a much greater percentage of the fMRI evoked response to stimulus than the Poisson model and is therefore the more commonly employed model [83]. Although these studies focused on the hemodynamic response in BOLD signals, the same models can be applied to perfusion fMRI because the HRF shapes are similar for the two methodologies [84]. Because of the aforementioned reasons, a gamma function based model was exploited in this research to simulate the hemodynamic response to epileptic activity. Instead of applying the single gamma function model suggested by Boynton et al., the sum of two gamma functions model was chosen in order to incorporate a post-peak undershoot into the HRF [85]. The 'initial dip' is not included in this model. The sum of two gamma functions model is described by the following equation:

$$y(t) = \mathrm{A}_1\left(t-\delta_1\right)^{h_1} e^{l_1(t-\delta_1)} + \mathrm{A}_2\left(t-\delta_2\right)^{h_2} e^{l_2(t-\delta_2)} \tag{3.1}$$

where A_1 and A_2 control the peak and undershoot amplitudes, respectively, h_1 and h_2 affect the widths and timings of the peak and undershoot, l_1 and l_2 also affect the peak and undershoot widths, and δ_1 and δ_2 determine the time-to-onset of the HRF. In this work, the values for the parameters in Equation 3.1 were chosen based on empirically determined ranges from real subject HRF analyses reported in literature [83-85]. The shape of the HRF, the timings and numbers of simulated epileptic events, and the size and location of the epileptic focus were varied for each phantom dataset. The maximum percentage signal change for the simulated activations ranged from 10% to 20% above the baseline value. Signal changes within this range have been reported in other perfusion data studies [84, 88]. The chosen HRF model is shown in Figure 3.2, and

Table 3.2 summarizes the ranges of values used for some important HRF signal characteristics.

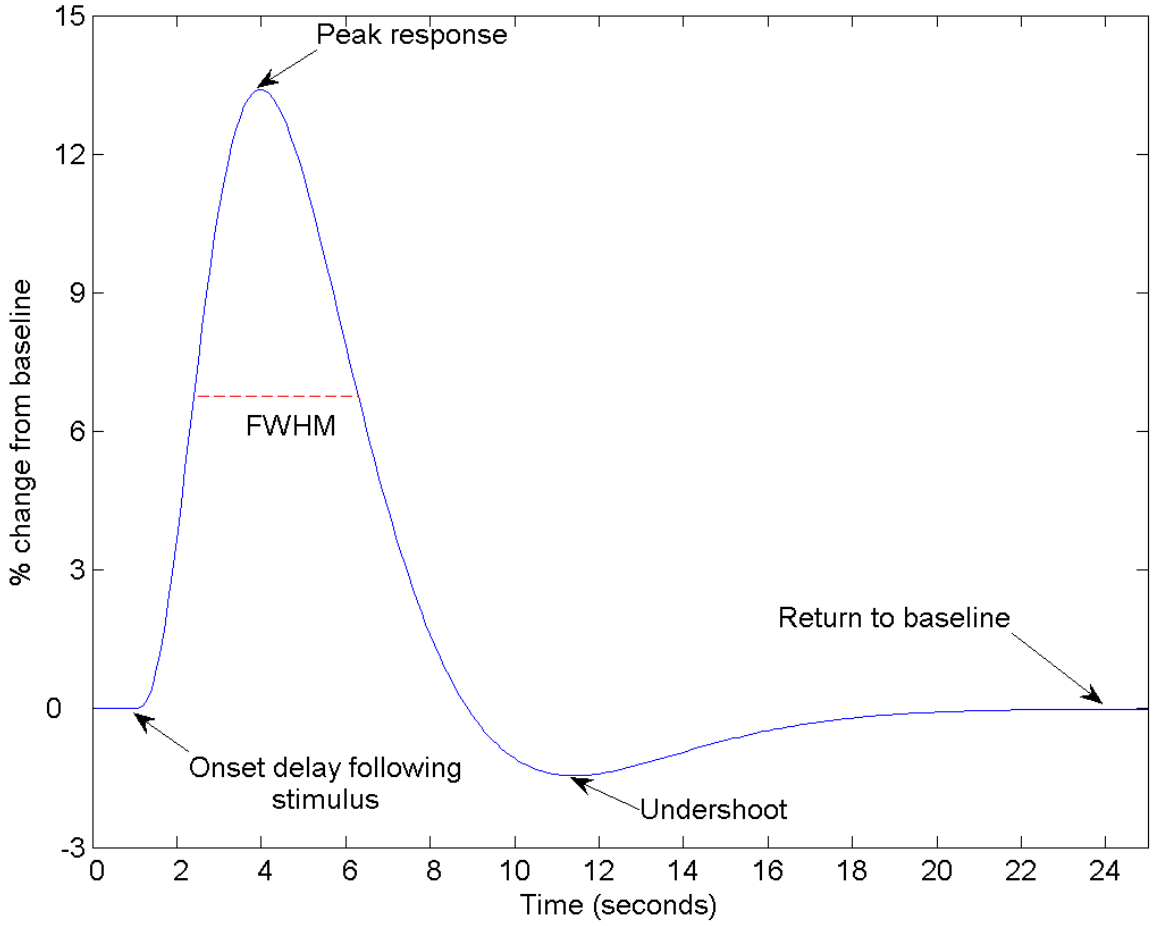

Figure 3.2 The sum of two gamma functions model of the HRF.

Table 3.2 Ranges of values for the simulated HRF characteristics.

Characteristic	**Values**
Percent maximum signal change	10%−20%
Time-to-peak response	4−5 seconds
Time-to-undershoot	9−10 seconds
FWHM	5−6 seconds
Ratio of peak response to undershoot	4−5

After adding simulated activations to the baseline dataset, motion deformations were applied to the images to model the effects of subject motion during scanning. Movement related fMRI signal changes can account for a majority of the signal variance in extreme cases and can result in false positive activations if not accounted for prior to data analysis [89]. Random head movements were simulated in this work to create phantoms with realistic motion characteristics. Task correlated-motion, which arises as a result of a subject's actions during a task activation study (e.g., a finger tapping exercise), is not present in resting functional data, so this type of motion was not added to the phantoms.

Motion in fMRI data is typically modeled as a six-parameter rigid body transformation that describes translations along the Cartesian coordinate system axes and rotations about these axes [90, 91]. Using this model, the n^{th} volume in the series, $f_n(\mathbf{x})$, can be related to the first volume by the following equation:

$$f_n(\mathbf{x}) = \alpha_n f_1(\mathbf{R}_n \mathbf{x} + \mathbf{t}_n) + e_n(\mathbf{x}) \tag{3.2}$$

where $\mathbf{x}$ is the spatial position of the voxel, $\mathbf{R}_n$ is a 3 × 3 orthonormal matrix characterized by the three rotation parameters, $\mathbf{t}_n$ is a 3 × 1 vector comprised of the three translation parameters, α_n is a scaling factor to account for intensity differences between volumes, and $e_n(\mathbf{x})$ is noise [89]. The motion parameters for each of the eight real subject datasets were estimated using the statistical parametric mapping software package SPM2 [5, 6, 90] and used as the basis for the motion time courses in the phantom data. The motion parameter time courses for subject Con2 are shown in Figure 3.3.

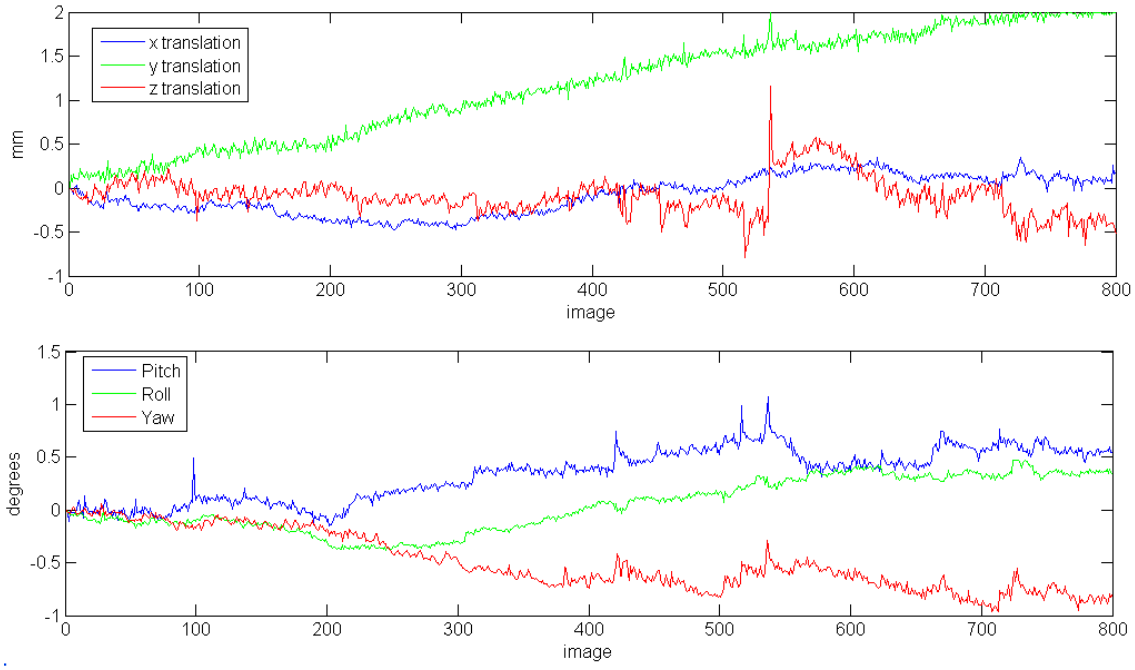

Figure 3.3 The translational (*top*) and rotational (*bottom*) motion parameters for subject Con2. Pitch, roll, and yaw represent the rotation about the x, y, and z axes, respectively.

The final consideration in the creation of the phantom datasets was the choice of noise models. The noise in fMRI is often assumed to be Gaussian, but studies have shown that the magnitudes in MR images actually assume a Rician distribution [92, 93]. At high SNRs, the Rician distribution approaches the Gaussian distribution, but the former model provides a closer approximation to the image noise at low SNRs. The Rician nature of the image noise is illustrated in Figure 3.4, which shows the histogram of the background voxel intensities for an ASL image from a control subject. To generate this histogram, the non-brain regions (background voxels) were manually segmented, and their intensity values were extracted. The Rician probability density function (PDF) provides a better overall fit to the data than the Gaussian PDF. The Rician PDF is a close match to the background noise histogram except at the point in the

histogram where there is a brief excursion from the trend. Figure 3.5 shows the histogram of image voxels corresponding to brain tissue regions. This higher SNR region has an intensity distribution that is almost Gaussian, as expected.

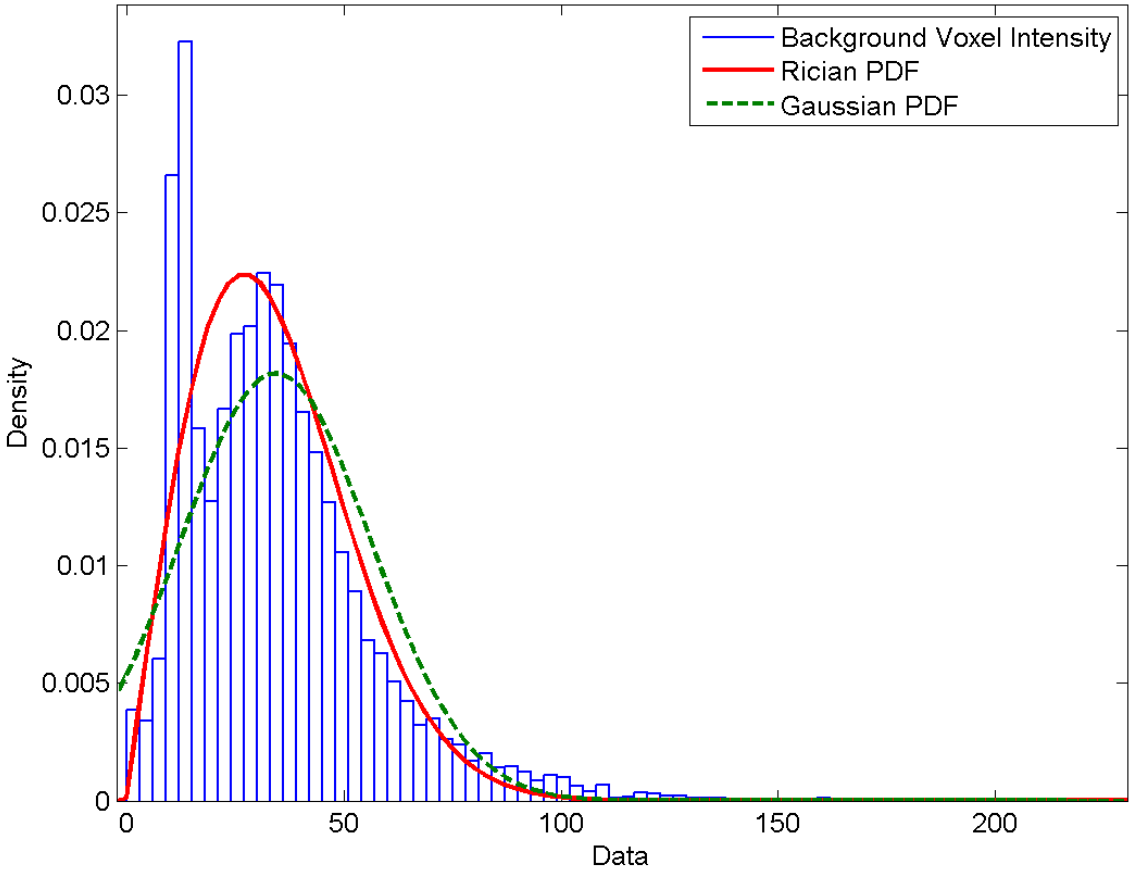

Figure 3.4 This figure demonstrates the close fit between the Rician PDF and the histogram of the background noise in an fMR image. The Rician PDF clearly provides a better fit than the Gaussian PDF over the entire intensity range.

The PDF of the noisy images is defined by the following equation:

$$p(r) = \frac{r}{\sigma^2} e^{\frac{-\left(r_0^2 + r^2\right)}{2\sigma^2}} I_0\left(\frac{r_0 \cdot r}{\sigma^2}\right) \tag{3.3}$$

where r_0 is the intensity of the underlying noise-free image, σ controls the scale of the noise, r_0/σ is the image SNR, and I_0 is the modified zeroth order Bessel function of the first kind. As Equation 3.3 indicates, the Rician noise in these images depends on the noise-free image intensity. Because of this, Rician noise cannot be simply added to the images. The image intensities are made Rician distributed by adding complex Gaussian white noise to the images and taking the magnitude of the complex data to form real-valued, noisy images [93, 94].

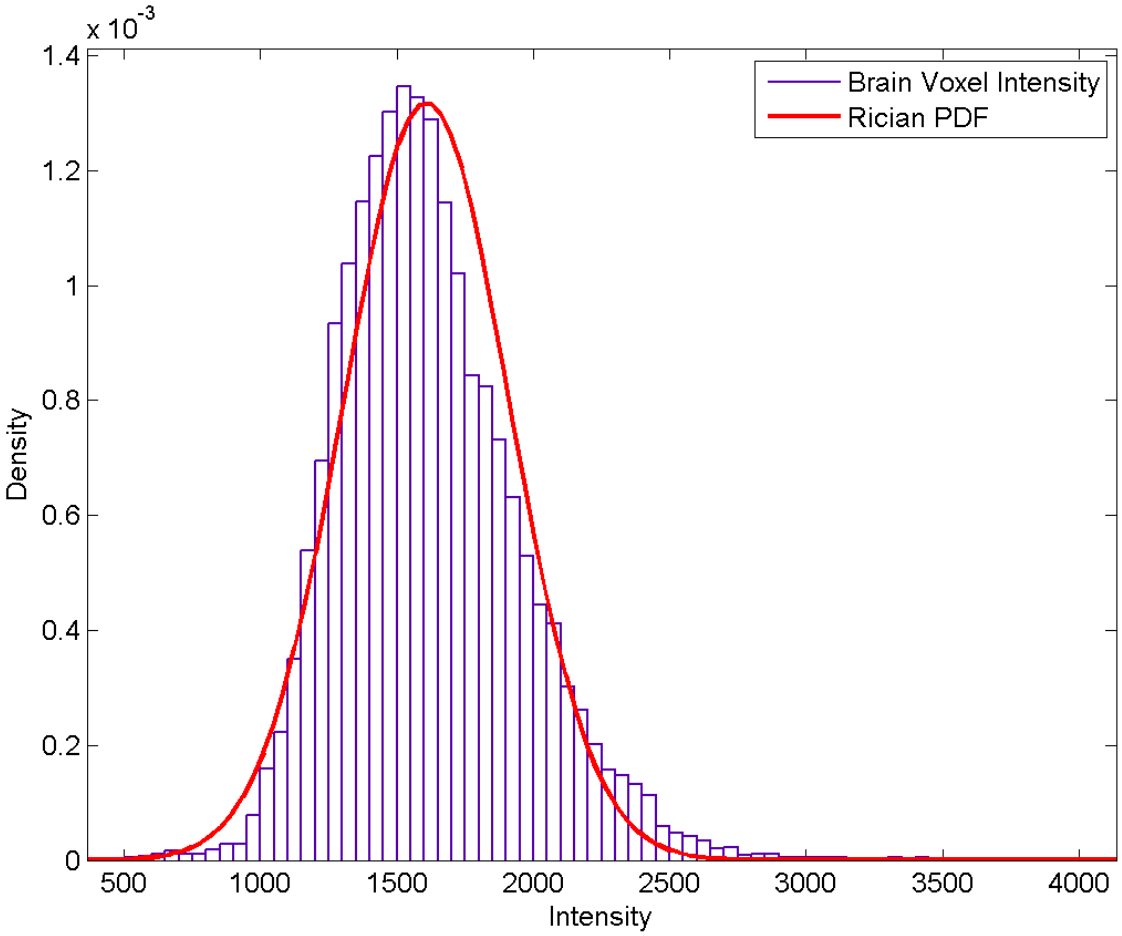

Figure 3.5 Histogram of the brain voxel intensity values with a Rician PDF overlaid. For this high SNR region of the image, the Rician distribution strongly resembles a Gaussian distribution.

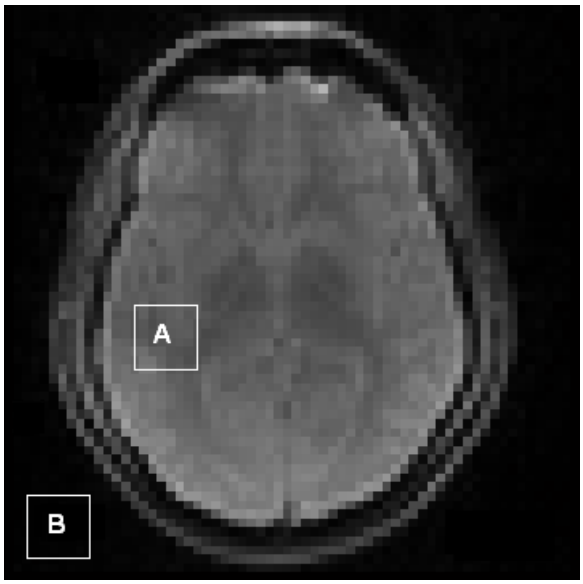

Figure 3.6 The regions of interest (ROIs) selected for estimating the image SNR as defined in Equation 3.4. The same ROIs were used for all subjects.

To generate the noisy images, first an appropriate SNR was chosen. The SNR values from the subject ASL scans were estimated to determine reasonable choices for phantom data SNRs. Applying the technique outlined by Pickens et al. in [95], the value of the SNR was computed for each acquired image, and a realistic range of SNR values was obtained. This procedure involved choosing a region of interest (ROI) inside the brain (ROI_A) and a background ROI without visible artifacts (ROI_B) as depicted in Figure 3.6. An estimate of the image SNR was then calculated using Equation 3.4. The computed SNR values for the data collected in this study ranged from approximately 29 dB to 49 dB with an average of 40 dB. After selecting an SNR, the value of the standard deviation of the background voxels necessary to yield the chosen SNR was computed using Equation 3.4, and the Rician distribution parameter σ was then found using Equation 3.5. The correction factor in the denominator of Equation 3.5 is needed due to

the fact that the variance of the Rician distribution is $\sigma_R^2 = \sqrt{\sigma^2(2-\pi/2)}$ when the image intensity is zero (as it would be in the noise-free background voxels). σ is the standard deviation of the Gaussian noise used to generate the Rician distribution, not the distribution itself. The final step of the procedure was to generate the noisy images using Equation 3.6, where **x** is the voxel spatial location and n_1 and n_2 are the real and imaginary components, respectively, of complex Gaussian white noise with zero mean and variance σ^2.

$$SNR = 20 \cdot \log_{10}\left(\frac{\text{mean}(ROI_A)}{\text{std}(ROI_B)}\right) \tag{3.4}$$

$$\sigma = \frac{\text{std}(ROI_B)}{\sqrt{2-\pi/2}} \tag{3.5}$$

$$r(\mathbf{x}) = \sqrt{(r_0(\mathbf{x}) + n_1(\mathbf{x}))^2 + n_2^2(\mathbf{x})}, \quad n_1, n_2 \sim N(0, \sigma^2), \text{ i.i.d.} \tag{3.6}$$

The following is a summary of the procedure implemented for generating realistic fMRI phantom data:

1. The baseline data were created from a control subject dataset after the images were motion corrected and spike artifacts were removed.
2. The HRF model given in Equation 3.1 was added to a subset of the voxels to simulate epileptic activity in the brain.
3. Motion artifacts were added to the data using the relationship in Equation 3.2 in order to simulate the effects of patient movement during scanning.
4. Finally, the image intensities were modified using Equation 3.6 to model fMRI data with Rician noise characteristics.

3.2 Preprocessing

Prior to analyzing the data, they had to be preprocessed to account for imaging artifacts, physiologic artifacts, and noise. After signal enhancement, the CBF images were calculated, resulting in images whose voxel intensities represented blood flow in physiological units. Figure 3.7 provides an overview of the preprocessing steps. The following sections discuss each of the major preprocessing stages in greater detail.

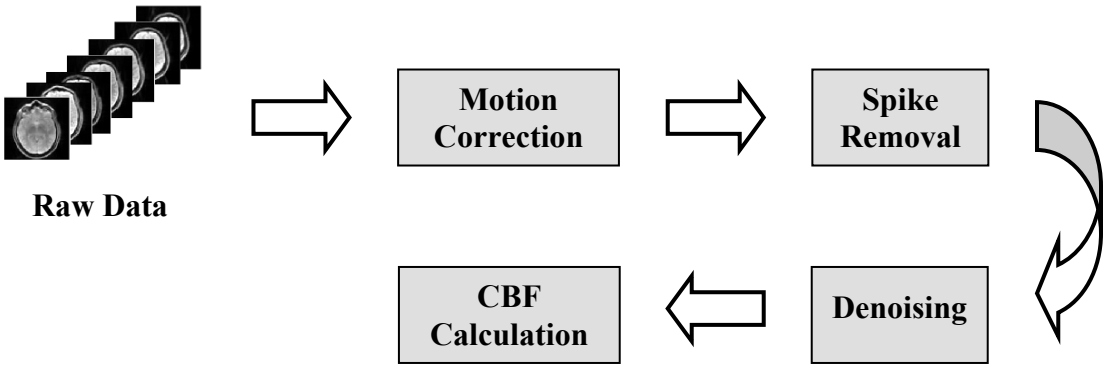

Figure 3.7 Diagram of the preprocessing stages.

3.2.1 Motion Correction

Motion correction consists of two major steps: image realignment and mathematical adjustment of voxel values to account for movement related intensity changes [91]. Realignment involves estimating the six rigid body motion parameters discussed in Section 3.1 and translating and rotating the images so that they are all aligned with the reference image, which is usually the first image in the series or the mean image. The SPM2 motion detection algorithm takes a least squares approach to estimating the motion parameters that minimize the distance between the corrected

volume and the reference volume. The algorithm then applies a spatial transformation based on these parameters to realign the images, but even after perfect realignment some motion effects remain in the images. Some components of the signal intensity are functions of its current and previous positions in the scanner. These effects cannot be eliminated through realignment alone, so an autoregression-moving average model is used to determine the effects of previous spatial displacements on the voxel signals [91]. The algorithm subsequently adjusts the image intensities to account for the motion effects.

All images analyzed in this work were motion corrected using SPM2 in the first preprocessing step. The images were realigned slice-by-slice, i.e., each slice in an image was realigned to the corresponding slice in the reference image, to reduce artifacts that sometimes arise in the ASL images after realigning entire volumes to one another.

3.2.2 Spike Removal

While motion correction removes the majority of the imaging artifacts due to a subject's movements during scanning, the image realignment process is not perfect, so there may still be mismatches in the alignments of adjacent images. During calculation of the perfusion signal, adjacent label and control images are subtracted pairwise. When the images are not perfectly aligned, large spikes in the intensity values can result from subtracting signals from mismatched voxels. Figure 3.8a shows examples of spiking artifacts due to misalignment. These large artifacts can mask signal changes due to brain activations, so localizing brain activations based on these corrupted signals would likely lead to inaccurate results.

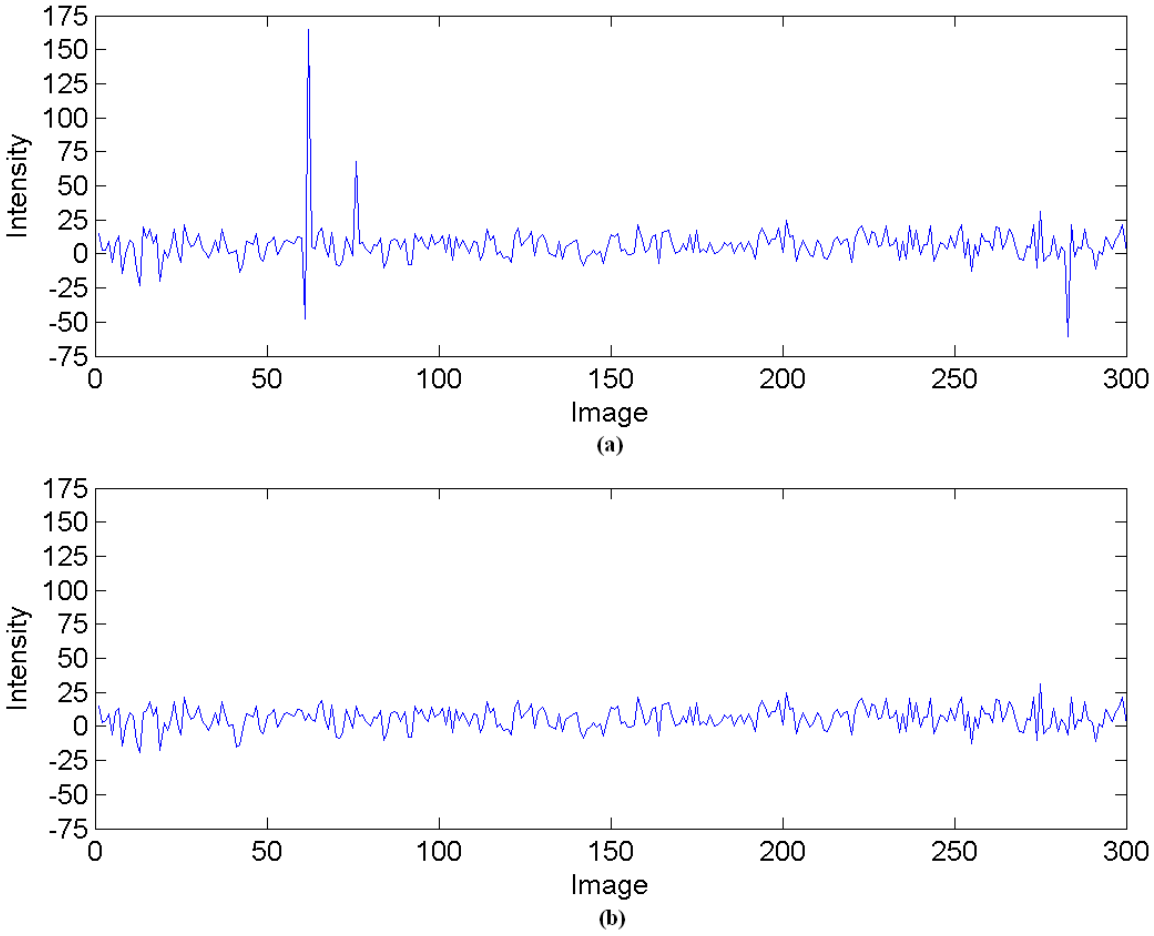

Figure 3.8 The mean perfusion time course of the left hippocampal voxels of Pt5 before (a) and after (b) spike removal. After spike removal, the large spikes have clearly been eliminated while leaving the remainder of the signal relatively unaltered.

The goal of the spike removal preprocessing step was to eliminate these artifactual spikes to ensure that they did not negatively impact the signal analysis results. The spikes were considered outliers in the perfusion time courses that could be detected through analysis of the z-scores of the approximately normally distributed perfusion values. The z-score of a signal x is $z = (x - \text{mean}(x))/\text{std}(x)$. A large absolute z-score at a given point in time is an indication that the signal contains a spike at that point in time.

The absolute values of the z-scores were thresholded to determine which signal values corresponded to spiking artifacts. The threshold was chosen so that time points with z-scores in the top 1% were classified as spikes. Visual inspection of the signal time courses before and after spike removal demonstrated that this threshold choice provided an adequate tradeoff between detecting large spikes and leaving the rest of the signal unchanged. The thresholds for the eight subjects are given in Table 3.3. For Pt5 the threshold of 2.86 means that any perfusion values more than 2.86 standard deviations from the mean of the time course were labeled spikes and subsequently removed.

Table 3.3 Spiking artifact thresholds for each subject.

Subject	**Threshold**
Pt1	2.75
Pt2	2.68
Pt3	2.65
Pt4	3.41
Pt5	2.86
Con1	2.55
Con2	2.66
Con3	2.55

Once the locations of the spikes were known, the next step was to remove the spikes from the affected images. Each outlier in a perfusion time course results from a misalignment between the adjacent label and control images at a certain spatial position. For each voxel, if a spike was found in its perfusion time course, the voxel values in the label and control images at the time of the spike were replaced by the average of the voxel intensities in the label and control images before and after the spike. Let $P(\mathbf{x},n)$ represent the value of perfusion image number n at spatial position $\mathbf{x}$, then

$P(\mathbf{x},n) = C(\mathbf{x},n) - L(\mathbf{x},n)$, where C and L are the control and label series images, respectively. If P(**x**,*n*) was a spike point, then C(**x**,*n*) was replaced by the average of C(**x**,*n+1*) and C(**x**,*n-1*), and L(**x**,*n*) was replaced by the average of L(**x**,*n+1*) and L(**x**,*n-1*). This procedure was performed on all voxels with spikes in their time courses. The spikes were averaged out instead of simply being removed for two reasons: 1) to preserve the temporal dimension of the signals and 2) to reduce the likelihood of introducing new artifacts in the data by concatenating non-consecutive images. Figure 3.8 shows the average perfusion signal in the left hippocampus of Pt5 before and after spike removal.

The result of the spike removal procedure was a set of images without large spiking artifacts in the perfusion series. It should be noted that the images were converted back into label and control pairs instead of being left as perfusion images because perfusion is generally calculated after image smoothing. The spike removal was performed before smoothing so that artifacts in one voxel time course would not be spread into another, but the perfusion images had to be calculated initially during the spike removal stage so that the effects of the label/control mismatch could be determined.

3.2.3 Denoising

The inherently low SNR of fMRI data complicates efforts to localize relatively small signal changes due to brain activations. The goal of image denoising is to increase the image SNR—and consequently increase the sensitivity of activation detection—without introducing excessive blurring in the images that could lead to a large loss of specificity. The three denoising techniques explored in this work are Gaussian spatial filtering, anisotropic diffusion, and a wavelet-based noise removal process.

Gaussian filtering is the most common spatial smoothing method employed in fMRI data analysis. Gaussian smoothing is performed by convolving each point in the image with a 3-dimensional Gaussian response function of the following form:

$$K(x,y,z) = \frac{1}{\left(2\pi\sigma^2\right)^{3/2}} e^{-(x^2/2\sigma_x^2)} e^{-(y^2/2\sigma_y^2)} e^{-(z^2/2\sigma_z^2)} \tag{3.7}$$

where σ_x, σ_y, and σ_z determine the full width at half maximum (FWHM) of the filter, which in turn controls the degree of smoothing in the output image. There is a tradeoff between SNR increase and the amount of image blurring when choosing the filter FWHM. If the FWHM is too great, large numbers of voxels are averaged and activations are spread across many voxels. This reduces the sensitivity of activation detection and decreases the precision of activated voxel localization by effectively increasing voxel size. When the chosen FWHM is too small, there is little SNR gain after filtering, so the filter parameters must be chosen carefully to balance these tradeoffs. An isotropic 8 mm FWHM Gaussian smoothing kernel was selected here for evaluation because it is a common choice in fMRI analysis.

Anisotropic diffusion, introduced by Perona and Malik in [96], addresses some of the problems associated with Gaussian spatial smoothing. To retain sharp edges in the image while still filtering out noise, anisotropic diffusion incorporates an "edge stopping" function, g(·), which influences the filter response at discontinuities in the image. The discrete version of the anisotropic diffusion equation is as follows:

$$I(s,t+1) = I(s,t) + \frac{\lambda}{|\eta_s|} \sum_{p \in \eta_s} g\left(\nabla I_{s,p}\right) \nabla I_{s,p} \tag{3.8}$$

where $I(s,t)$ is a discretely sampled image, s is the voxel position, and t represents the current time step in the iterative filtering process. The scalar λ determines the rate of

diffusion, η_s is the spatial neighborhood of voxel *s*, and $|\eta_s|$ is the number of neighboring voxels. $\nabla I_{s,p} = I(p,t) - I(s,t), p \in \eta_s$ is an approximation to the image gradient magnitude in a particular direction.

The choice of edge stopping function can greatly affect the outcome of image smoothing and edge preservation. Perona and Malik proposed two edge stopping functions:

$$g(x) = \mathrm{e}^{-(x^2/\kappa^2)} \tag{3.9}$$

$$g(x) = \frac{1}{1 + \frac{x^2}{\kappa^2}} \tag{3.10}$$

For large values of *x*, both of these functions approach 0, so for large image gradient values, such as would occur at discontinuities in the image, the diffusion is stopped and sharp edges are preserved. The parameter κ is selected based on the noise level and edge preservation needs. As κ grows, the amount of blurring at the edges increases. The number of iterations of the algorithm also influences the degree of noise reduction and edge strength. Gerig et al. found that Equation 3.9 affords much greater edge enhancement while providing comparable noise suppression ability to Equation 3.10 [97]. They also determined that $\kappa \in (1.5 \cdot \sigma_{noise}, 2 \cdot \sigma_{noise})$ resulted in adequate noise reduction and edge maintenance. Based on these findings, anisotropic diffusion was implemented here using the edge stopping function in Equation 3.9, $\kappa = 2 \cdot \sigma_{noise}$, and five iterations.

The wavelet domain noise filtering technique proposed by Pižurica classifies wavelet coefficients from noisy images as representative of important image

characteristics or as simply noise [98]. This preliminary classification allows the PDF of the noise-free image coefficients to be estimated and gives an indication of local spatial activity. With the local activity information, the coefficients can be adapted to spatial image context for detail retention. This algorithm has a single user defined input parameter K that balances protection of important image detail against adequate noise reduction. Pižurica et al. found that $K = 2$ was optimal in terms of SNR improvement for MRI data [98].

The SNR values of the collected scans before and after noise removal were calculated using Equation 3.4. The mean SNR values for each dataset are summarized in Table 3.4. All three of the denoising techniques resulted in SNR improvement. For six of the eight subjects, wavelet domain denoising achieved the greatest increase in average SNR. Anisotropic diffusion outperformed the standard Gaussian filter in most cases. Based on these numbers alone, one might decide that the wavelet-based methodology is the best signal enhancement technique, but as seen in Table 3.5, for some images this method actually reduced image SNR although it also yielded the greatest SNR increases. Gaussian smoothing and anisotropic diffusion, on the other hand, always increased the SNR range. The wavelet technique also introduced large artifacts into image slices in some cases. Figure 3.9 shows the slices of a single image before and after denoising. The Gaussian filter introduced significant blur into the image, while anisotropic diffusion was able to preserve edges and other detail. The wavelet domain filter provided reasonable edge maintenance for one slice but completely blurred another slice. Because of the aforementioned drawbacks to the wavelet technique and the blurring caused by Gaussian smoothing, anisotropic diffusion was utilized to enhance all images in this

work. No conclusions were drawn about the superiority of one method over another because different choices for the parameters could potentially have altered the findings on which filter performed the best.

Table 3.4 The SNR values (mean ± standard deviation) in dB for the ASL images before noise removal and the resulting SNRs after denoising via an 8 mm FWHM Gaussian smoothing kernel, anisotropic diffusion, and the wavelet-based technique.

Subject	Unsmoothed	Gaussian Smoothing	Anisotropic Diffusion	Wavelet Denoising
Pt1	41.27 ± 1.23	44.83 ± 1.15	46.22 ± 1.07	45.89 ± 5.04
Pt2	37.98 ± 1.61	41.65 ± 1.95	43.22 ± 1.67	46.95 ± 2.48
Pt3	40.14 ± 1.10	44.05 ± 1.34	44.37 ± 1.22	46.19 ± 3.12
Pt4	38.44 ± 2.04	42.63 ± 2.59	43.66 ± 2.53	42.94 ± 8.71
Pt5	44.12 ± 2.14	47.99 ± 1.89	48.54 ± 1.88	51.24 ± 2.45
Con1	37.26 ± 0.60	39.67 ± 0.53	40.25 ± 0.46	41.64 ± 1.33
Con2	37.20 ± 1.21	40.78 ± 1.08	40.52 ± 0.80	44.27 ± 1.16
Con3	44.71 ± 1.03	49.75 ± 1.43	50.47 ± 1.25	53.37 ± 2.84

Table 3.5 The range of the SNR values ([minimum, maximum]) in dB for the images before noise removal and after using each of the three techniques.

Subject	Unsmoothed	Gaussian Smoothing	Anisotropic Diffusion	Wavelet Denoising
Pt1	[37.99, 44.15]	[41.59, 47.52]	[42.97, 48.95]	[32.65, 60.17]
Pt2	[34.72, 42.75]	[37.86, 47.80]	[38.84, 47.71]	[35.23, 53.23]
Pt3	[37.01, 43.35]	[39.50, 47.59]	[40.26, 47.62]	[30.85, 53.88]
Pt4	[28.75, 43.80]	[31.92, 48.40]	[29.66, 48.15]	[30.81, 60.69]
Pt5	[39.52, 49.18]	[43.19, 53.08]	[42.06, 52.44]	[34.72, 59.76]
Con1	[35.67, 38.77]	[37.93, 41.00]	[39.00, 41.27]	[29.86, 45.47]
Con2	[34.25, 42.51]	[38.11, 44.07]	[38.36, 43.01]	[41.53, 46.98]
Con3	[41.81, 47.91]	[46.31, 54.76]	[46.08, 53.56]	[38.46, 61.72]

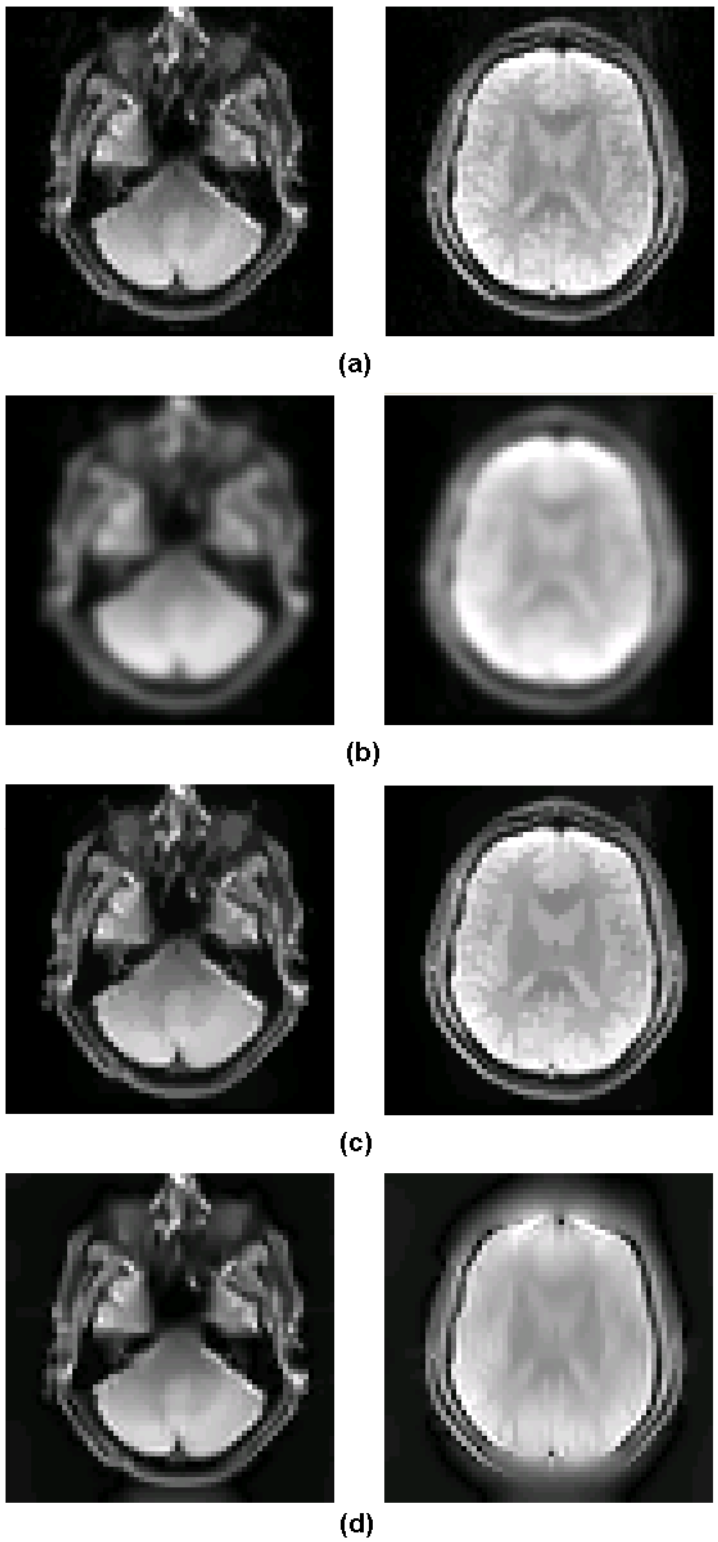

Figure 3.9 This figure displays two slices from an image before filtering (a) and after application of a Gaussian filter (b), anisotropic diffusion (c), and wavelet domain denoising (d). The anisotropic diffusion filter appears to do the best job of preserving fine image details.

3.2.4 CBF Calculation

The final step before signal analysis was calculation of the CBF images. The raw ASL images were first converted into perfusion images through pairwise subtraction of label and control images as discussed previously. The perfusion images had to be scaled in a nonlinear fashion before physiological measures of blood flow could be extracted. The CBF images were calculated using the following equation:

$$CBF = \frac{\lambda \Delta M R_{1a}}{2\alpha M_{con}\{\exp(-wR_{1a}) - \exp[-(\tau + w)R_{1a}]\}}$$

where ΔM is the perfusion image, M_{con} is the average control image intensity, and λ, R_{1a}, α, and w are determined by scan parameters [99]. The images resulting from this calculation had voxel intensities that represent CBF in units of mL/100g/minute. All of the subsequent analyses were performed on the CBF data.

3.3 Feature Extraction

Features are measures of signal attributes that are used to compress raw data into smaller, more informative sets of data for classification, pattern recognition, and machine learning applications. For large datasets, analyzing the raw signals themselves can be computationally expensive and even impractical. By examining features of signals, the most important characteristics of these signals can be gleaned and some of the irrelevant information can be discarded. Feature extraction is therefore a key step in any classification problem. In fact, when a highly representative set of features is selected, the choice of a classifier becomes almost immaterial [100].

The features described below were chosen based on their proven usefulness in the study of other physiologic signals and in signal processing in general [101-105]. Features

were selected from the time, statistics, information theory, and frequency domains to reveal some of the most important signal characteristics. In the following equations, x represents the signal samples, N is the length of the signal, p is the signal histogram, P_{xx} is the power spectral density (PSD) of x, and $X(f)$ is the Fourier transform of x.

- *Energy*: measures the average instantaneous energy in the signal.

$$\frac{1}{N}\sum_i x_i^2$$

- *Curve Length*: sum of the lengths of the vertical line segments between samples. It provides measures of both time and frequency characteristics.

$$\sum_i \left| x_i - x_{i-1} \right|$$

- *Nonlinear Energy*: provides information about amplitude and frequency content of a signal. It is also known as Teager's energy [103].

$$\frac{1}{N}\sum_i \left(x_i^2 - x_{i+1} \cdot x_{i-1} \right)$$

- *Katz Fractal Dimension*: measures the number of elemental units comprising a curve. It is useful for detecting transients in a signal [105, 106].

$$\frac{\log_{10}(N-1)}{\log_{10}\left(\frac{\max_i \left(\sqrt{(x_i - x_1)^2 + i^2} \right)}{\sum_i \sqrt{(x_i - x_{i-1})^2 + 1}} \right) + \log_{10}(N-1)}$$

- *Mean*: average (arithmetic mean) of the signal amplitudes.

$$\mu = \frac{1}{N}\sum_i x_i$$

- *Variance*: measure of the dispersion of the amplitude values.

$$\sigma^2 = \frac{1}{N}\sum_i (x_i - \mu)^2$$

- *Skewness*: measure of the asymmetry of the data distribution.

$$\frac{1}{N}\sum_i \left(\frac{x_i - \mu}{\sigma}\right)^3$$

- *Kurtosis*: measure of how prone to outliers the signal distribution is.

$$\frac{1}{N}\sum_i \left(\frac{x_i - \mu}{\sigma}\right)^4 - 3$$

- *Interquartile Range*: measures statistical dispersion in the signal amplitudes. It is difference between the 75th and 25th percentile samples in *x*.
- *Spectral Entropy*: measure of the randomness in the frequency spectrum of a signal.

$$-\sum_i P_{xx} \times \log_2(P_{xx})$$

- *Shannon Entropy*: measure of the randomness in the time signal.

$$-\sum_i p_i \times \log_2(p_i)$$

- *Renyi Entropy*: measure of the randomness in the time signal.

$$\frac{1}{1-q}\log_2 \sum_i p_i^q$$

- *Complexity*: measures disorder in a sequence using the procedure described in [107].
- *Median Frequency*: frequency at which equal amounts of the spectral power lie above and below.

$$f_{med} \ni \sum_{f=0}^{f_{med}} |X(f)|^2 = \sum_{f=f_{med}}^{\infty} |X(f)|^2$$

- *Mean Frequency*: frequency that is the centroid of the PSD.

$$\frac{\sum_f f \cdot |X(f)|^2}{\sum_f |X(f)|^2}$$

- *Peak Frequency*: frequency at which the PSD reaches its maximum value.

$$f_{\max} = \arg\max_f |X(f)|$$

3.4 Feature Selection and Fusion

Seemingly, having more information about the samples from the two distributions to be classified would improve the overall classification accuracy; however, this is not always true. Correlations in the features used in classifying data and noise in these features can increase the probability of misclassifications. For this reason, feature selection and fusion techniques were exploited in order to determine the best sets and combinations of features for accurately distinguishing epileptogenic and non-epileptogenic voxels.

3.4.1 Feature Selection Techniques

The features presented in Section 3.3 formed the basis for the library of signal attributes investigated for discernment of epileptogenic and non-epileptogenic brain regions. The aim of feature selection was to find a feature subset of size $d < D$ (where D is total number of features in the library) that had the greatest ability to distinguish

between the two classes of voxels. Because the goal was to maximize the classification performance, the classification accuracy was selected as an appropriate objective function for evaluating the feature subsets. The four feature selection approaches employed in this work include:

- Sequential forward selection (SFS)

  SFS is a greedy search algorithm that determines the best set of features for extraction by starting from an empty set and sequentially adding a single feature to the subset if it increases the value of the chosen objective function.

- Sequential backward selection (SBS)

  SBS is similar to SFS but works in the opposite direction. The search initializes with the full set of features and removes a single feature that improves or minimally worsens the objective function to obtain the best subset of features.

- Sequential floating forward selection (SFFS)

  SFFS addresses the tendency of SFS and SBS to gravitate toward local minima due to the inability to re-evaluate the usefulness of features that were previously added or discarded. SFFS performs a dynamically chosen number of forward selection steps followed by backward selection as long the objective function increases. The process then repeats until the desired number of features has been selected.

- Branch and bound (B&B)

  B&B is an exponential search algorithm with the ability to find "optimal" solutions under certain assumptions and conditions [108]. The algorithm creates a tree structure such as the one shown in Figure 3.10. Then, based on the

assumption that the superset always has a higher objective function value than its subsets—which is not always true—the algorithm is able to eliminate certain branches of the tree as possible best solutions without evaluating them. In this way, the optimal solution can be found without an exhaustive search of the feature space.

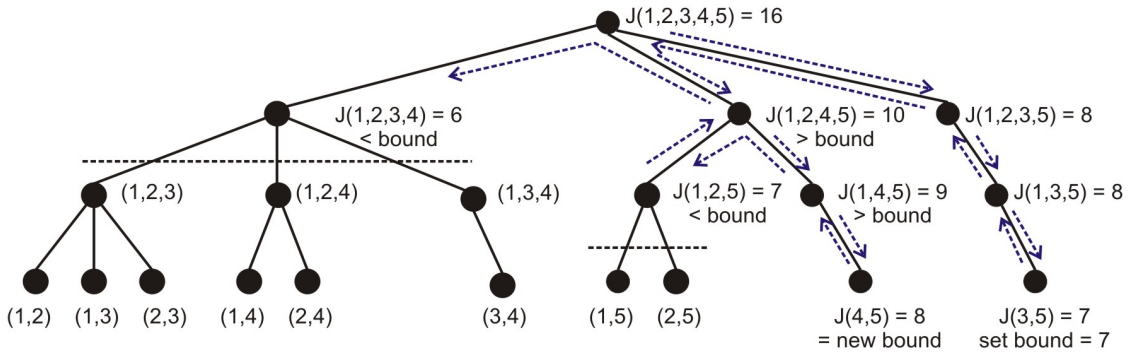

Figure 3.10 Example of a branch and bound search tree for $D = 5$ and $d = 2$. The dashed black lines represent the points at which branches can be pruned in order to reduce the computational burden without loss of optimality, and the arrows represent the order of tree traversal starting from the right.

3.4.2 Genetic Programming for Feature Fusion

In addition to exploring feature selection routines for determining the best sets of features for discriminating between the epileptic and non-epileptic brain regions, genetic programming (GP) was also exploited as a means of fusing separate features. The goal in feature fusion is to create a single composite feature with superior ability to discriminate between the two classes than the component features.

Genetic programming is a machine learning technique that employs an evolutionary algorithm to generate a globally "optimal" program to solve a given problem [109, 110]. Evolutionary algorithms apply genetic operators such as

reproduction, mutation, crossover, and selection to find optimal solutions from populations of candidate solutions, also known as individuals or chromosomes. Individuals are assessed through evaluation of a fitness (objective) function, which gauges the individual's ability to solve the given problem. In other words, fitness is a measure of how well an individual can predict the systems outputs from the inputs. The output of the GP algorithm is the individual with the best fitness.

GP is an extension of genetic algorithms (GA), but there are a few key differences. First, unlike GA, which finds a direct solution to a problem, GP outputs a program that can then be used to solve the given problem. In the algorithms standard form, variably sized GP programs are represented as tree structures; on the other hand, GA chromosomes typically are fixed-length and represented as strings or vectors of binary or real values. Because the size of individuals is not fixed in GP, the algorithm is capable of creating both simple and highly complex individuals. A simple example a GP tree is shown in Figure 3.11. The gray nodes represent functions, and the white nodes represent terminals. Functions are arithmetic, mathematical, Boolean, or conditional operators, and terminals are user inputs to the GP algorithm and constants.

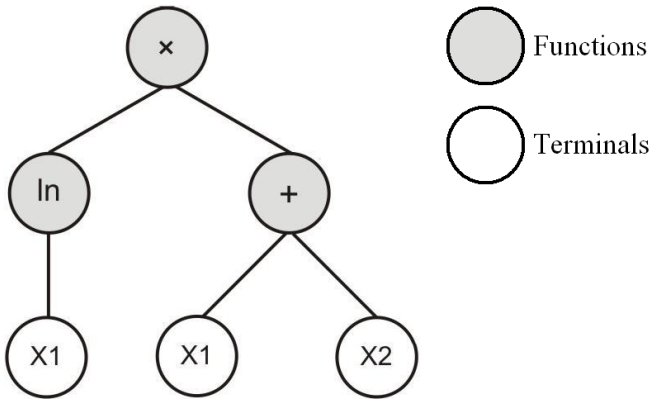

Figure 3.11 An example of a GP tree structure encoding the function $ln(X1)\times(X1 + X2)$.

The GP algorithm evolves programs through an iterative process, which is depicted in Figure 3.12. Each iteration of the algorithm is known as a generation. During the initial generation, randomly generated individuals populate the solution space. With each new generation, the population is diversified through crossover, mutation, and selection operations. Selection involves choosing a set of individuals from the larger population based on a fitness criterion. These individuals then form an intermediate population and are either varied through crossover and mutation operations or proceed to the next generation unaltered via reproduction. In a crossover operation, two new individuals (offspring) are produced as combinations of two parents. This is accomplished by selecting a node in each parent tree and then swapping the subtrees branching from those nodes. Figure 3.13 depicts a typical crossover operation. Like crossover, mutation operations also generate new offspring; however, mutation involves only a single parent. In a mutation operation, as shown in Figure 3.14, a subtree is selected and replaced by a randomly generated tree to create a new individual. Once the new population has been created through the aforementioned genetic operators, the survival stage chooses the fittest individuals from this population of parents and children to go on to the next generation. The process of creating new populations continues until the maximum number of generations is reached or until a stop criterion, such as a specified fitness level, is met.

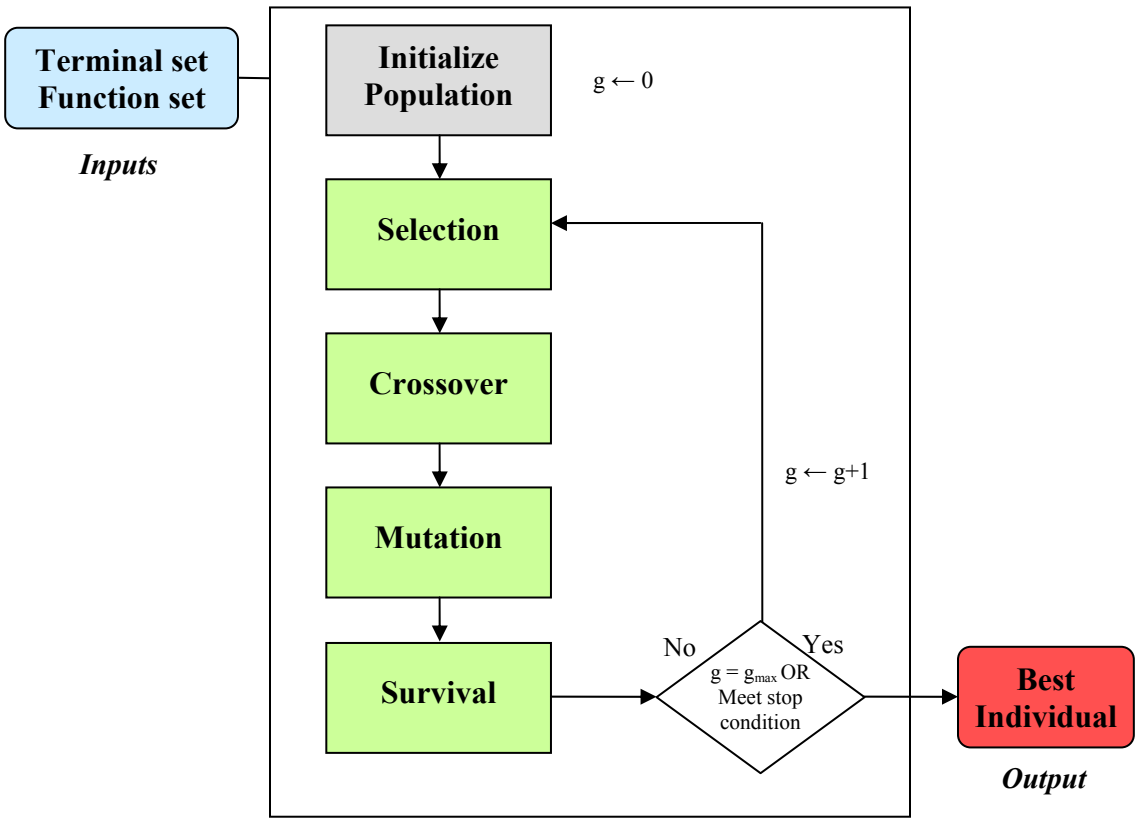

Figure 3.12 Graphical representation of the GP algorithm.

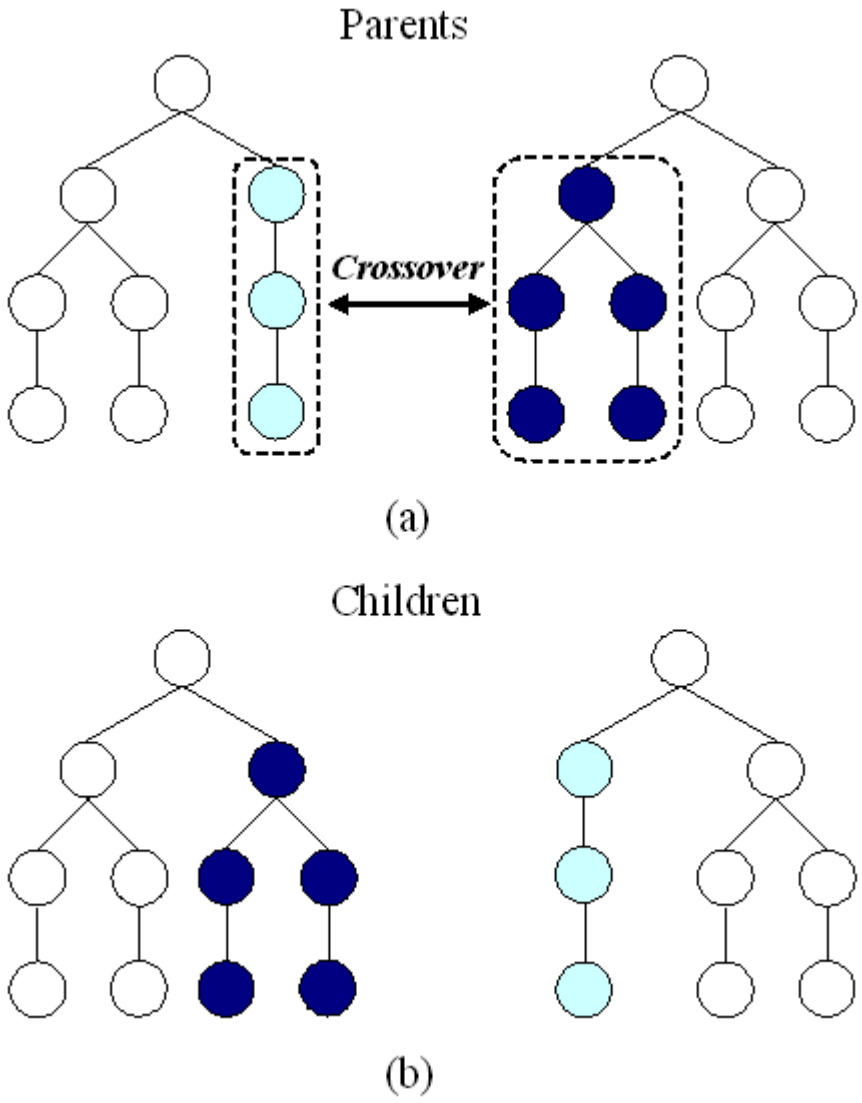

Figure 3.13 Illustration of a GP crossover operation. (a) Individuals whose subtrees are swapped. (b) The new individuals resulting from the crossover.

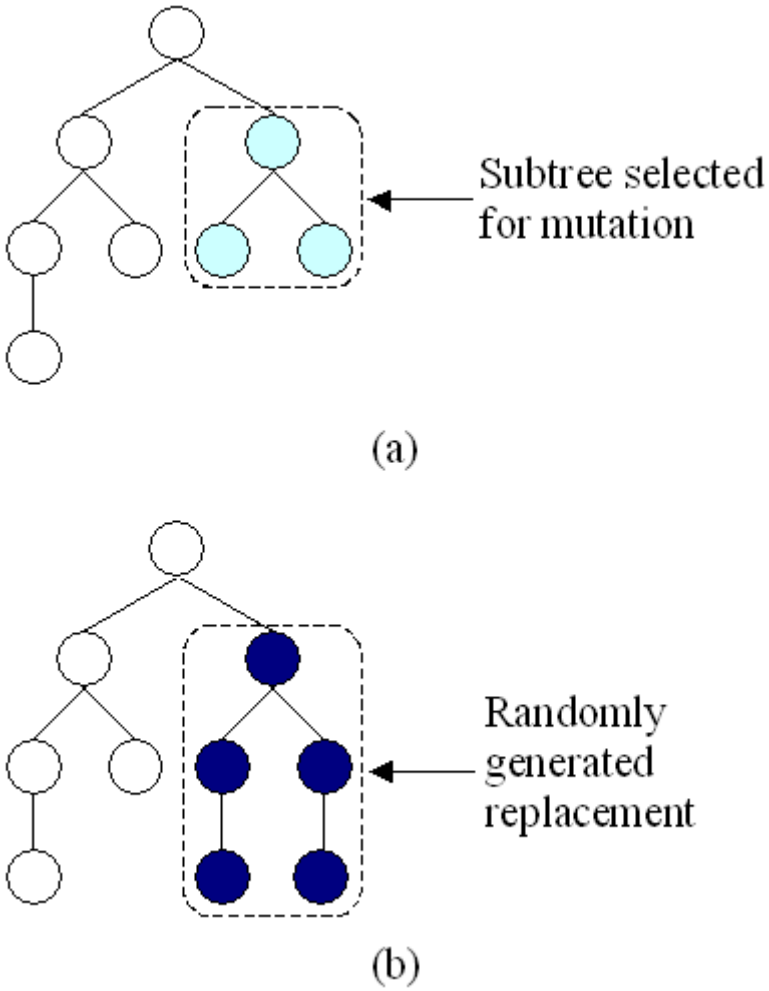

Figure 3.14 Illustration of a GP mutation operation. (a) Individual with subtree selected for mutation. (b) New individual created through mutation.

Table 3.6 List of functions supplied to the GP algorithm and their respective symbols.

Function	**Symbol**
Addition	+
Subtraction	−
Multiplication	×
Division	÷
Absolute Value	$\lvert\ \rvert$
Square root	$\sqrt{\lvert\ \rvert}$
Square	$(\ )^2$
Natural logarithm	$\ln(\lvert\ \rvert)$
Sine	sin
Cosine	cos
Arctangent	atan

When applying GP to the problem of feature fusion, the feature library became the terminal set and the functions listed in Table 3.6 were supplied to the GP algorithm for creating feature combinations. The output was the best composite feature found during the evolutionary process. The chosen fitness metric, given in Equation 3.11, provided an indication of the separation between the prior probability distributions of the two classes. It therefore served as an indirect measure of the performance that could be achieved when classifying voxels based on the composite feature.

$$fitness = \frac{\left|\mu_1 - \mu_0\right|}{\sqrt{\left(\sigma_1^2 + \sigma_0^2\right)}} \cdot \left(1 - overlap\right) \tag{3.11}$$

The first part of the equation is Fisher's discriminant ratio (FDR), which measures class separability. The variables μ_i and σ_i^2 are the mean and variance, respectively of the two class PDFs. The higher this ratio is the greater the distance between the two classes. The FDR alone, though, is not always a good indicator of class separability in the case of multi-modal probability distributions. The addition of the overlap term provides a means of addressing this issue. The overlap is defined as

$$overlap = \int \min\left(p(\mathbf{y} \mid \mathbf{c} = 0), p(\mathbf{y} \mid \mathbf{c} = 1)\right) dy \tag{3.12}$$

where **y** is a column vector of feature values, **c** is a column vector of class labels (either 0 or 1) for each corresponding observation in **y**, and $p(\mathbf{y} \mid \mathbf{c} = i)$ is the PDF of the feature **y** given that all observations in **y** belong to class *i*. As the PDF overlap approaches 0, the fitness is solely governed by the FDR value. For classes with significant overlap, the fitness is decremented proportionally to the amount of overlap. Figure 3.15 shows examples of feature PDFs for low and high fitness cases.

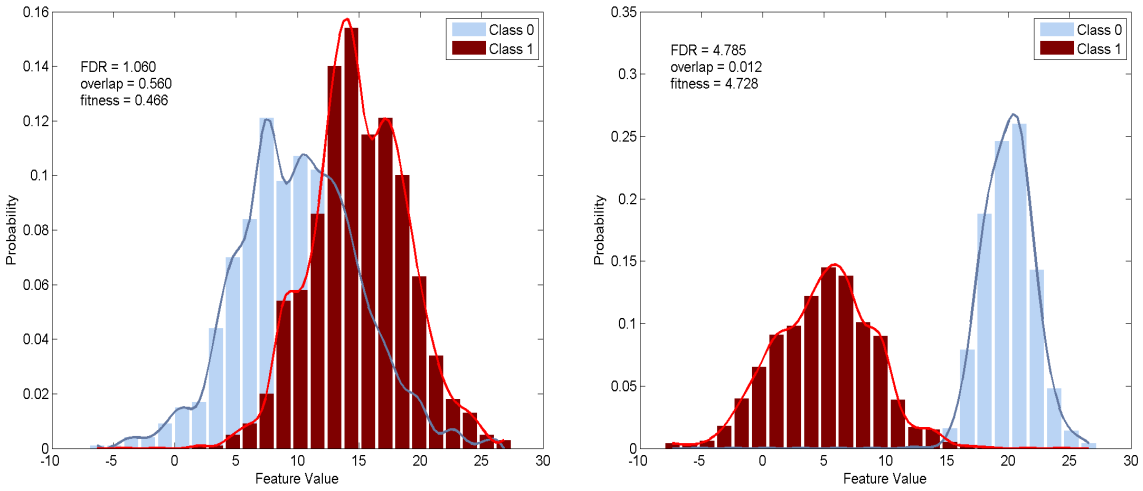

Figure 3.15 PDFs for features with low fitness (*left*) and high fitness (*right*). The separation between the two classes is much clearer for high fitness feature, thereby making accurate classification based on this feature easier.

3.5 Classification

As mentioned previously, the emphasis in this work is on the selection of the best features for distinguishing the characteristics of epileptogenic and non-epileptogenic voxels. If the features are chosen wisely, any classifier should be able to accurately separate the two classes. Under this assumption, a simple *k*-nearest neighbor (*k*-NN) rule was employed to classify voxels based on their feature values. *k*-NN classifiers are nonparametric architectures that find the *k* training samples in the feature space closest to the testing data based on some distance metric (e.g., Euclidean distance). Then a simple majority rule vote determines the class label of the testing point. This process is illustrated in Figure 3.16.

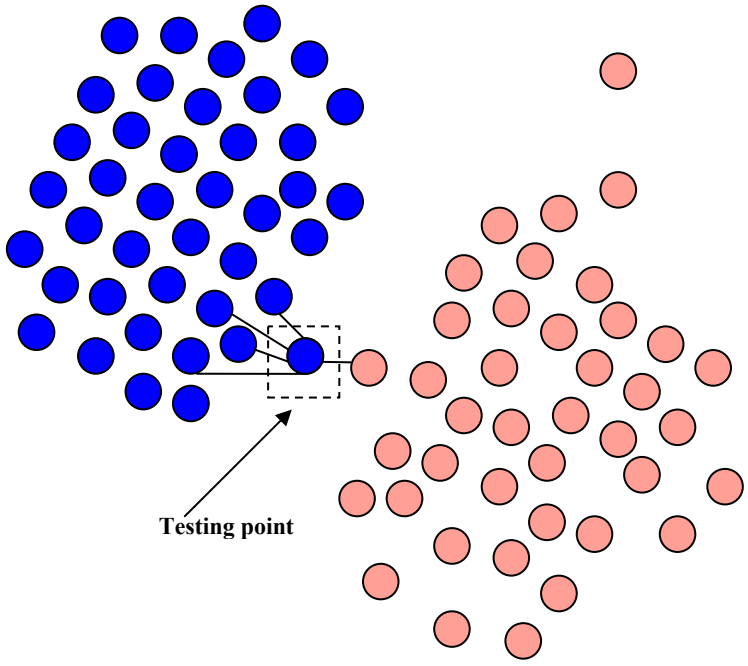

Figure 3.16 Illustration the *k*-nearest neighbor classification process. The testing point is assigned to a class based on the classes of the *k* closest training points. In this example $k = 5$. The testing point is labeled as blue because four of its five nearest neighbors are blue.

3.6 Performance Metrics

To evaluate the accuracy of the activation detections and the usefulness of the extracted features, various performance metrics can be assessed. These metrics provide quantitative measures of how good the detection system is at distinguishing between epileptogenic (or more generally activated) and non-epileptogenic (or non-activated) voxel time courses. The four possible outcomes of the system are:

1. True positive (*TP*) − the detector correctly identifies a voxel as being activated.
2. False positive (*FP*) − the detector mistakenly identifies a voxel without activations present as being activated.
3. True negative (*TN*) − the detector correctly identifies a voxel as not being activated.
4. False negative (*FN*) − the detector mistakenly identifies a voxel as not being activated.

Key detector performance metrics can be derived by determining the numbers of occurrences of each of these outcomes.

- $Sensitivity = \frac{TP}{TP + FN}$ is a measure the system's ability to correctly identify the activated voxels (positives).
- $Specificity = \frac{TN}{TN + FP}$ is indicative of the system's ability to recognize the non-activated voxels (negatives).

Sensitivity and specificity provide indications of not only the overall classification accuracy, but also the error rate for each class. In cases of unbalanced classes, the accuracy alone is not always representative of the true performance. The recognition rate

of the smaller class could be close to 0, but the system could still have high overall classification accuracy. Examining sensitivity and specificity alleviates this problem.

Using these metrics, receiver operating characteristic (ROC) curves can be generated. ROC curves, as illustrated in Figure 3.17, provide a visual representation of the tradeoff between sensitivity and specificity for various classification thresholds on the features. The ROC curve of a perfect classifier is a straight line from the origin (sensitivity = 0, specificity = 1) to the upper left-hand corner (sensitivity = 1, specificity = 1) and from there to the upper right hand corner (sensitivity = 1, specificity = 0), while the ROC curve of a random guess classifier is a straight line from the origin to the point the (1,1). The area under the curve (AUC) offers a metric of the quality of a classifier with a given ROC curve. The larger the AUC is, the better the classifier. A perfect classifier has an AUC of one, and a random guessing classifier has an AUC of 0.5.

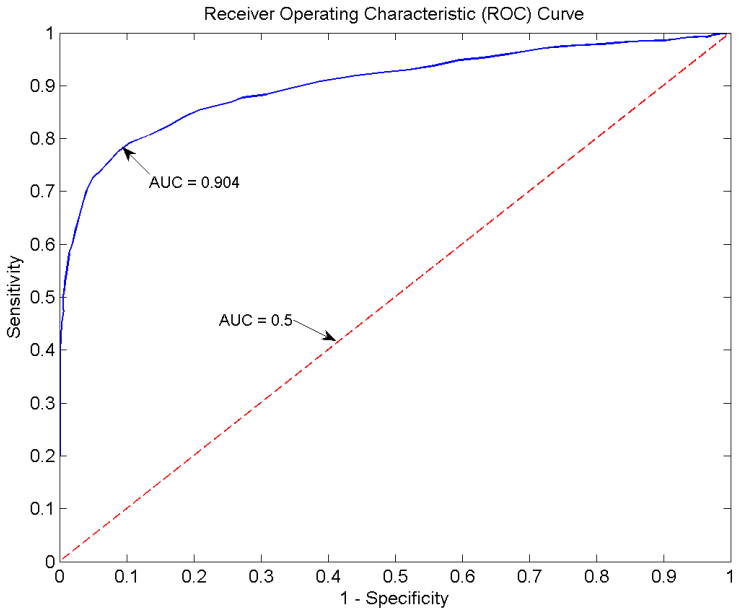

Figure 3.17 Examples of ROC curves and their corresponding AUC values. The dashed line represents a random guessing classifier with an AUC of 0.5. The solid line with higher AUC represents a much better classifier.

3.7 2dTCA

In addition to the methods described in the previous sections, the 2dTCA technique introduced in Section 2.5 was implemented and applied to all fMRI datasets to serve as a benchmark. The purpose of applying this algorithm is to establish the timings of irregular transient signal changes occurring simultaneously in large numbers of voxel time courses [76]. To that end, the algorithm creates a two-dimensional histogram showing the number of voxels undergoing a signal change of at least 1.5 standard deviations above the average time signal as a function of time. The x-axis signifies the times of first substantial signal increase, and the y-axis denotes the times at which significant signal changes occur. For example, a dataset with 100 images results in a histogram, $hist_{2d}(x,y)$, of size 100 × 100, such as the one illustrated in Figure 3.18. The value of $hist_{2d}$ at location (x,y) indicates the number of voxels with first significant signal increase in image x that experienced an event in image y. By having all voxels with the same initial signal increase time contribute to the same column of the histogram, voxels with similar responses are grouped together.

Each column of the histogram is referred to as a reference time course (RTC). Peaks in the RTC represent times at which substantial numbers of voxels experience considerable deviations from the signal mean. The most significant RTCs can be determined by examining the diagonal of $hist_{2d}$. The times at which the diagonal values are highest are the times at which significant numbers of voxels experience similar signal changes. These large, widespread changes may be indicative of times of brain activations due to stimuli or spontaneous brain dysfunction. The number of RTCs created by the 2dTCA algorithm varies depending on the data and is only limited by the number of

images in the time series. The example in Figure 3.18 has significant peaks at time points 10 and 51. At all other points in time only a few voxels experience their first transient event, so these RTCs are deemed unimportant because the effect is isolated, not widespread. The RTCs corresponding to the notable event timings are shown in Figure 3.19.

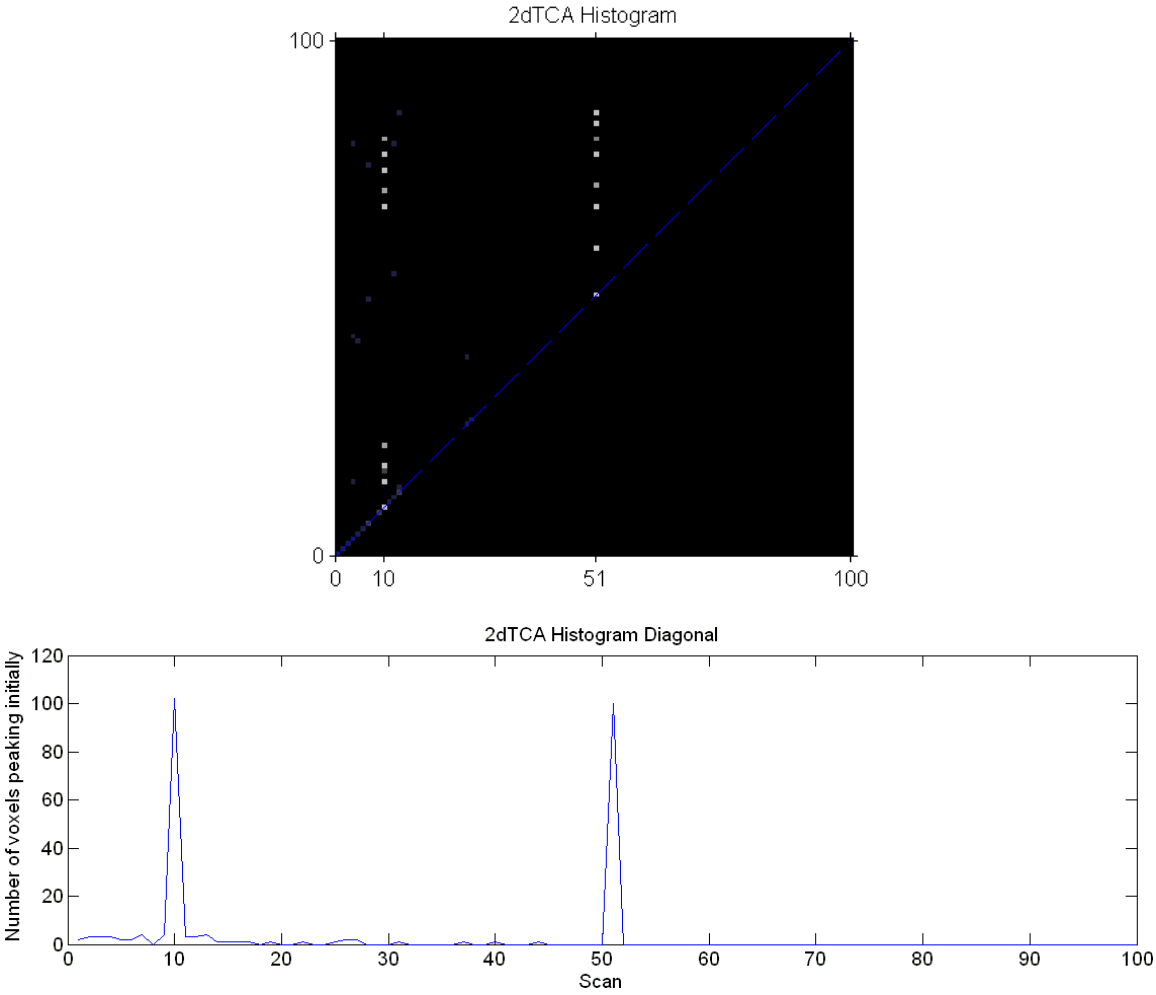

Figure 3.18 A 2dTCA histogram for a dataset containing 100 images. By examining the diagonal of the histogram (blue dashed line), the most significant RTCs can be determined and extracted from the corresponding columns. A plot of the values along the diagonal reveals two time points at which large numbers of voxels peak.

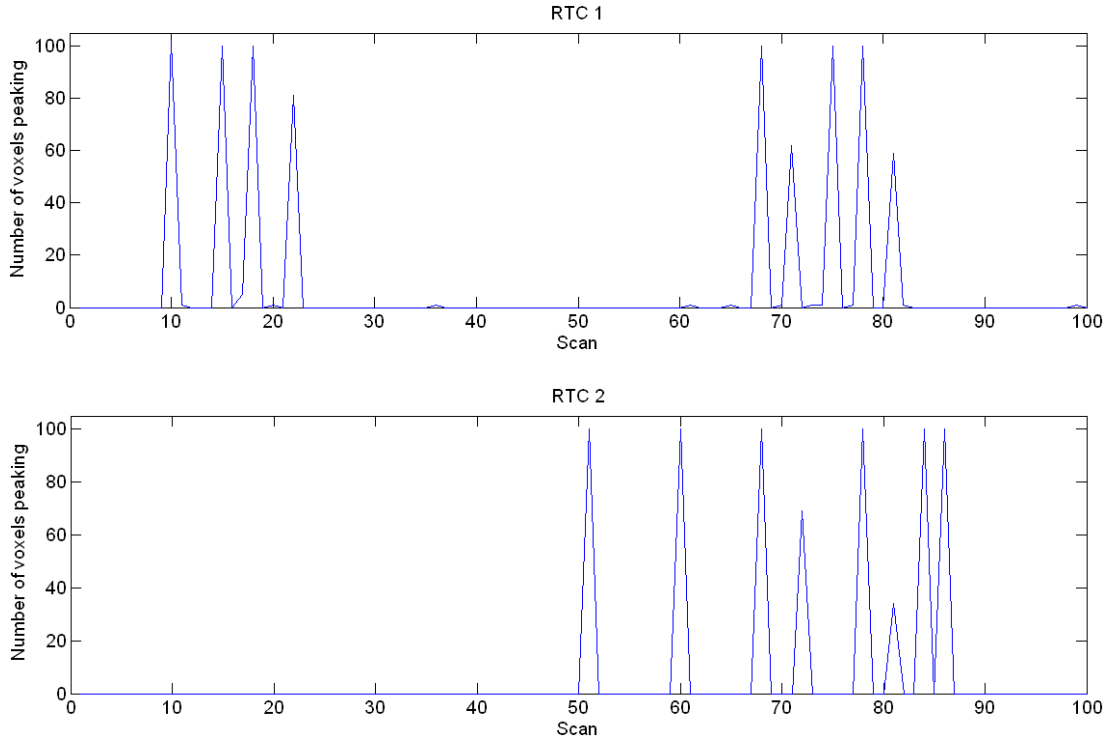

Figure 3.19 The two most significant RTCs extracted from the histogram illustrated in Figure 3.18. RTC 1 and RTC 2 represent the signal responses of voxels with initial peaks at time points 10 and 51, respectively.

Once the RTCs are found, they are normalized and used as regressors in the general linear model (GLM) along with motion parameters and the global time signal to perform fixed-effects analysis [5]. This statistical analysis approach attempts to model each voxel time course as a linear combination of the regressors. Voxels with time courses more like the regressors are assigned higher t-values in the statistical parametric map (SPM) generated by the procedure (cf. Appendix A). By thresholding these t-maps, the areas of activation corresponding to the individual RTCs can be determined. All voxels with t-values greater than the threshold are deemed activated. Each RTC represents a signal response due to a separate source and generates a separate activation map.

CHAPTER 4

PHANTOM DATA RESULTS

This chapter presents the results of analyzing features of fMRI voxel time courses to detect simulated functional activations embedded in phantom images. The importance of processing phantom data with known areas of activation was to validate the functional analysis tools developed in this work and provide confidence in the results obtained when examining in vivo data with uncertain activations. An overview of the phantom data characteristics and details of the experimental methods are presented. Key results and performance metrics for the newly developed methodology and techniques previously formulated by other researches are also presented and discussed.

4.1 Phantom Data Overview

Using the procedure outlined in Section 3.1.2, fifteen phantom datasets were produced for analysis in this work. Each generated dataset consisted of 400 images with an assumed repetition time of 6 seconds. Figure 4.1 shows an example of a voxel time course extracted from the simulated data along with a real fMRI time course for comparison. The HRF, noise levels, motion characteristics, areas of activation, and spiking frequency were varied amongst the datasets to model the differences in brain function that would be found between epilepsy patients. The HRF characteristics, with the exception of maximum percentage signal change, were altered only slightly between datasets as these subtle differences were not deemed likely to significantly affect the results. Low levels of random motion were added to the data with the intention of

replicating what would be seen in a cooperative subject remaining reasonably still during scanning. The most significant variations between the datasets were in the maximum signal change, noise variance (and consequently SNR), and locations of added activations. These important data characteristics are summarized in Table 4.1.

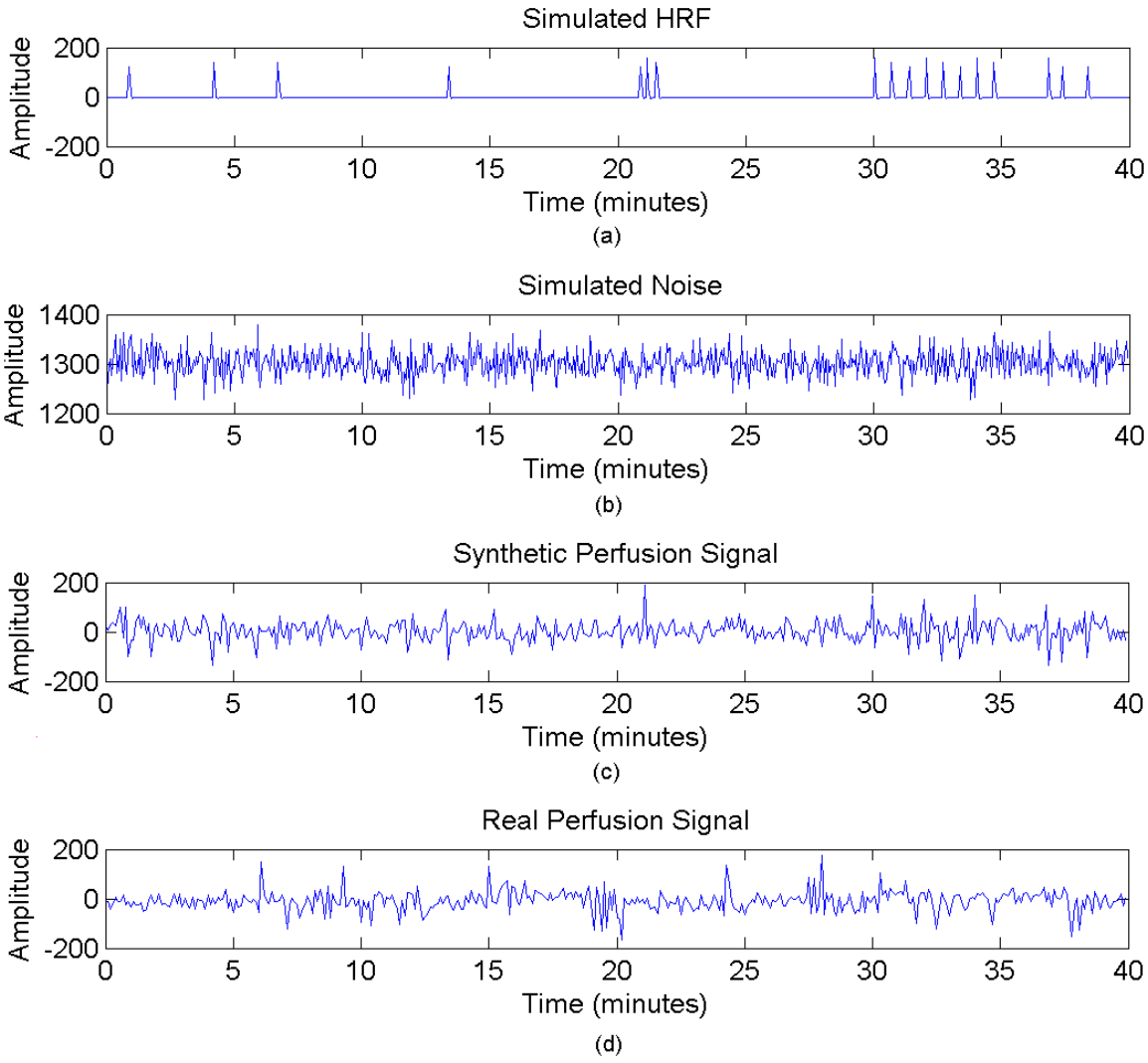

Figure 4.1 (a) A simulated hemodynamic response based on the sum of two gamma functions model. (b) A baseline signal with added Rician noise. (c) The voxel perfusion signal generated by adding noise to the modeled HRF and performing pairwise subtraction between adjacent label and control images. (d) A perfusion time course extracted from the epileptogenic hippocampus of a TLE patient.

Table 4.1 Summary of important phantom dataset attributes.

Subject ID	Maximum Signal Change	Average Raw Image SNR	Focus #
S1	20%	43.167	4
S2	20%	38.740	2
S3	20%	37.150	3
S4	18%	43.127	4
S5	18%	40.671	3
S6	18%	38.730	1
S7	15%	43.175	2
S8	15%	40.661	3
S9	15%	40.635	1
S10	12%	43.167	3
S11	12%	40.654	2
S12	12%	40.645	2
S13	10%	43.154	4
S14	10%	37.063	1
S15	10%	45.096	3

Table 4.1 lists for each patient the focus number, which describes the areas of activations for that particular patient. Four masks defining the brain regions in which the activations were to be embedded were created using by the WFU Pickatlas toolbox for Matlab [111-113]. All masks are combinations of the left and right mesial temporal lobe templates available in Pickatlas. The MTL template masks were produced by combining the amygdala, hippocampus, and parahippocampal gyrus. The first mask, referred to as focus 1, defined the epileptogenic region as the left MTL. Focus 2 included the entire left MTL and 20% of the right MTL voxels. Focus 3 consisted of approximately 75% of the left MTL, and focus 4 included 80% of the left MTL plus 20% of the right MTL. Masks with both left and right side activations were created to make the focal regions more realistic in that even for patients with unilateral TLE, the contralateral (opposite side) lobe is also often dysfunctional to some degree. Figure 4.2 shows several slices of the

MTL masks utilized in the data simulations. The red and white shaded regions indicate the left and right MTL voxels, respectively.

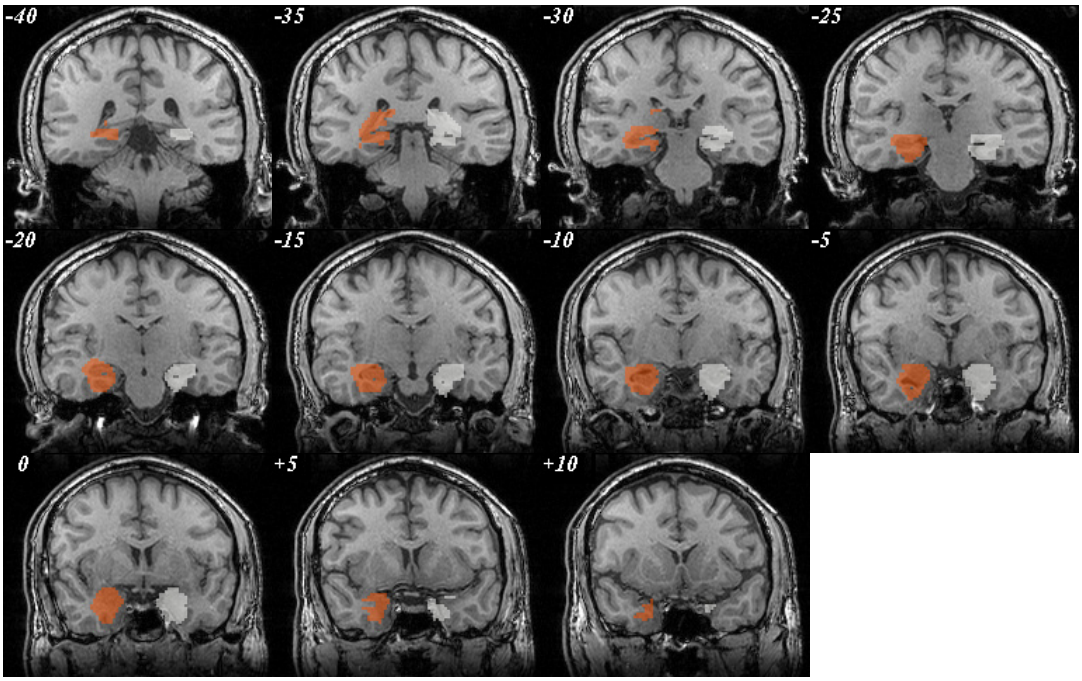

Figure 4.2 Coronal view of the MTL template mask slices overlaid on a high-resolution anatomical scan. This image, as well as all subsequent images, is displayed in the neurological convention, meaning the left side of the image corresponds to the subject's left side. The number in the corner of each slice indicates the distance in mm along the z direction from the origin of the image.

4.2 2dTCA Experiments

The 2dTCA technique detailed in Section 3.7 was implemented and applied to the simulated datasets. The results of these experiments provided a benchmark for evaluating the performance of the feature-based analysis discussed in subsequent sections.

For each of the fifteen phantom datasets, 2dTCA was applied to find a set of RTCs estimating the hemodynamic response to significant spontaneous activity in the

brain. Each RTC, such as the one illustrated in Figure 4.3, was then used as a regressor in a GLM analysis performed using SPM2 software, and activation t-maps were generated. These maps were analyzed to determine the locations of functional activation in the fMRI data. This was accomplished by thresholding the maps to find the brain regions with responses most similar to the RTC under investigation. Thresholding provided a level confidence in rejecting the null hypothesis of no activation (cf. Appendix A). All voxels with intensities, i.e., t-values, less than the chosen threshold were deemed inactive, while voxels with intensities greater than the threshold were deemed active. The higher the t-value the more likely the voxel was truly activated and the less likely the similarity between the RTC and the voxel time course was simply due to chance.

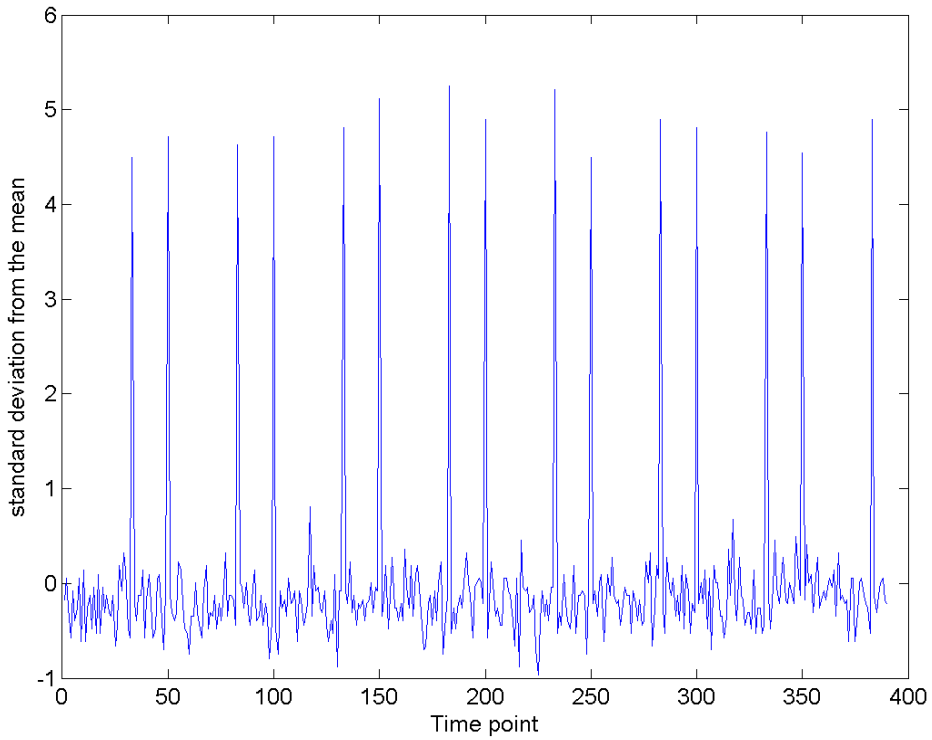

Figure 4.3 A normalized RTC extracted from a phantom dataset using the 2dTCA algorithm.

The thresholded t-map associated with the RTC seen in Figure 4.3 is shown in Figure 4.4. The map is a visual representation of the statistical significance of the activations in each voxel. The red shaded regions indicate voxels with t-values just above the threshold, while the yellow regions signify voxels with the highest t-values. The likelihood of false activations in the yellow areas is lower than in the red regions with lower statistical values. This particular map was thresholded at a level resulting in a false positive activation rate less than 5% ($p < 0.05$ with correction for familywise error). This threshold was chosen when evaluating the maps because it is a commonly chosen statistical inference level in SPM analysis. A different choice of threshold would have yielded a different activated region. The map below shows clear bilateral MTL activation as expected for this dataset with simulated activation time courses in both MTLs.

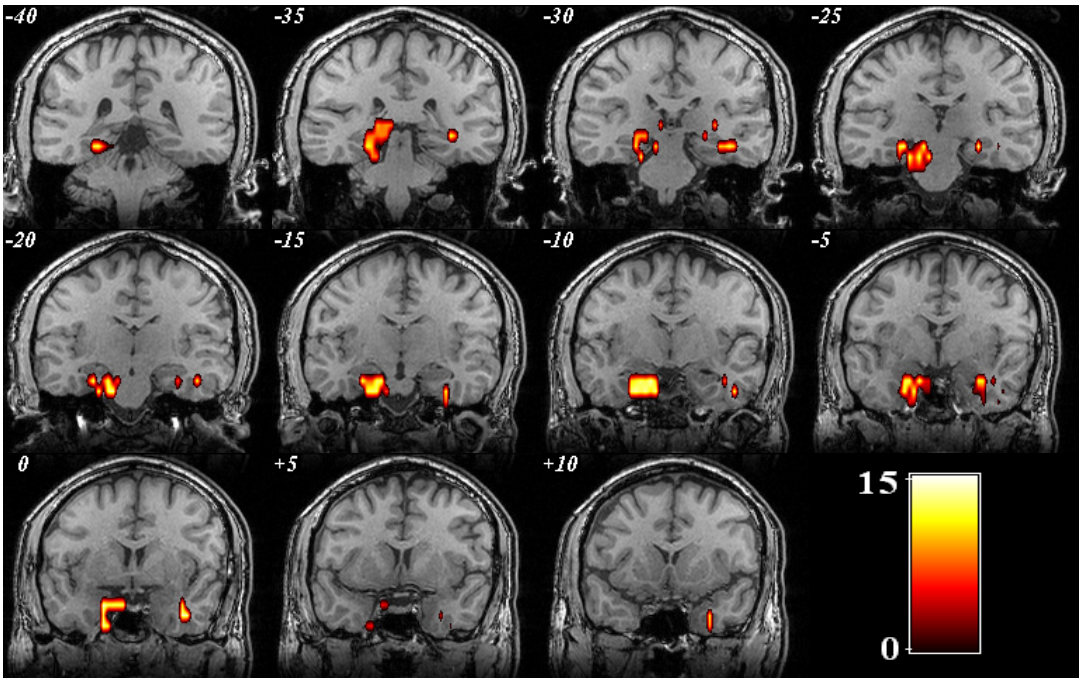

Figure 4.4 Activation t-map ($p < 0.05$, corrected) generated for phantom subject S1 overlaid on the structural scan of the subject. The subject's t-map, with simulated bilateral TLE, shows left and right mesial temporal lobe activations.

To evaluate the ability of the 2dTCA algorithm to accurately identify voxels in the simulated data with embedded activations, ROC analysis was performed. The t-maps corresponding to each RTC were thresholded over a range of values to determine the AUC, which measures the overall usefulness of each t-map as a basis for classifying normal and epileptic brain regions. The maps were also thresholded at the critical value (t_{crit}) resulting in the desired level of statistical significance ($p < 0.05$ with correction for familywise error).

The results of the statistical analysis of the fifteen phantom datasets evaluated in this work are summarized in Table 4.2. For each subject the number of RTCs yielding maps with statistically significant activations, the maximum AUC over all of the RTCs, and the sensitivity and specificity at the critical threshold are reported.

Table 4.2 The results of the 2dTCA experiments for the phantom data. The maximum AUC obtained for any of the maps is reported in addition to the sensitivity and specificity when thresholding the statistical map at t_{crit}.

Subject	Number of RTCs	Maximum AUC	Sensitivity At t_{crit}	Specificity at t_{crit}
S1	2	1.00	100.00%	100.00%
S2	7	1.00	100.00%	99.99%
S3	2	1.00	100.00%	100.00%
S4	1	1.00	100.00%	100.00%
S5	3	1.00	100.00%	100.00%
S6	3	1.00	100.00%	100.00%
S7	8	0.93	0.00%	99.99%
S8	4	1.00	87.96%	100.00%
S9	3	1.00	96.58%	100.00%
S10	1	0.53	0.00%	99.94%
S11	0	—	—	—
S12	2	1.00	100.00%	99.99%
S13	0	—	—	—
S14	4	0.54	0.00%	99.98%
S15	2	1.00	100.00%	100.00%

The results of these experiments demonstrate the ability of the 2dTCA algorithm to accurately localize the areas of activation in simulated fMRI data in many cases. For ten of the fifteen datasets, the maximum AUC over all of the RTCs for that subject was 1, indicating that when the threshold was properly chosen, the map accurately identified voxels as active or inactive. However, it is important to note that the activations were not always statistically significant ($p < 0.05$). For instance, at the critical threshold, the sensitivity of the classifier is only 87.96% for subject S8. Lowering the threshold would increase the sensitivity but at the expense of statistical significance. The other RTCs, which yield lower classification accuracies, represent voxel activations due to sources other than the simulated epileptic time courses. These other sources include image noise and motion artifacts remaining after motion correction.

The classification results for the five other phantom subjects were much less accurate. Subject S7 had one RTC exhibiting high classification accuracies for certain thresholds but no statistically significant true positive activations (sensitivity = 0% at t_{crit}). The maximum AUC values for subjects S10 and S14 were close to 0.5, meaning that classification of voxels based on these t-maps would be essentially random and therefore not useful. Finally, for subjects S11 and S13, none of the RTCs yielded maps showing statistically significant voxel activations, whether true or false positives.

The previously mentioned failures to localize the areas of embedded activations were due to the inability to find an RTC similar to the true activation time course. Figure 4.5 shows both the true normalized RTC and the RTC generated by the 2dTCA algorithm for subject S10. The two RTCs were notably different, so they produced completely different activation maps. On the other hand, the true RTC and the 2dTCA generated

RTC for subject S15 contained similar spiking event timings. Consequently, the 2dTCA generated technique produced a highly accurate activation map for this subject.

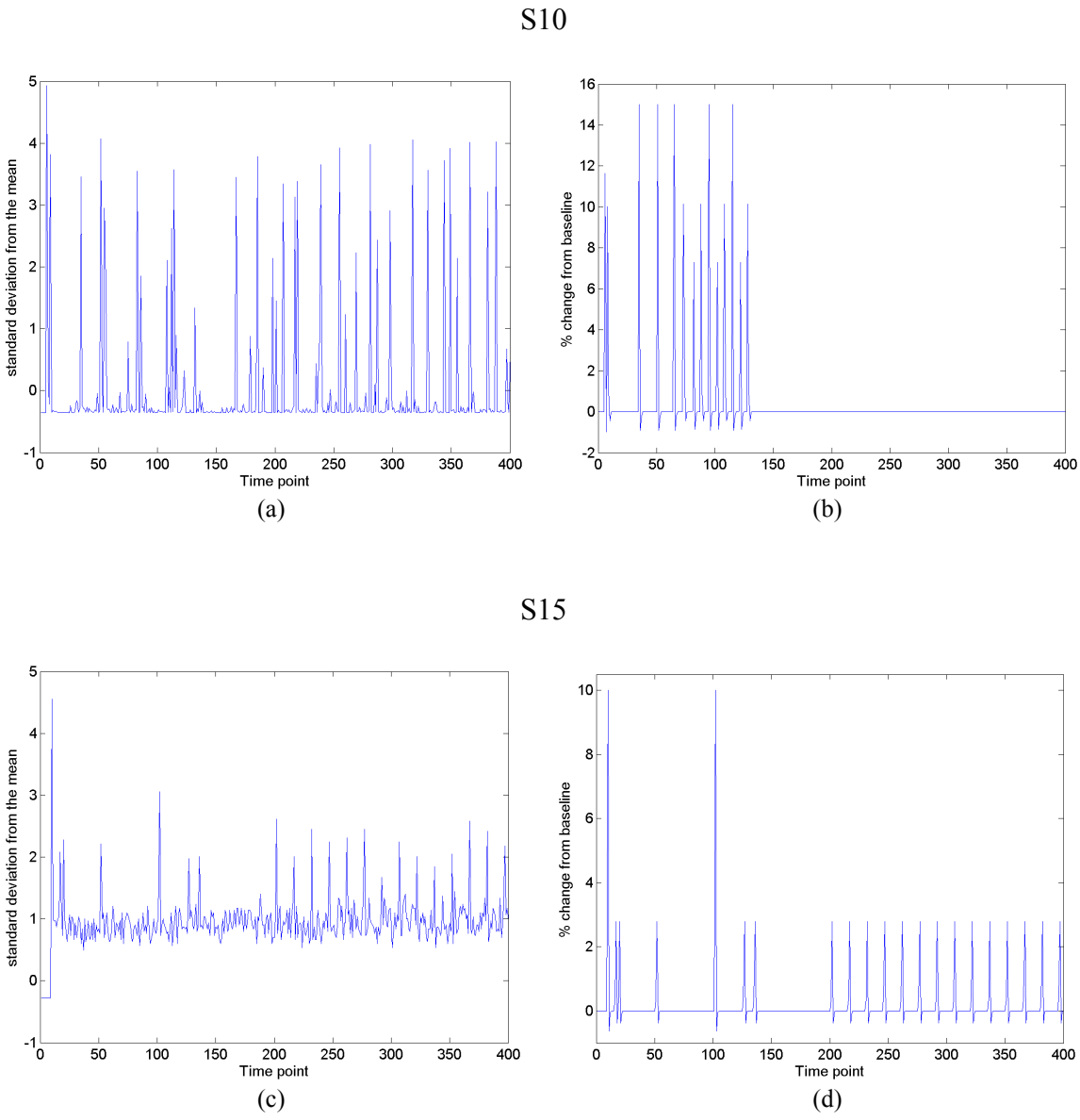

Figure 4.5 Comparison of the true activation time course and the 2dTCA generated RTCs for two phantom subjects. The 2dTCA generated RTC (b) greatly differs from the actual simulated time course (a) for subject S10, explaining the inability to find the areas of activation for S10. On the other hand, for subject S15, the simulated time course (c) and the 2dTCA RTC (d) have similar event timings, so the activated regions were accurately determined based on this RTC.

4.3 Feature Evaluation

The procedure employed to assess the usefulness of featured-based processing of fMRI data to discriminate the differences between baseline brain activity and functional activations due to stimuli is illustrated in Figure 4.6. Initially the phantom data were divided into training and testing sets. For the training set, equal numbers of samples from each class, i.e., epileptic and non-epileptic, were used in order to address the class imbalance problem. In patients with focal epilepsy, the vast majority of the voxels will belong to the non-epileptic class (0) and relatively few will belong to the epileptic class (1). Training based on a balanced set of data helps to alleviate the problem of training the classifier with too few examples of one class, as illustrated in Figure 4.7. In this case, the training set was designed to have class proportions similar to the testing data, i.e., with a few samples from the light blue diamond class and many from the red oval class. When training, the classifier has so few examples of the diamond class as seen in the figure, that when it evaluates the testing data, it assigns all sample points to the same class while still maintaining high classification accuracy because of the small number of misclassified points. Had a balanced training set been used, the classifier would have been more likely to recognize the underrepresented class points and correctly labeled them.

After creation of the training and testing datasets, the features discussed in Section 3.3 were then extracted from each dataset. Each of the feature selection methods presented in Section 3.4 were subsequently applied to the feature sets to determine the best sets of features for distinguishing between the two classes of voxels in the training set. Finally, these feature sets were used as the basis for assigning the testing data to either the epileptic or non-epileptic class.

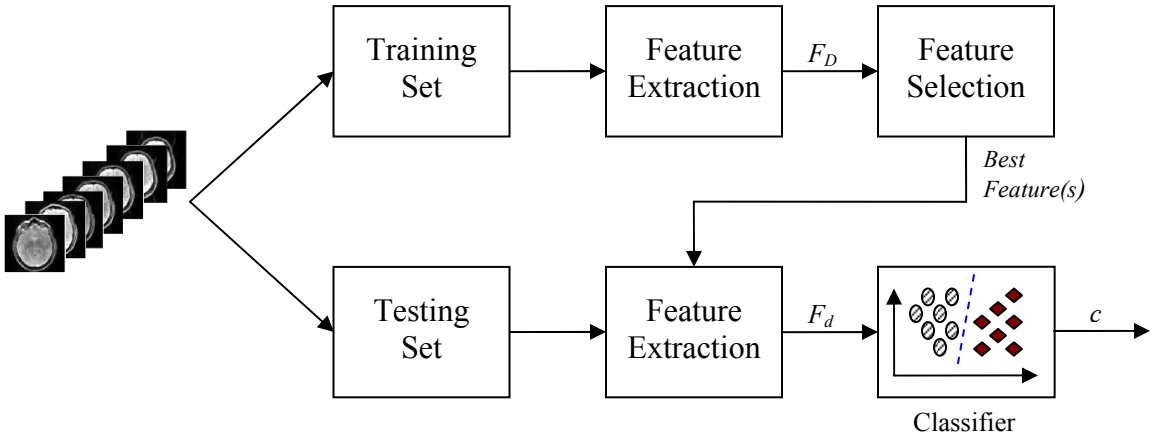

Figure 4.6 Diagram of the feature analysis framework. The functional datasets are divided into training sets, which are evaluated to find the best set of features, F_d, for discriminating epileptogenic and non-epileptogenic voxels. The best feature set is then used as the basis for classifying the testing data.

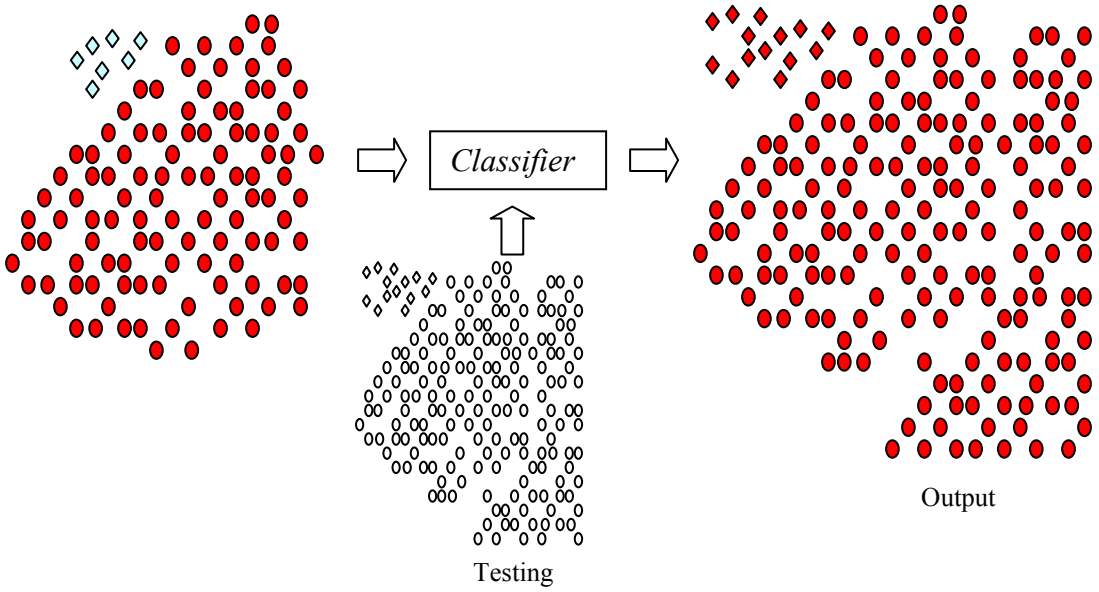

Figure 4.7 Illustration of the class imbalance problem.

For this experiment, the feature evaluation was limited to voxels in the mesial temporal lobes. The phantom data were generated to simulate functional images from patients with TLE, so these tests were designed to demonstrate the ability to discriminate between voxels in the normal and dysfunctional lobes. For all phantom datasets, one-third of the data from the class with the fewest points was included in the training set. The same number of points from the other class was then added to create a balanced training set. All other MTL voxels were included in the testing set. Thirty Monte Carlo simulations were run to statistically validate the approach. Separate randomly selected training and testing sets were created for each dataset and each run and used to create a feature set for subsequent classification of the testing data using a *k* nearest neighbor rule. The sensitivity and specificity were calculated for each simulation to evaluate performance.

To assess the statistical significance of any differences in the performance of the feature selection techniques, a two-way analysis of variance (ANOVA-2) was completed. The subject served as the first factor and the method as the second. The results are illustrated in the box plots in Figures 4.8 and 4.9. From these results, it is evident that no one method consistently outperformed the others, although some methods worked better than others for individual subjects. For subjects S6 and S14, there was no statistically significant difference in the sensitivity or specificity of any of the methods. SFS and SBS provided by far the highest performance for S13, but the best method for subject S15 was GP.

The results of this experiment demonstrate that for the phantom data, all five feature selection and creation methods analyzed here could produce features capable of

accurately distinguishing the two classes of voxels. Another important point to note is that the algorithm was effective for all subjects, even those (S11 and S13) who could not be analyzed using the 2dTCA technique or whose analysis results were poor (S7, S10, and S14).

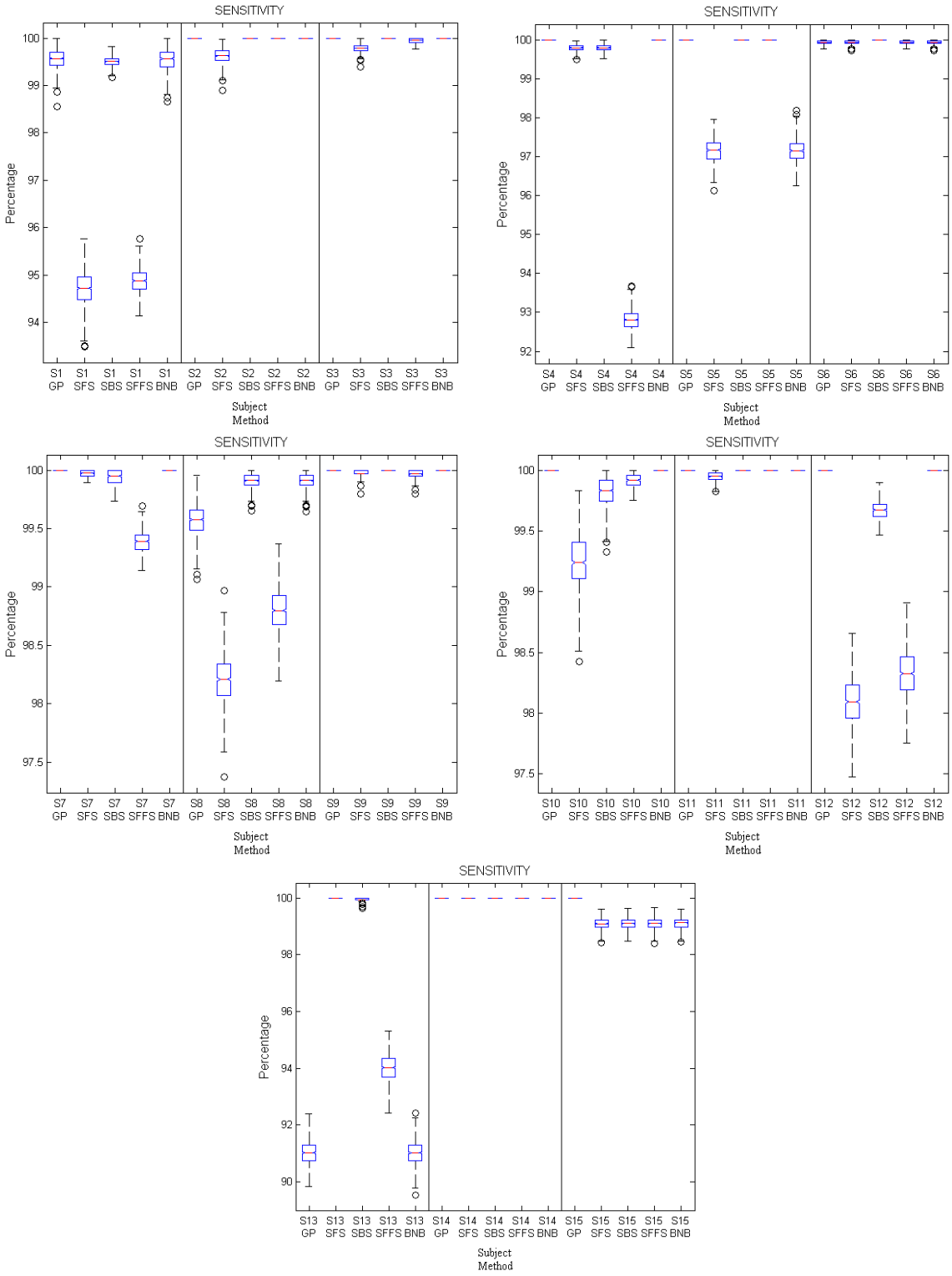

Figure 4.8 This figure illustrates the results of analyzing the performance of feature-based classification of phantom data voxels in terms of sensitivity. The differences between the methods were not always statistically significant, and no one method consistently outperformed the others.

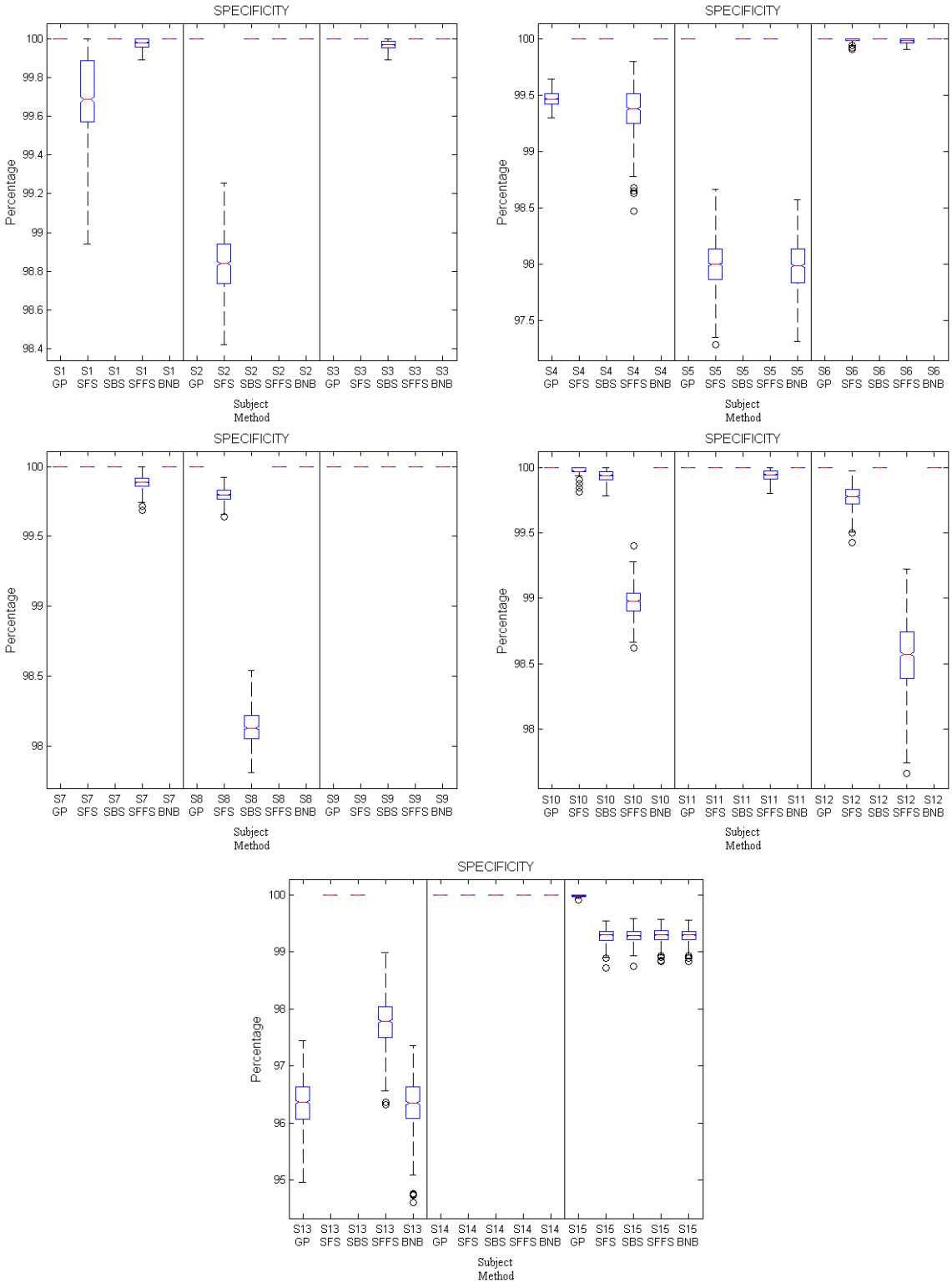

Figure 4.9 This figure illustrates the results of analyzing the performance of feature-based classification of phantom data voxels in terms of specificity. The differences between the methods were not always statistically significant, and no one method consistently outperformed the others.

4.4 Feature Clustering

The results in Section 4.3 demonstrate the ability to discern the time courses of activated voxels from those experiencing baseline activity based on the feature values of the simulated data. Once the usefulness of the features was established, the next logical step was to investigate whether the features could be used to cluster brain regions with similar voxel time courses. The purpose of the experiments in this section was to use the features generated for the previous experiment to cluster voxels with similar feature values in order to create maps showing activated brain regions. In this way, with only limited knowledge about which voxels belong to each class, the algorithm could be used to group voxels with similar characteristics. As was the case for the feature selection stage, separate training and testing sets were created for these experiments, and the training sets were balanced to address the class imbalance problem, which is even greater when the entire image (not just a specific ROI) is evaluated. The training data for the epileptic class were randomly selected from the simulated epileptogenic region, and the samples for the other class were randomly chosen from the set of all other brain voxels. All brain voxels not included in the training set were then added to the testing set.

A spectral clustering approach [114], which does not rely on an explicit model of the data distribution, was chosen for this work because of its effectiveness and simplicity. Spectral clustering techniques involve the creation of a similarity matrix for the data points and use the spectrum of the matrix to perform dimensionality reduction for clustering in a lower dimensional space. The features generated in Section 4.3 were used as the basis for clustering the data for each of the thirty Monte Carlo simulations. The spectral clustering results are summarized in Table 4.3.

Table 4.3 Summary of the results of spectral clustering of the voxels in the phantom images. The maximum sensitivity and specificity over the thirty simulations are given.

Subject	Sensitivity	Specificity
S1	100.00%	100.00%
S2	100.00%	99.95%
S3	100.00%	99.98%
S4	100.00%	100.00%
S5	100.00%	100.00%
S6	100.00%	99.88%
S7	100.00%	100.00%
S8	100.00%	99.99%
S9	100.00%	99.98%
S10	100.00%	100.00%
S11	100.00%	99.099%
S12	100.00%	100.00%
S13	100.00%	100.00%
S14	100.00%	100.00%
S15	100.00%	99.99%

For all fifteen subjects the most accurate map had sensitivity and specificity greater than 99%. Again, even for the subjects whose 2dTCA analysis produced either inaccurate maps or no maps at all, the feature analysis resulted in highly accurate maps for at least one feature set. While these results are impressive, it must be noted that as with the 2dTCA generated maps, not all maps are equally good, so some a priori knowledge about the true epileptogenic zone is needed to separate the correct maps from the others. For instance, if all activations are outside of the temporal lobe for a particular map and the patient is known to have TLE, the map is most likely showing false activations and can be discarded.

4.5 Conclusions

The experiments discussed in this chapter demonstrate the power of feature-based analyses in examining the differences between simulated baseline activity and functional activations in fMRI data. By training on a small subset of the data with known class labels, a set of features was generated for discriminating between the two classes. The remaining voxels were then accurately identified as active or inactive by applying a simple *k*-NN classifier for all simulated datasets. The features generated in the training process were also used to cluster the testing data into two classes based on their feature values. The results of this process were functional maps with nearly perfect accuracies in all fifteen cases. For the data examined in this work, the feature-based analyses proved superior to the 2dTCA technique. While the 2dTCA method was highly accurate in some cases, it produced maps with no sensitivity or failed to generate any maps at all in other cases. On the other hand, the feature-based technique always yielded accurate results.

CHAPTER 5

IN VIVO DATA RESULTS

This chapter provides the results of applying to real subject data the techniques developed and validated in Chapter 4 on the study of phantom fMRI data. The goal of these experiments is to localize any spontaneous epileptiform activity present in the resting imaging data of TLE patients and determine whether the results are concordant with the patient's clinical information.

5.1 2dTCA Experiments

One drawback of the 2dTCA algorithm is that multiple RTCs (and consequently multiple SPMs) are typically produced for each dataset. Without a priori information about the likely areas of activation, the true regions of interest cannot be established. For instance, if analysis of the resting perfusion data of an epilepsy patient resulted in five SPMs, each with different areas of activation, without knowing the patient had TLE, the map corresponding to the epileptic activity could not be determined. In such a case, maps not including temporal lobe activity would be of no interest. Another problem with the algorithm would be determining the most relevant map when multiple maps show temporal lobe involvement but perhaps different extratemporal activations.

For phantom data with known areas of abnormal activity, the aforementioned issues were not relevant. In this case, the exact areas of added activations were known, allowing for statistical analysis of the resultant maps. This was not the case for the in

vivo patient data, so other measures had to be employed to determine which t-maps corresponded to activations in the epileptic onset zone.

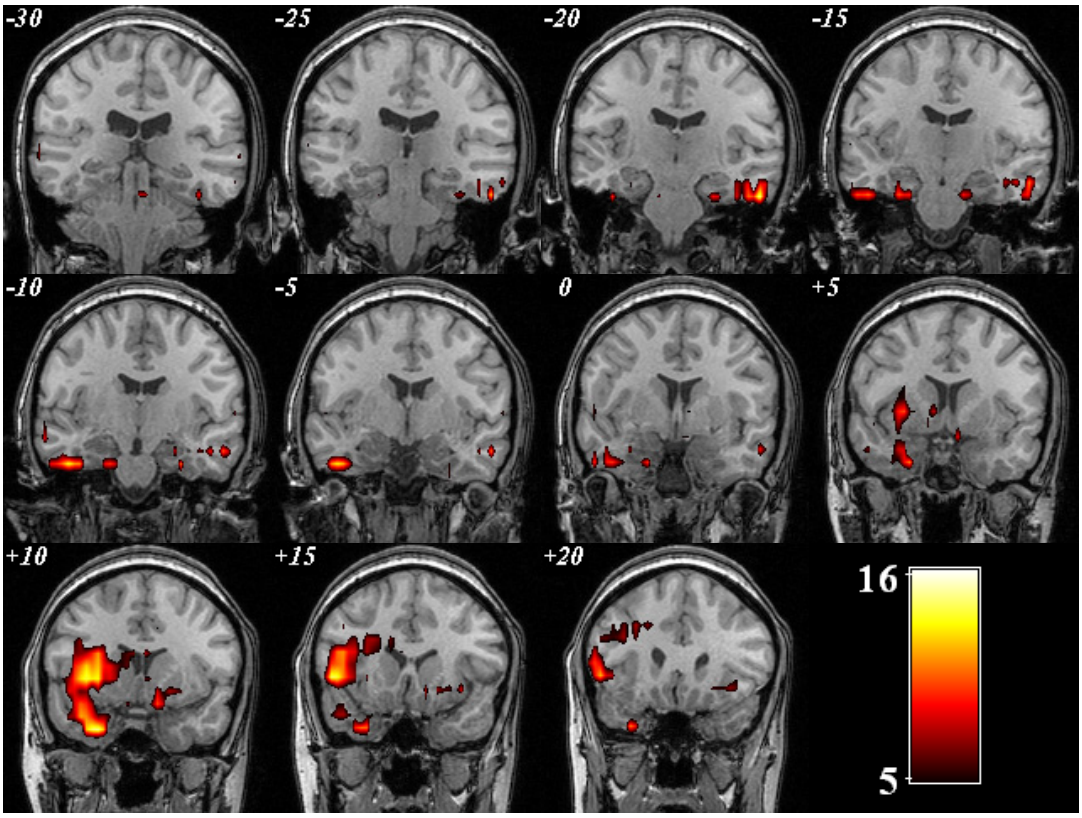

Figure 5.1 Activation t-map (t > 5 with a cluster size of 5) produced using a 2dTCA RTC from Pt1 showing widespread, bilateral brain activations.

Data from each of the five TLE patients and the three healthy controls were evaluated using the 2dTCA algorithm. Multiple RTCs were found for each dataset, and the resultant maps were investigated for the presence of focal activations. When the maps were thresholded at a statistical significance level of $p < 0.05$ with correction for familywise error, most showed widespread activation over both hemispheres. One such map is shown in Figure 5.1. To better localize the significant activations in individual maps, the activation t-levels were increased in increments of one starting at a minimum

of t > 5 and ending when no temporal lobe activation was found. The maps of the maximum t-level containing temporal lobe activations were then further investigated and noted as having left, right, or bilateral mesial and lateral temporal lobe activations. If two maps demonstrated different lateralizations, then both results were reported, and if no activations were present at the minimum t-level, then the subject was deemed to have no TL activations. The results of this analysis are summarized in Table 5.1.

Table 5.1 The results of the 2dTCA experiments for the in vivo data.

Subject	# RTCs	Lateral TL Activation	Mesial TL Activation
Pt1	7	Left	Left
Pt2	11	None	Left
Pt3	11	Left	Bilateral
Pt4	13	Left	Bilateral
Pt5	2	None	Left
Con1	9	Left	None
Con2	9	None	Left
Con3	8	Left	Right

The following subsections review each patient's clinical information and present one 2dTCA generated map for each subject. The maps displayed here were chosen because they had the highest maximum t-level (and statistical significance) for each subject.

5.1.1 Pt1

Pt1 experienced left side interictal spikes and left temporal seizures during EEG monitoring. The MRI results were normal, and the PET scan revealed left TL

hypometabolism. This patient's t-map contained clear left temporal activations, which was concordant with the clinical information.

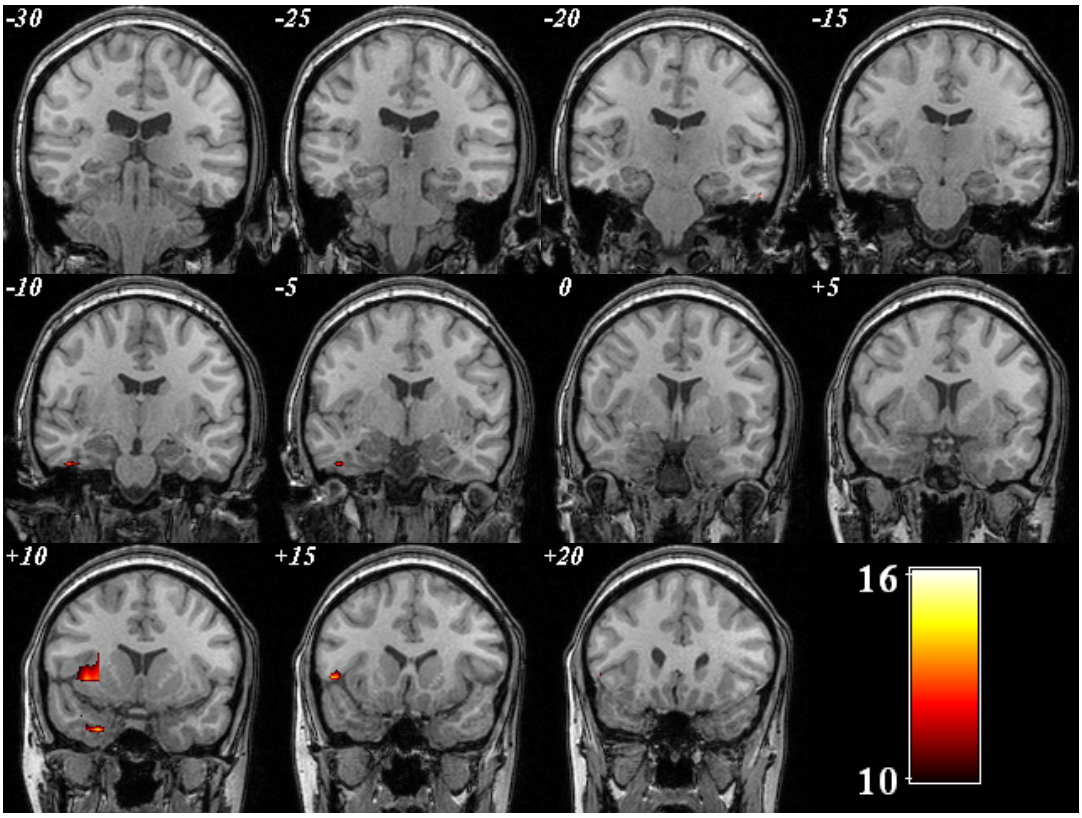

Figure 5.2 Pt1 2dTCA activation t-map (t > 10, cluster size 5) showing left lateral and mesial temporal lobe activations, which corresponds with the clinical results.

5.1.2 Pt2

Pt2 experienced right side interictal spikes and right temporal seizures during EEG monitoring. The MRI scan revealed right mesial temporal sclerosis, and the PET scan showed hypometabolism in the right TL. No significant lateral temporal activations were found in any of the activation maps, but small areas of left mesial temporal activation were found. These findings conflicted with the clinical results. The discrepancies may be due to the low image SNR, a lack of significant spontaneous

epileptic activity during scanning, or other confounding factors such as excessive subject movement during scanning.

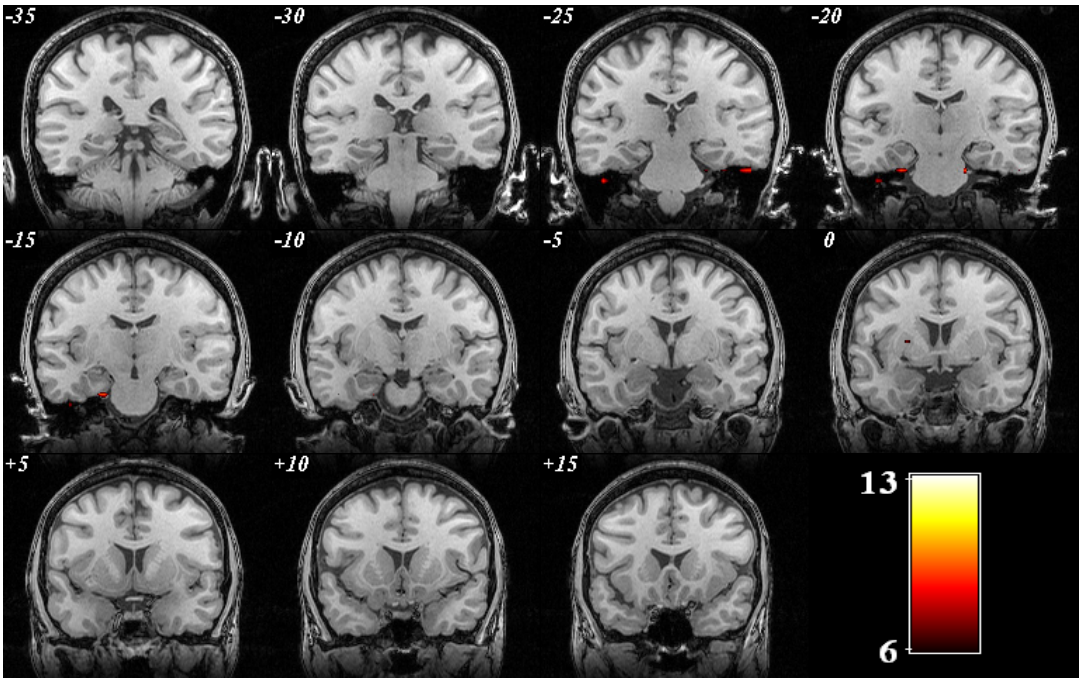

Figure 5.3 Pt2 2dTCA activation t-map (t > 6, cluster size 5) showing a tiny area of left mesial temporal activation. These results are not consistent with the clinical lateralization.

5.1.3 Pt3

Pt3 experienced left side interictal spikes and left temporal seizures during EEG monitoring. The MRI results were normal. PET scan results were not available for this patient. The map below showed left temporal activations as expected but also small areas of right mesial temporal activation. The t-values of these activated right MTL voxels were relatively low, so the meaning of these activations was unclear.

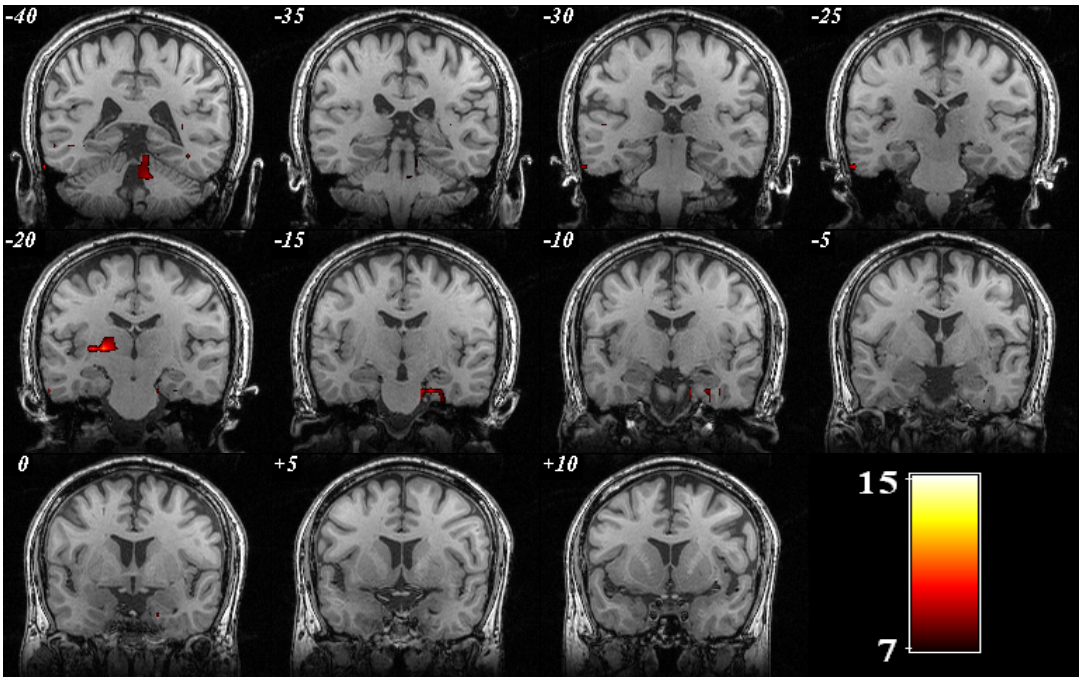

Figure 5.4 Pt3 2dTCA activation t-map (t > 7, cluster size 5) showing a clear left temporal epileptogenic focus and a much smaller right mesial temporal area of activation.

5.1.4 Pt4

Pt4 experienced right side interictal spikes and left and right temporal seizures during EEG monitoring. Both the MRI and PET scan results were normal. The maps indicated that there was spontaneous activity in both mesial temporal lobes (greater on the right) and in the left lateral temporal lobe, which agreed with the EEG monitoring results that revealed seizures originating in both temporal lobes.

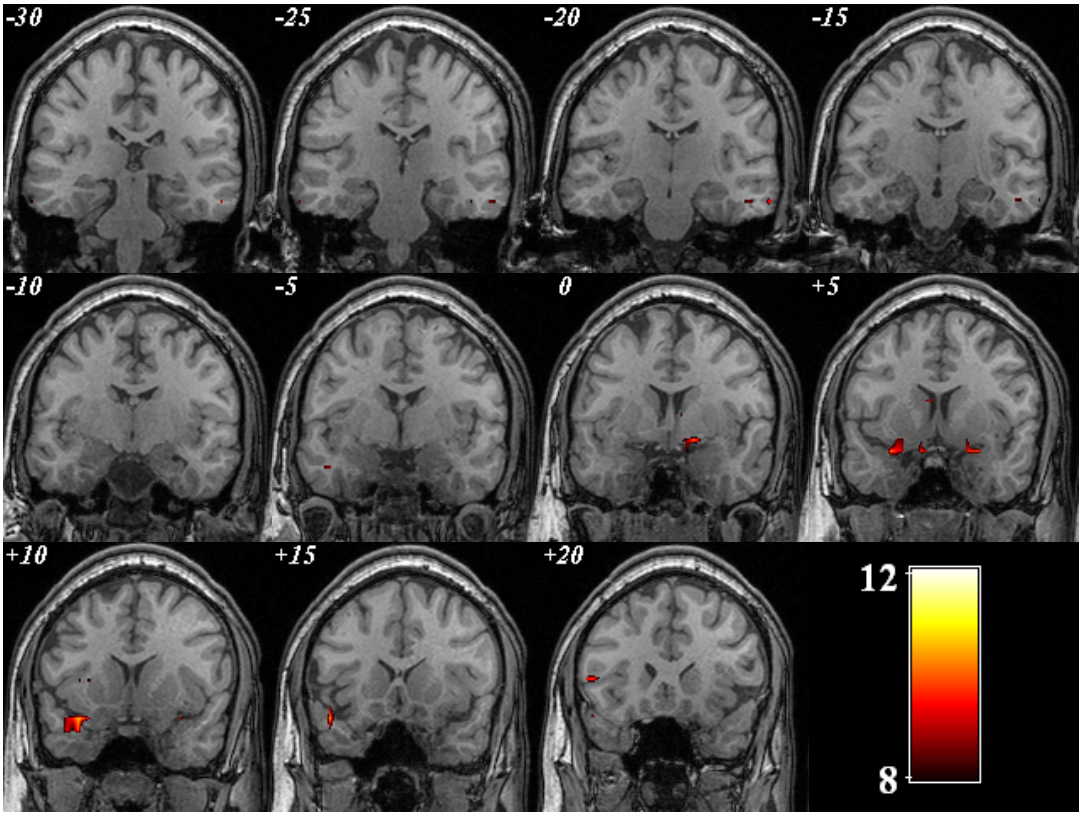

Figure 5.5 Pt4 2dTCA activation t-map (t > 8, cluster size 5) showing left and right mesial temporal activation. The bilateral activations are consistent with the EEG findings.

5.1.5 Pt5

Pt5 experienced left side interictal spikes and left temporal seizures during EEG monitoring. The MRI results revealed bilateral hippocampal volume loss, and the PET scan revealed left TL hypometabolism. The t-maps showed clear left mesial temporal activity as expected from the clinical results.

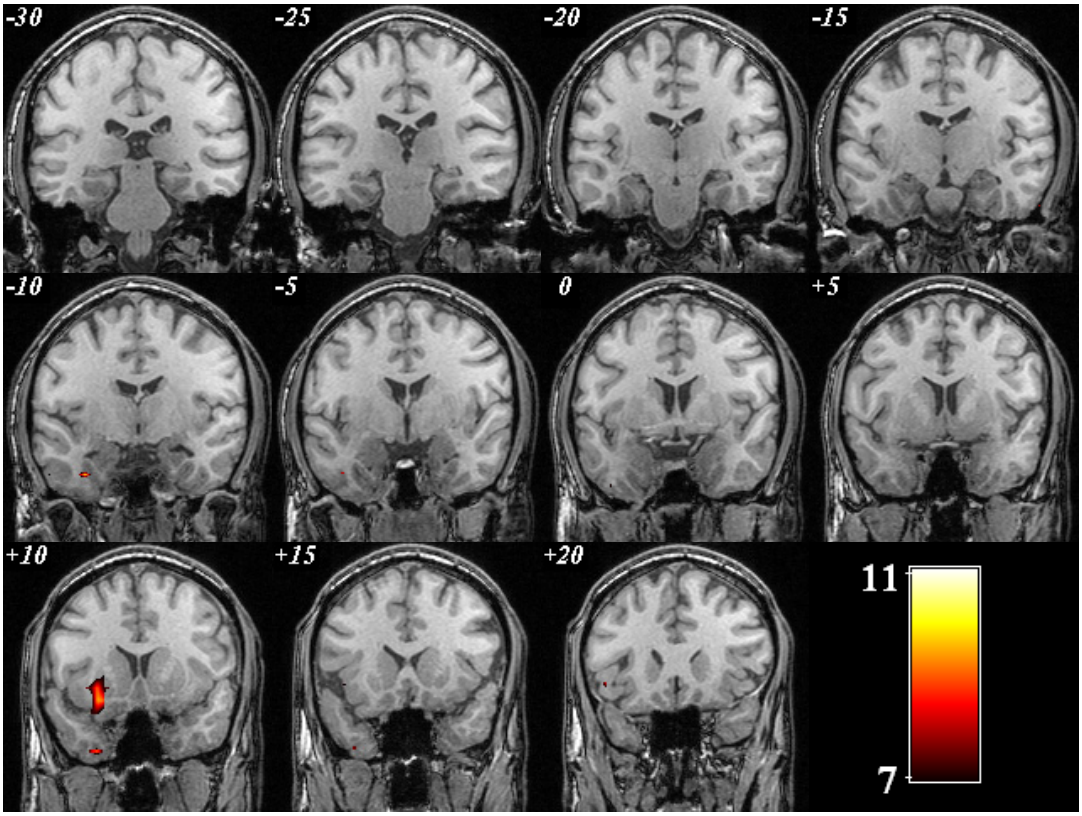

Figure 5.6 Pt5 2dTCA activation t-map (t > 7, cluster size 5) showing left mesial temporal activations consistent with the EEG findings.

5.1.6 Controls

To determine whether or not the lateral and mesial temporal lobe activations seen in most of the epilepsy patients were also present in the resting fMRI of persons without epilepsy, the data from the three healthy controls were also analyzed using the 2dTCA technique. Each of the three controls had some level of TL activation whether it was in the lateral or mesial region as well as some extratemporal activations.

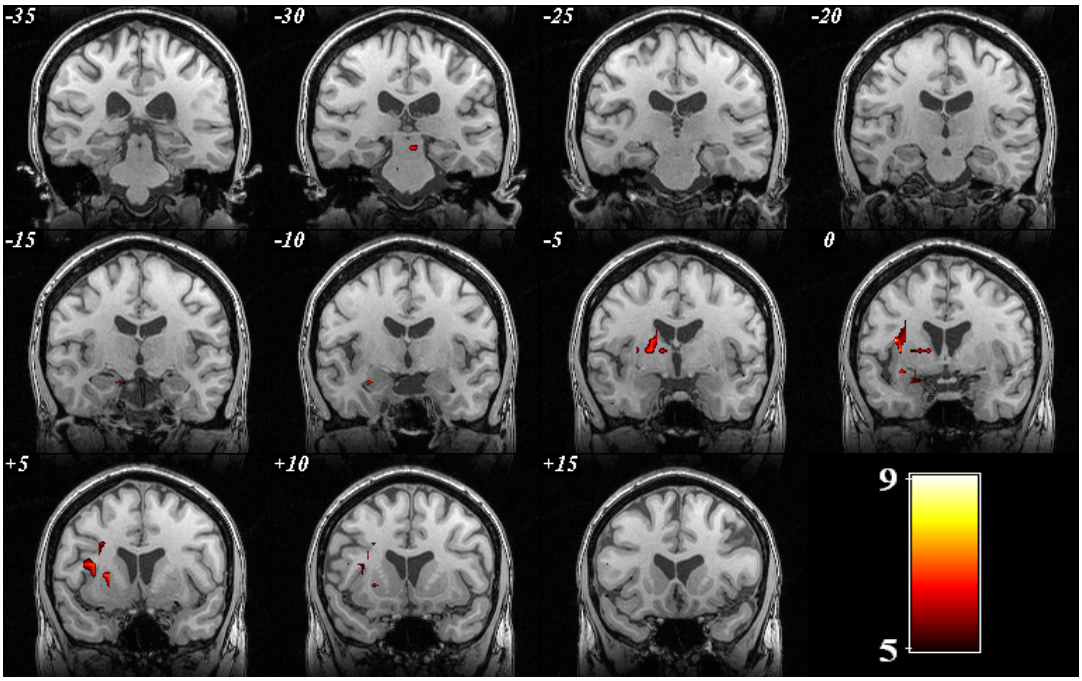

Figure 5.7 Con1 2dTCA activation t-map (t > 5, cluster size 5) showing left lateral temporal activation.

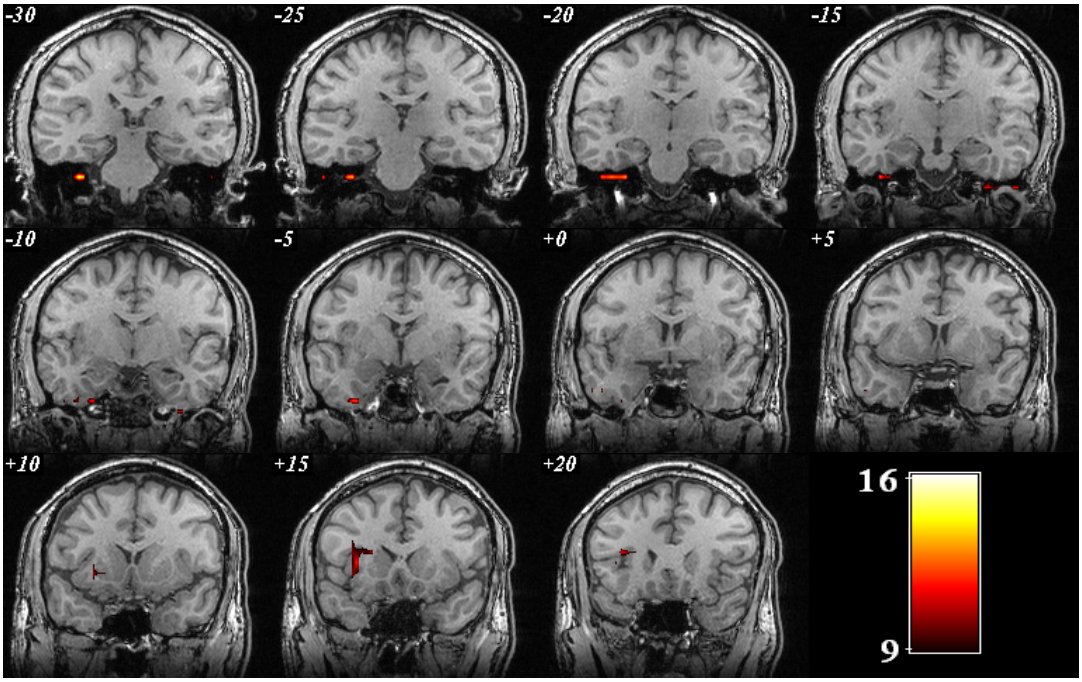

Figure 5.8 Con2 2dTCA activation t-map (t > 9, cluster size 5) showing a small region of left mesial temporal activation.

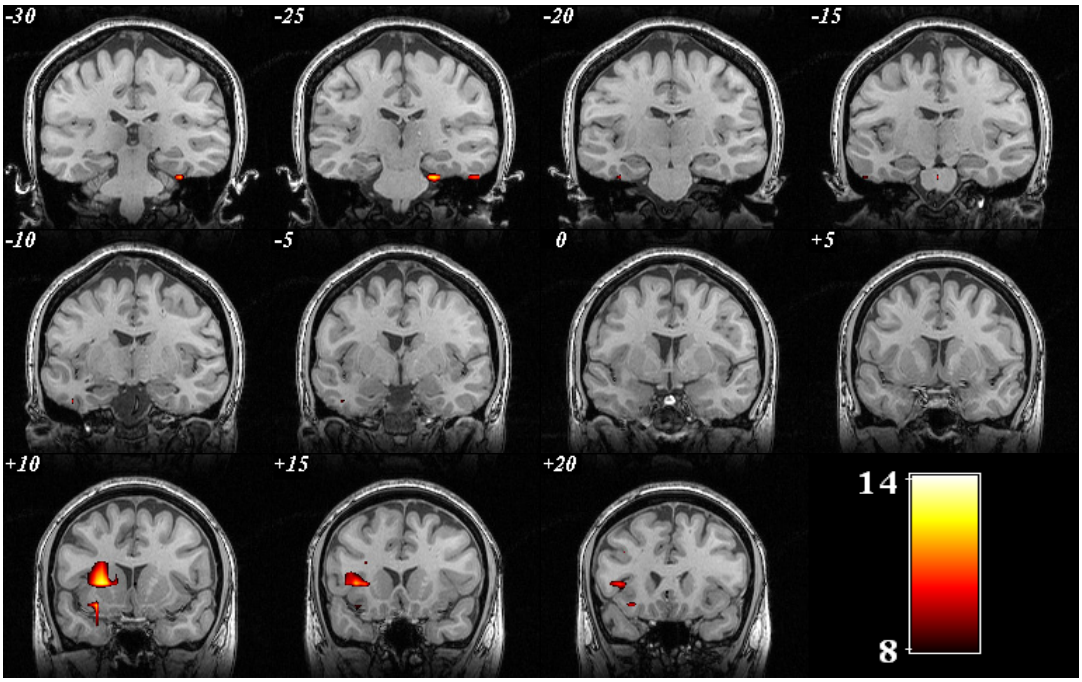

Figure 5.9 Con3 2dTCA activation t-map (t > 8, cluster size 5) showing left and right temporal activations.

5.1.7 Summary

Four of the five TLE patients demonstrated activations within the suspected seizure onset zone when analyzing the fMRI data using the 2dTCA algorithm. Extratemporal activity and activations contralateral to the EEG focus were also found in most. Only Pt2 exhibited activation exclusively contralateral to the clinically defined epileptic focus. All three of the control subjects exhibited some temporal lobe activations but the meaning of these activations is difficult to define without simultaneous EEG data.

While some questions about the source of the activations in these maps remain, the results demonstrate the potential usefulness of the 2dTCA algorithm in helping to define the epileptic foci for temporal lobe epilepsy patients. One drawback is the large number of maps sometimes generated by the algorithm. Each map must be carefully

analyzed to eliminate those due to sources of no clinical interest, such as noise, subject motion, and activations due to changes in attention during scanning. While these maps do not perfectly define the epileptic focus they may provide information about brain regions outside of the scalp EEG defined focus that should be investigated further.

5.2 Feature Evaluation

The feature evaluation process outlined in Section 4.3 was repeated for the in vivo data. Using the clinical information provided along with the functional data, the mesial temporal lobe voxels were divided into epileptic and non-epileptic classes. All voxels in the affected MTL were assumed to be abnormal and all voxels in the "normal" lobe were assumed to be healthy. Random training and testing sets were created for each subject and analyzed to determine the effectiveness of using feature-based methods to process the given data. Thirty Monte Carlo simulations were run, and the performance was assessed with an ANOVA-2 analysis. The subject and the feature selection method again were the factors of comparison. Box plots of the sensitivity and specificity results are given in Figures 5.10 and 5.11.

Instead of achieving median sensitivities and specificities of 90% and higher for all subjects, as was the case for the phantom data, the performance of the in vivo analysis was significantly reduced. No feature set regardless of selection method achieved sensitivity or specificity greater than 90%, and for Pt2 when using SFFS for selection, the median specificity was in the low 40^{th} percentile. Another noteworthy difference between these results and the phantom data analysis results was in the impact of the choice of feature selection method. As seen in Section 4.3, the various methods often had

similar performance, but for the five TLE patient datasets, the GP feature outperformed the others, in terms of sensitivity and specificity, in most cases. While the differences were not always statistically significant, the superior performance for separating the left and right MTLs was evident.

In addition to analyzing features extracted from the five TLE patient datasets, the images from the three healthy controls were also examined. The purpose of these experiments was to demonstrate whether or not the differences seen between the feature values in the healthy and abnormal lobes of the TLE patients were also present in control subjects. All voxels for these subjects belong to the healthy class, but voxels from one lobe were assumed to be abnormal class so that the same tests that were performed on the phantom data would be applicable. The performance metrics for the control data were similar in range to those obtained for the TLE patients. This was likely due to intrinsic differences between the two brain regions, such as mean CBF, that are present in both healthy and unhealthy subjects and can be characterized by one or more the extracted features. However, one key difference between the analyses of the control subjects and the patients was in the performance of the GP feature. For the control data, other features (such as the SFFS generated feature set for instance) outperformed the GP features in terms of sensitivity and specificity in most cases. This could be due to the GP features ability to identify differences between the two MTLs that are not intrinsic to all subjects but are specific to persons with interictal epileptic activity present in their voxel time courses.

Clearly the in vivo feature analysis results are not as impressive as the phantom results. Both the sensitivity and specificity have decreased substantially for these

datasets. While the exact causes of the performance degradation are unknown, they could be due to several factors, including: the greater complexity of the dynamics of the in vivo over the phantom data, a lack of significant interictal activity during scanning, and the misclassification of individual voxels based on clinical information. This analysis assumes that all voxels in the suspected dysfunctional lobe are "bad," and all voxels in the supposedly normal lobe are "good." This is not likely to be completely true, so evaluating the classification performance based on these assumptions is somewhat flawed but still informative.

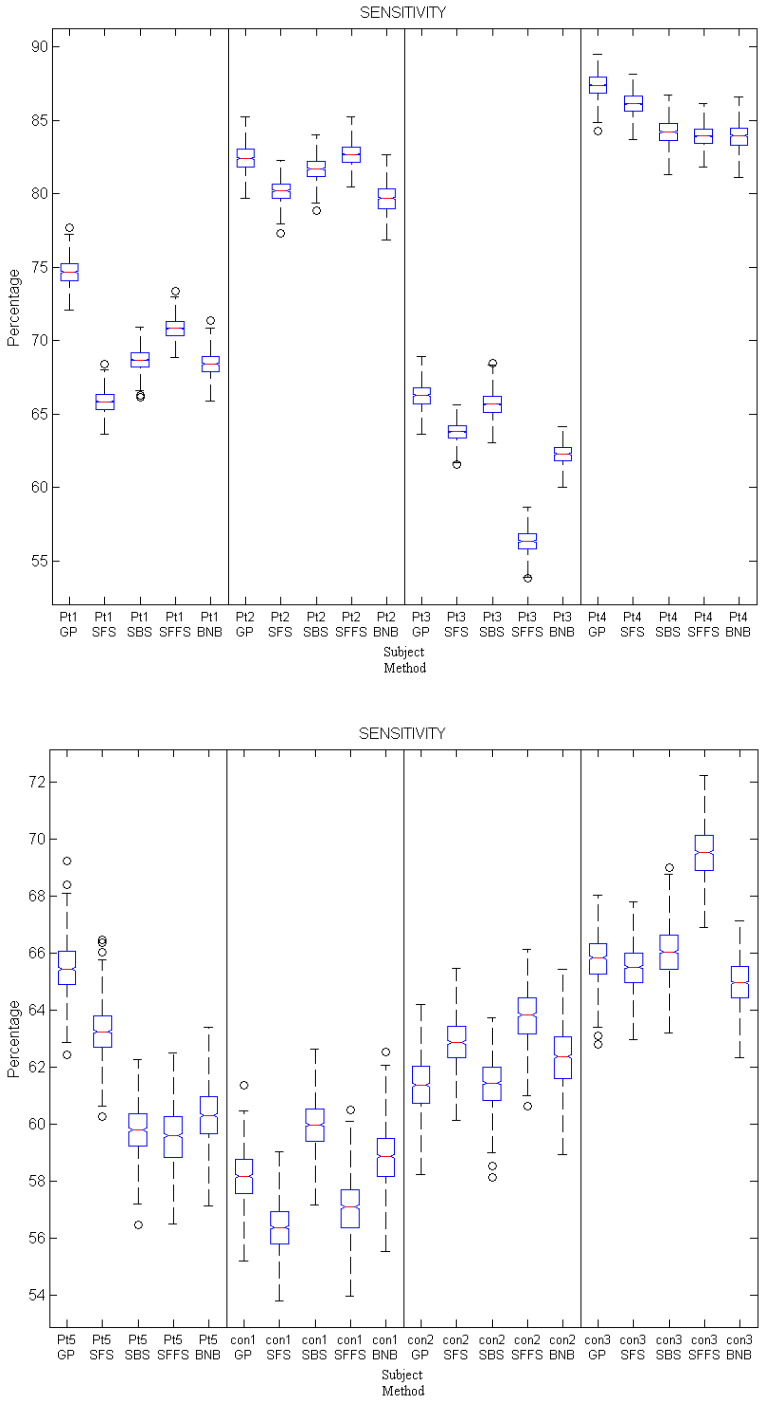

Figure 5.10 This figure illustrates the results of analyzing the performance of feature-based classification of the in vivo data voxels in terms of sensitivity.

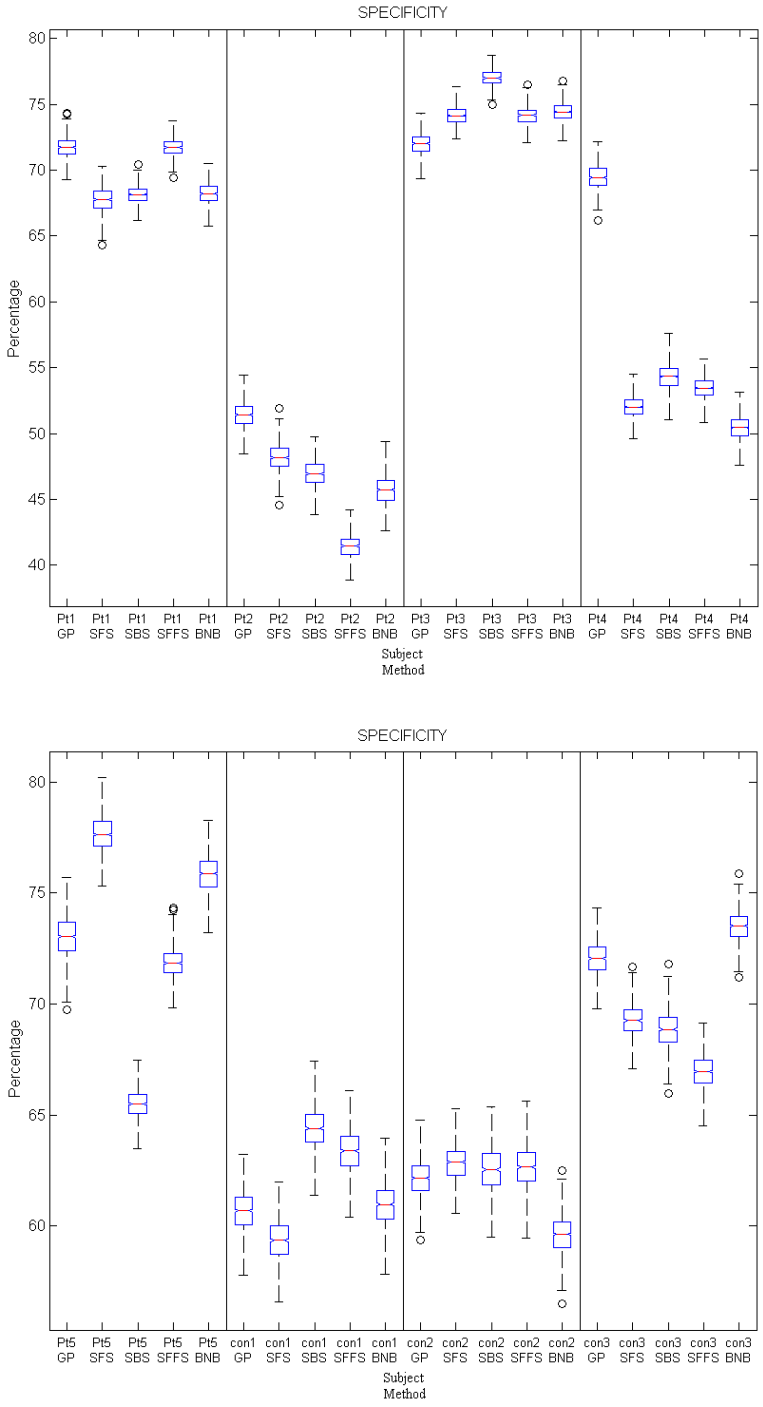

Figure 5.11 This figure illustrates the results of analyzing the performance of feature-based classification of the in vivo data voxels in terms of specificity.

5.3 Feature Clustering

The spectral clustering analysis performed on the phantom data was repeated for the in vivo data. Subsets of the abnormal hippocampal voxels were used to represent the epileptic class, and voxels from the supposedly healthy hippocampus were included in the samples of the non-epileptic class. As stated before, the true class labels of these points are unknown, so the results must be analyzed with care. By limiting the number of improperly labeled voxels in the training set, the weight of the results could be increased in the future. To compensate in part for this problem, the clustering analysis was limited to the mesial temporal lobe voxels. With a better training set, the analysis could be extended to other brain regions.

Based on features created using GP, maps identifying the suspected epileptic voxels in the MTLs were generated for each of the epilepsy patients. The three controls were also analyzed to group voxels with similar temporal characteristics and to determine whether or not the clusters seen in these data were noticeably different from those seen in the epileptic data. The results are displayed in the following sections.

5.3.1 Pt1

The map below shows bilateral MTL activations for this patient with suspected left side onset. These results differed considerably from the unilateral activation seen in the 2dTCA map (Figure 5.2). However, the low accuracy with which the voxels were classified based on the features alone explains these results.

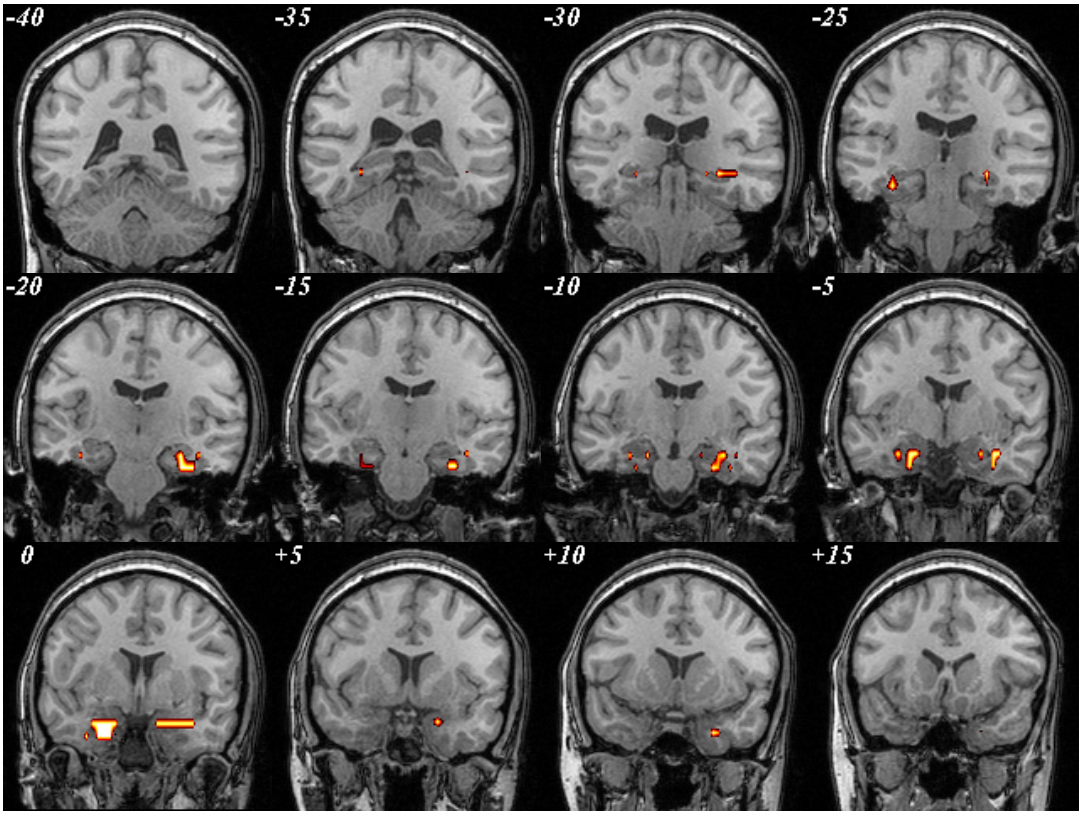

Figure 5.12 Pt1 activation map generated using spectral clustering.

5.3.2 Pt2

This map of Pt2, who has a suspected right side epileptic onset, also demonstrated bilateral activations but with right side dominance. The 2dTCA generated map (Figure 5.3), on the other hand, showed only slight left temporal activation, which conflicts with the clinically defined epileptic focus.

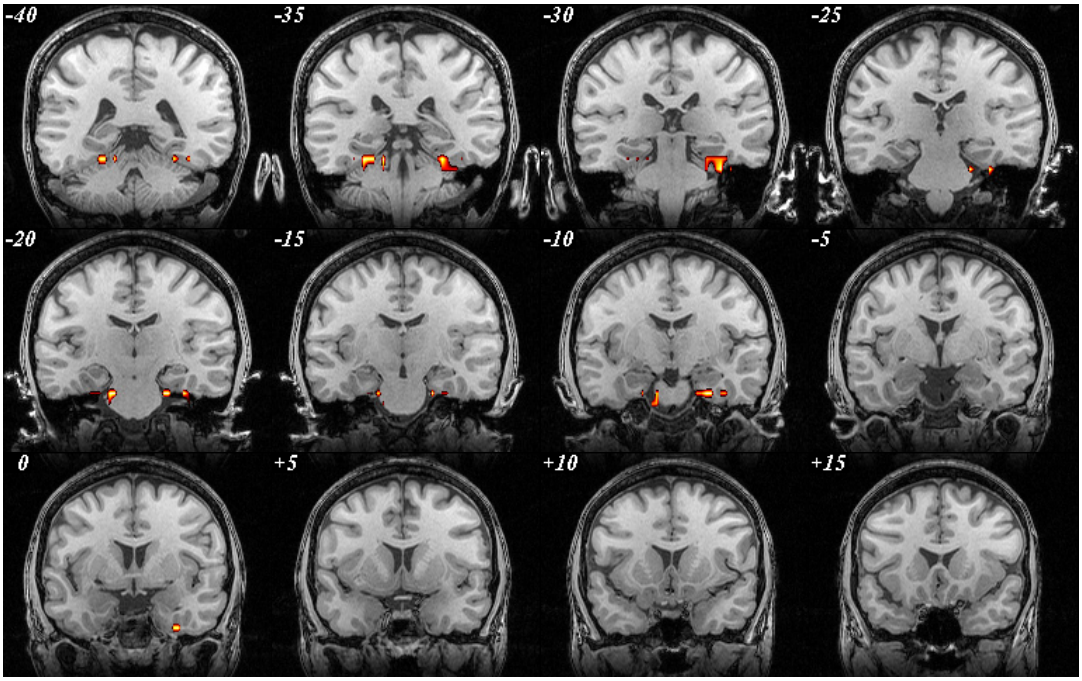

Figure 5.13 Pt2 activation map generated using spectral clustering.

5.3.3 Pt3

This patient is suspected to have left side seizure onset. The map shows greater left side activation than right, as does the 2dTCA map (Figure 5.4).

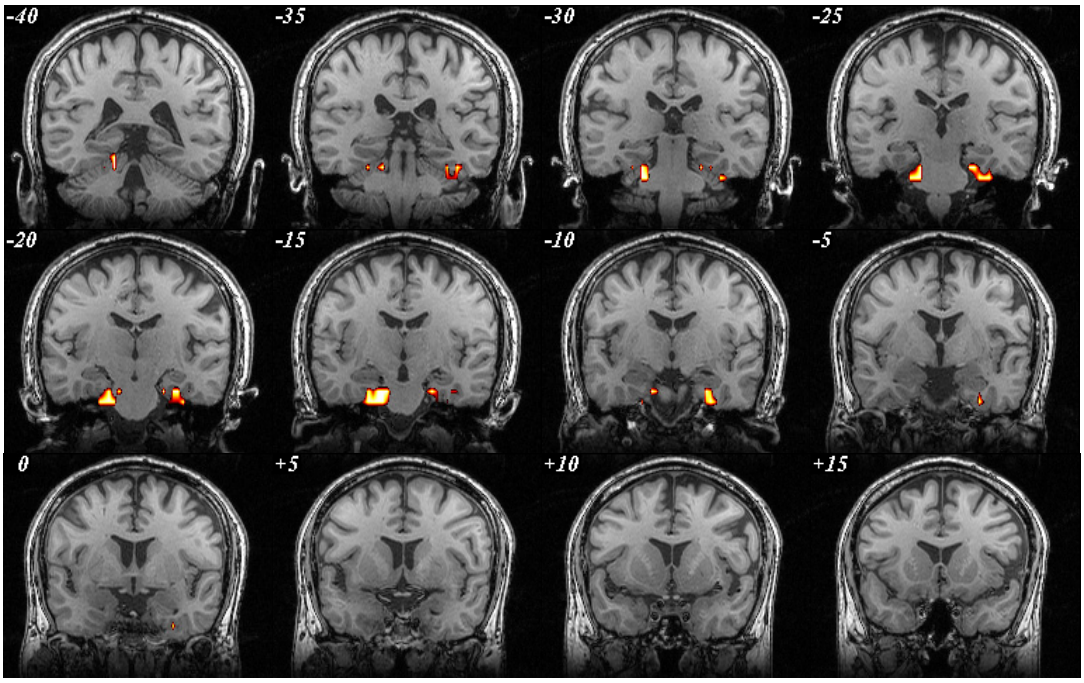

Figure 5.14 Pt3 activation map generated using spectral clustering.

5.3.4 Pt4

This map demonstrates small areas of activation in both MTLs with slightly greater activity in the left lobe, which is not thought to be generating the seizures. These results though are consistent with the 2dTCA map (Figure 5.5) and the EEG findings of bilateral seizures.

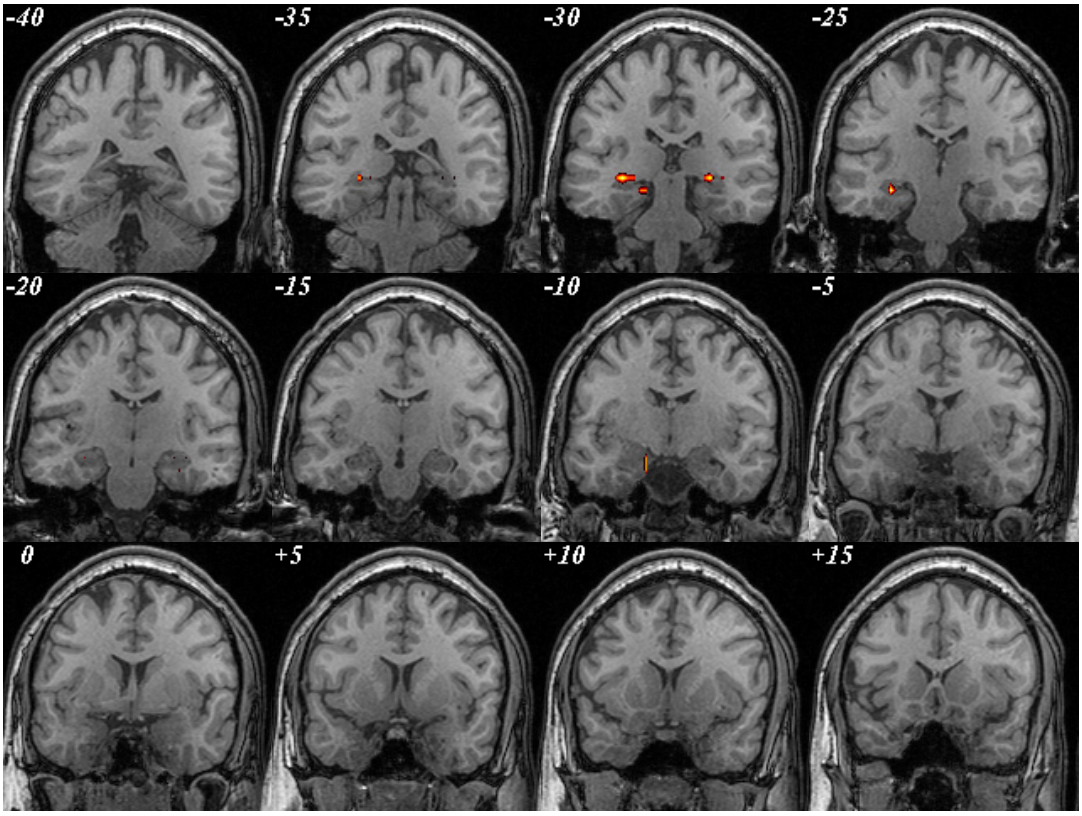

Figure 5.15 Pt4 activation map generated using spectral clustering.

5.3.5 Pt5

This map of Pt5 whose EEG recordings showed left side seizure onset shows activations predominantly in the left MTL as does the 2dTCA map (Figure 5.6).

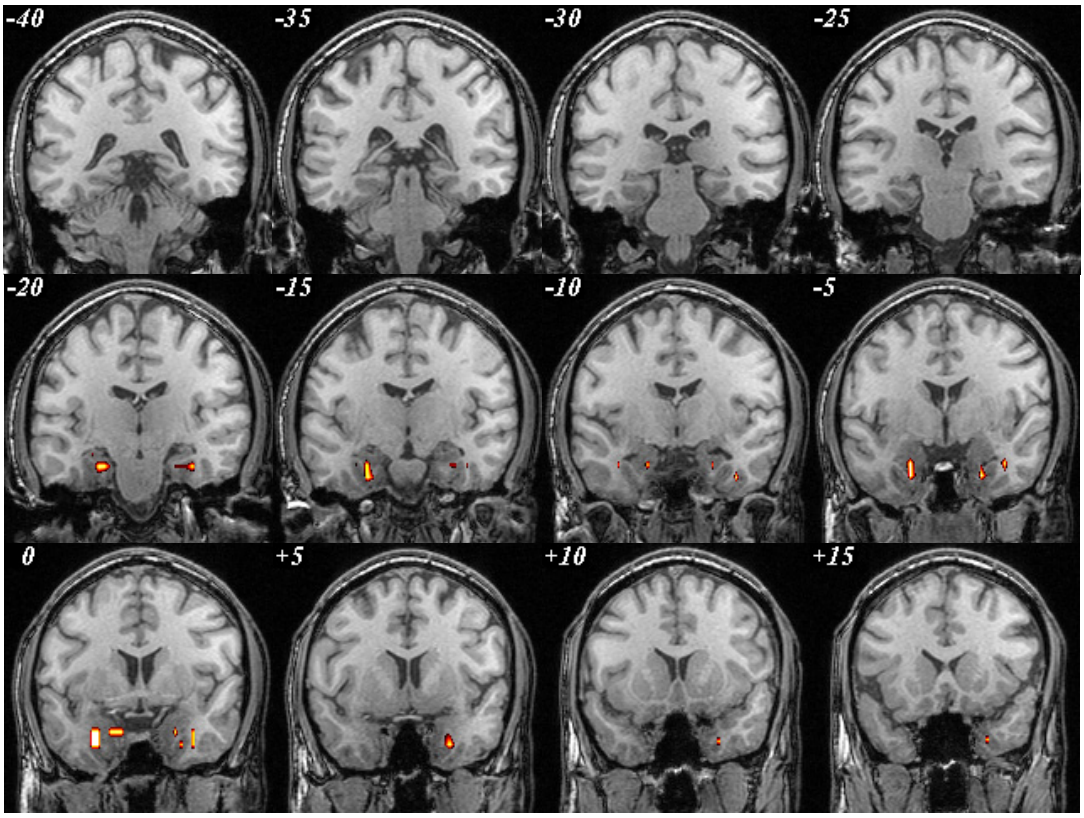

Figure 5.16 Pt5 activation map generated using spectral clustering.

5.3.6 Controls

The activation maps generated for the three controls all demonstrate bilateral activations with no clearly dominant side. These differed from the maps generated for the epilepsy patients which had a dominantly activated side in most cases.

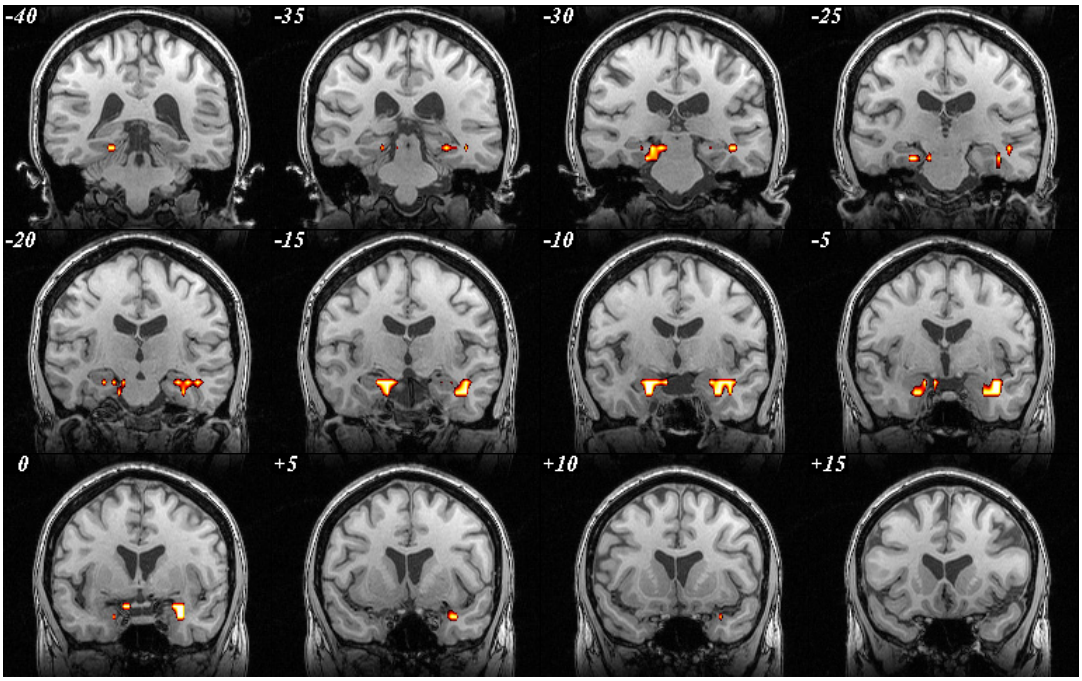

Figure 5.17 Con1 activation map generated using spectral clustering.

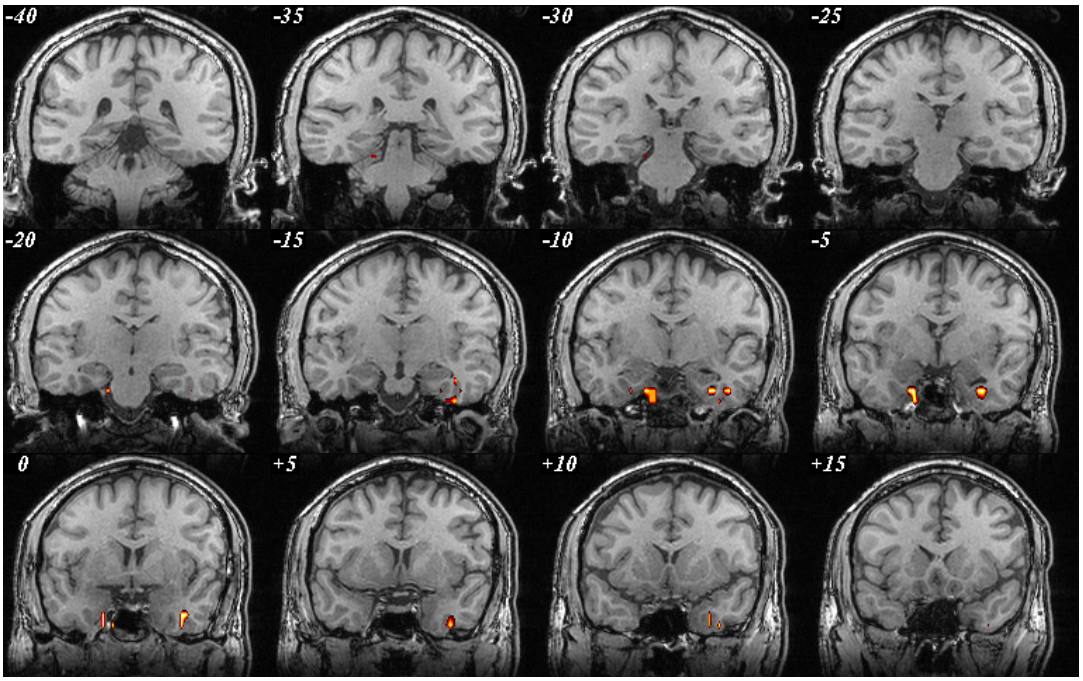

Figure 5.18 Con 2 activation map generated using spectral clustering.

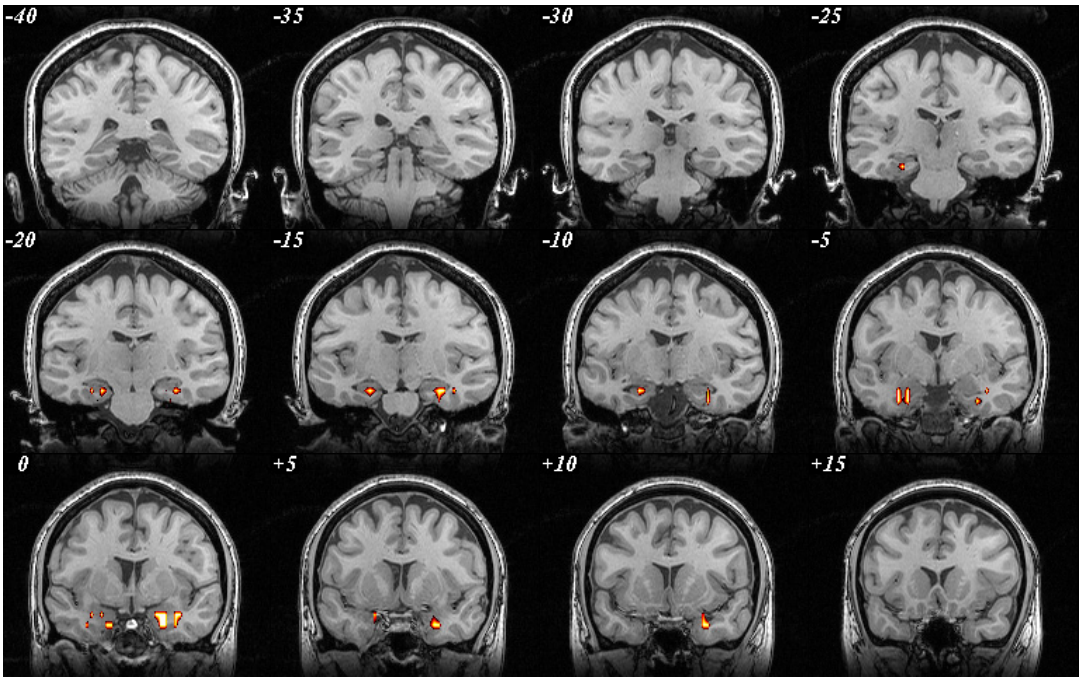

Figure 5.19 Con3 activation map generated using spectral clustering.

5.3.7 Summary

Four of the five TLE patients demonstrated activations within the suspected seizure onset zone when analyzing the fMRI data using spectral clustering based on feature values. In these four cases, the lateralization and dominance of the activations were the same as for the 2dTCA generated maps, although the maps resulting from the two techniques were not identical. Only Pt1 exhibited activations exclusively contralateral to the EEG defined epileptic focus. All three of the control subjects exhibited bilateral temporal lobe activations, but none exhibited dominant activations in one lobe as was the case for all of the TLE patients demonstrating bilateral activations.

5.4 Conclusions

Due to limits in the amount and nature of the data available for this research, the efficacy of applying the feature based analysis and clustering techniques presented in this work cannot be concluded definitively. However, this work demonstrates the potential of these techniques to group voxels with similar interictal dynamics. The results presented here show that the performance of feature based clustering is similar to that obtained using 2dTCA when analyzing in vivo patient data.

CHAPTER 6

CONCLUSIONS AND FUTURE RESEARCH

6.1 Conclusions

This work demonstrates the potential to map epileptic networks through the analysis of features of fMRI voxel time courses. Data from five epilepsy patients and three healthy controls were explored in addition to phantom data with known areas of activation. Analysis of the phantom data was key in validating the technique. Because the exact locations of the simulated activations were known, the results of examining the phantom data could be assessed quantitatively through various performance metrics. The results from the in vivo patient data, on the other hand, had to be analyzed qualitatively.

The phantom data analysis showed that feature-based techniques can be used to distinguish between fMRI voxels with and without simulated activity. Based on features and feature sets created using genetic programming and various feature selection methods, the voxels were classified with over 90% sensitivity and specificity, even in cases with low SNR for which the 2dTCA technique failed to accurately map the activity.

Analysis of the in vivo patient data revealed the potential to discover regions with similar interictal behavior with only gross knowledge of the areas of epileptic activity. First, a classifier was trained on data from the suspected epileptic hippocampus and the presumed healthy hippocampus to find features for discriminating between the two classes. These features were then used to classify the remaining MTL voxels. These experiments revealed that one cannot assume that all voxels in the dysfunctional lobe are also dysfunctional and that all voxels in the healthy lobe are "normal," as suspected. To

address this issue a spectral clustering technique was applied to group the voxels with similar feature characteristics and potentially provide a better picture of the true epileptic network. The results of this analysis revealed that the abnormal activity was usually present in both lobes of the TLE patients, but this abnormal activity was typically dominant in one lobe. The dominant lobe in most cases was the EEG defined epileptic lobe. Clustering of the MTL voxels for the healthy controls also illuminated bilateral activations but without clear dominance in one lobe or the other. This difference in the composition of the clusters found when analyzing healthy versus epileptic subject data may be due to key differences in the dynamics of the functional activity. Further study of this phenomenon could reveal the nature of these differences.

6.2 Future Research

Although this work emphasizes the role of feature processing in the study of fMRI data from epilepsy patients, these techniques are not limited to study of functional activations due to interictal epileptiform activity. The same techniques could be applied to task related studies of cognition and sensorimotor activity and the study of other neurological disorders such as Parkinson's and Alzheimer's disease.

The application of the techniques presented here to simultaneously recorded EEG and fMRI data would further strengthen the results. With such a dataset available, the EEG correlates of changes in the fMRI time courses could be studied and provide a better understanding of the coupling between the two neuroimaging methodologies. The EEG data could be used to better define areas of the brain to focus on when initially defining the gross epileptic onset zone. Then after applying the feature analysis and clustering

techniques, the simultaneous EEG data could be used to verify that the resultant map does indeed include areas demonstrating some amount of abnormal activity during scanning or show that fMRI has the ability to localize interictal activity not evident on EEG. Additionally, the analysis of coupled intracranial EEG data would help to verify the correctness of the maps generated. Intracranial EEG has higher spatial resolution than scalp EEG and would be useful in validating the process. Also, by performing feature analysis on smaller windows of data instead of the entire time course, the signal dynamics could be explored in the feature space and reveal more about the hemodynamic response due to interictal activity visible in EEG recordings.

Another possible extension of this work would be to study multiple fMRI datasets collected from the same patient at different times, i.e., days, weeks, or months apart. By training and testing on data collected in one session, it is possible that the classifier is being overtrained and tuned to just one set. By examining multiple sets from the same patient we can explore this issue and determine the robustness of the patient specific features over time. Would the features chosen for the first dataset result in similar maps for subsequent datasets, or would new features need to be chosen each time to produce accurate maps? The work could also be extended by performing statistical analysis on the features themselves, not the voxel time courses, to create feature based SPMs.

For this work, only five datasets from patients with suspected unilateral TLE were available. With such a small dataset, it is impossible to draw any conclusions about the utility of the techniques. Although the results demonstrate the promise of the presented methodology, a larger corpus of data would be needed to prove the clinical usefulness of the procedures. Additionally, studying patients who subsequently underwent epilepsy

surgery and correlating fMRI localization results with the resected brain regions and the ultimate seizure frequency outcome following surgery would prove the precision of the localizations.

Finally, improving the model of simulated data so that it more closely resembles real fMRI data would also help with future developments of the analysis framework and rendering the technique more robust. For instance, several distinct HRFs could be incorporated into the data to mirror the spatial variations seen in the hemodynamic responses of different brain regions. In this way, activity due to multiple sources could be studied and more complex relationships—not just a simple two class problem such as epileptic or non-epileptic —could be explored.

APPENDIX A

STATISTICAL PARAMETRIC MAPPING

Statistical parametric mapping (SPM) is a voxel-based technique for examining regional differences in brain activity recorded during functional neuroimaging scans. In activation studies, the objective of the analysis is to map areas of the brain with a specified functional response to experimental conditions. The voxel values in the generated statistical maps are measures of the extent to which the predicted response accounts for the variance in the observed voxel time courses. Through application of the general linear model and Gaussian random field theory, statistical inferences about the significance of the effects of the experimental design can be made at each voxel [5].

The general linear model (GLM) is an important statistical analysis tool that forms the foundation of many widely used statistical tests. Analysis of variance (ANOVA), t-tests, regression analysis, correlation coefficients, and factor analysis, among other parametric statistical methods, are special cases of this model. The goal of using the GLM is to represent a set of measured observations as a linear combination of response variables describing the conditions under which the observations were made. The GLM can be expressed in matrix form as follows:

$$\mathbf{X} = \mathbf{G}\boldsymbol{\beta} + \mathbf{e} \tag{A.1}$$

where $\mathbf{X}$ is the measured data, $\mathbf{G}$ is the design matrix, $\boldsymbol{\beta}$ is the matrix of model parameters to be estimated, and $\mathbf{e}$ is the matrix of normally distributed errors between the observations and the model. In the case of fMRI analysis, $\mathbf{X}$ contains one column for each voxel and one row for each scan. $\mathbf{G}$ has one row per scan and one column for each

modeled effect, and $\boldsymbol{\beta}$ has one row per effect and one column per voxel. If $\mathbf{G}$ is full rank, least squares estimates of $\boldsymbol{\beta}$ are given by

$$\mathbf{b} = \left(\mathbf{G}^T\mathbf{G}\right)^{-1}\mathbf{G}^T\mathbf{X} \tag{A.2}$$

A wide range of statistical tests can be implemented using Equations A.1 and A.2. Two commonly reported statistics in imaging analysis are t and F statistics. These statistics, which are calculated as outlined in [5], are used to test the null hypothesis that the effects of interest (e.g., the expected hemodynamic response or the presence or absence of pharmacological treatments during scanning) included in $\mathbf{G}$ are not significant. Employment of F statistics allows for the significance of all of the effects of interest to be examined, while analysis of t statistics enables inferences about the effects of specific conditions and variables to be made.

The simple example shown in Figure A.1 illustrates the application of the GLM to a single observed signal with one regressor, i.e., effect of interest. In this case, the fMRI time course is modeled as the sum of the predicted hemodynamic response to a set of stimuli and residual error. The value of $\boldsymbol{\beta_1}$ that provides the best fit to the data is estimated using equation A.2 and can be used to perform a series of t-tests that will provide measures of the goodness of the fit between the modeled response and the real data. The resulting statistical map of t values, known as an SPM{t}, has higher intensities for voxels with time courses most similar to the model. Improvements to this model could be made by adding confounding factors (e.g., movement parameters or the global signal mean) to the design matrix. Including confounds, which can inhibit the estimation of interesting effects, allows for adjustment of the data to discount the effects of these irrelevant factors. For example, by incorporating the motion parameter time

series into the model, signal variance explained by these artifacts can be removed from the voxel time courses, and consequently, these confounding factors will not negatively impact attempts to model the data through the effects of interest.

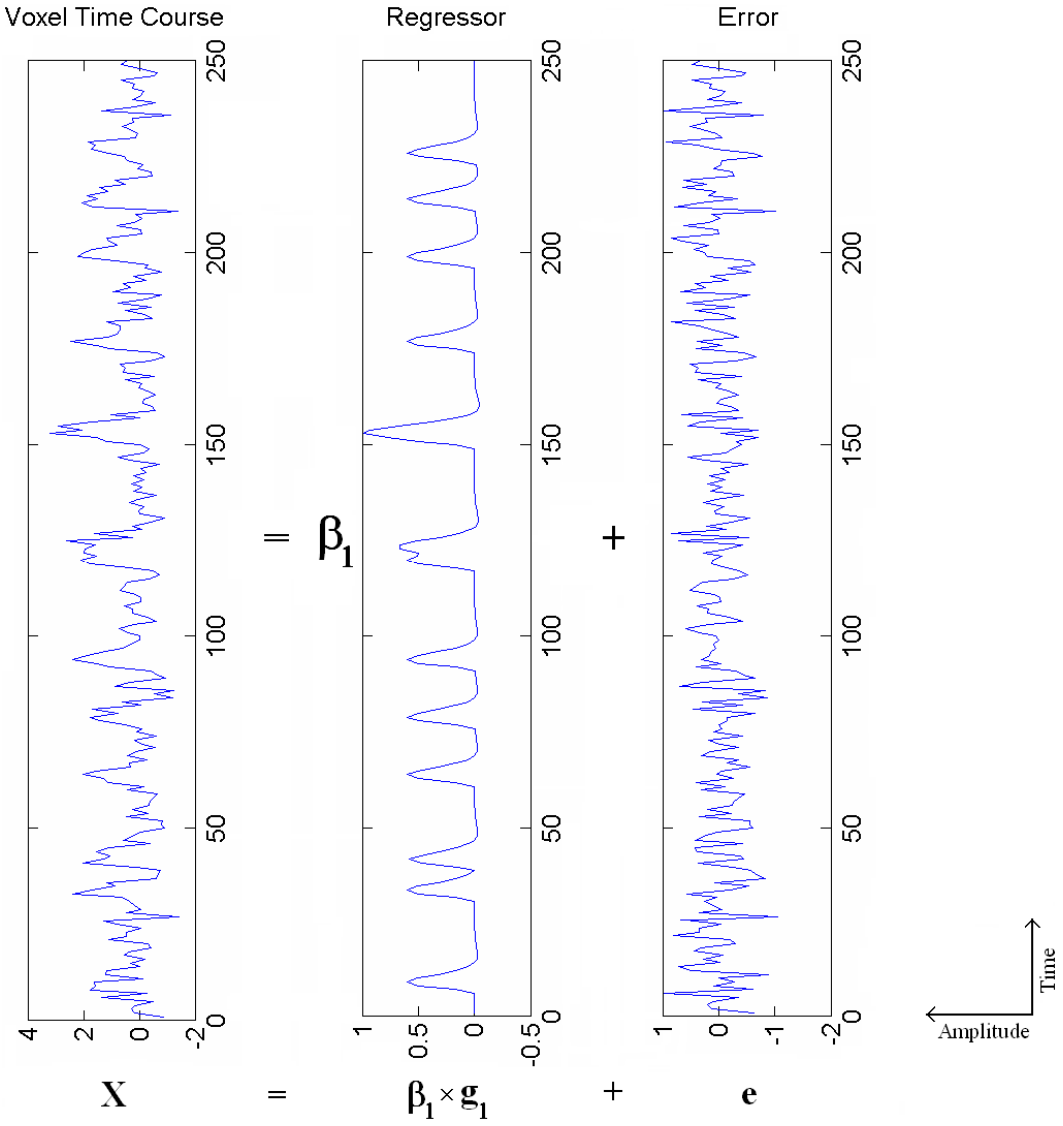

Figure A.1 An example illustrating the use of GLM in the analysis of fMRI data. The voxel time course (**X**) is modeled as the weighted sum of the predicted hemodynamic response ($\mathbf{g_1}$) and residual Gaussian distributed error (**e**).

After the statistical maps are created, inferences must be made about which voxel values represent significant activations (or deactivations). Thresholding the maps at a given height (intensity) provides a certain level of confidence in the presence of activations and reduces the odds of spurious activations due to chance. The appropriate threshold for the desired level of confidence (e.g., $p < 0.05$) can be determined for the SPM{t} or SPM{F} in a naïve fashion by using a table of t or F statistics, respectively. The degrees of freedom of the map and the p-value dictate the threshold needed for the chosen error rate. The null hypothesis of no activation can then be rejected for all voxels exceeding this threshold. The problem with applying this simple approach when examining fMRI is that calculation of the statistics involves a mass univariate analysis and leads to the multiple testing or multiple comparisons problem [115]. Because of the large number of non-independent statistical tests (comparisons) being evaluated simultaneously when analyzing functional images, the likelihood of chance excursions in the statistical map becomes quite high. Adjustments must therefore be made to control for these Type I errors, i.e., false positives.

As the number of tests increases so does the probability that at least one Type I error will occur over the entire set (family) of individual statistical tests. This overall error rate is known as the familywise error (FWE) rate. According to the Bonferroni inequality, the relationship between the FWE rate α_{FWE} and the individual testing error rate $\alpha_{individual}$ for a family of dependent statistical tests is given by $\alpha_{FWE} \leq k \times \alpha_{individual}$, where k is the total number of tests or comparisons. For an image with 20,000 brain voxels, $\alpha_{individual}$ must be set to 2.5×10^{-6} or less to achieve a maximum FWE rate of 0.05. Such a low p-value is too stringent to be practical.

SPM programs often employ Gaussian random field theory to correct for FWE without the need to set an impractical individual error rate [5, 115]. The statistical map is modeled as a stationary Gaussian random field, and inferences about the significance of the regionally specific effects are made based on the corrected p-values estimated using distributional approximations from Gaussian field theory. The necessary threshold is then selected based on this p-value, which represents the Type I error rate for the entire brain, not individual voxels. In addition to considering the intensity of the voxel when inferring significance, cluster size is also generally taken into account. The choice of cluster size will determine whether the cluster-level or the voxel-level statistical significance is greater. Smaller cluster sizes result in fewer tests per cluster, thereby increasing $\alpha_{individual}$ and reducing the individual voxel significance level for a preset corrected p-value. In other words, the likelihood that the cluster contains activated voxels rises, but the probability that individual voxels within the cluster are significant decreases. Larger cluster sizes, on the other hand, lead to reductions in $\alpha_{individual}$ and increased voxel-level significance.

The maps in Figure A.2 show how the activated areas can differ greatly depending on the use of corrected or uncorrected p-values and the choice of cluster size. For an uncorrected p-value of 0.05, the activations are scattered across brain regions as seen in Figure A.2a. When FWE correction is applied, these spurious activations are removed for the same false positive rate, and only a few focal areas of activation remain as shown in Figure A.2b. Changing the minimum cluster size also helps to reduce the presence of scattered, non-focal activations even without the use of error correction techniques, as demonstrated in Figure A.3c by setting a minimum cluster size of 100

voxels. Typically in functional activation studies error correction and minimum cluster sizes are applied when generating activation maps.

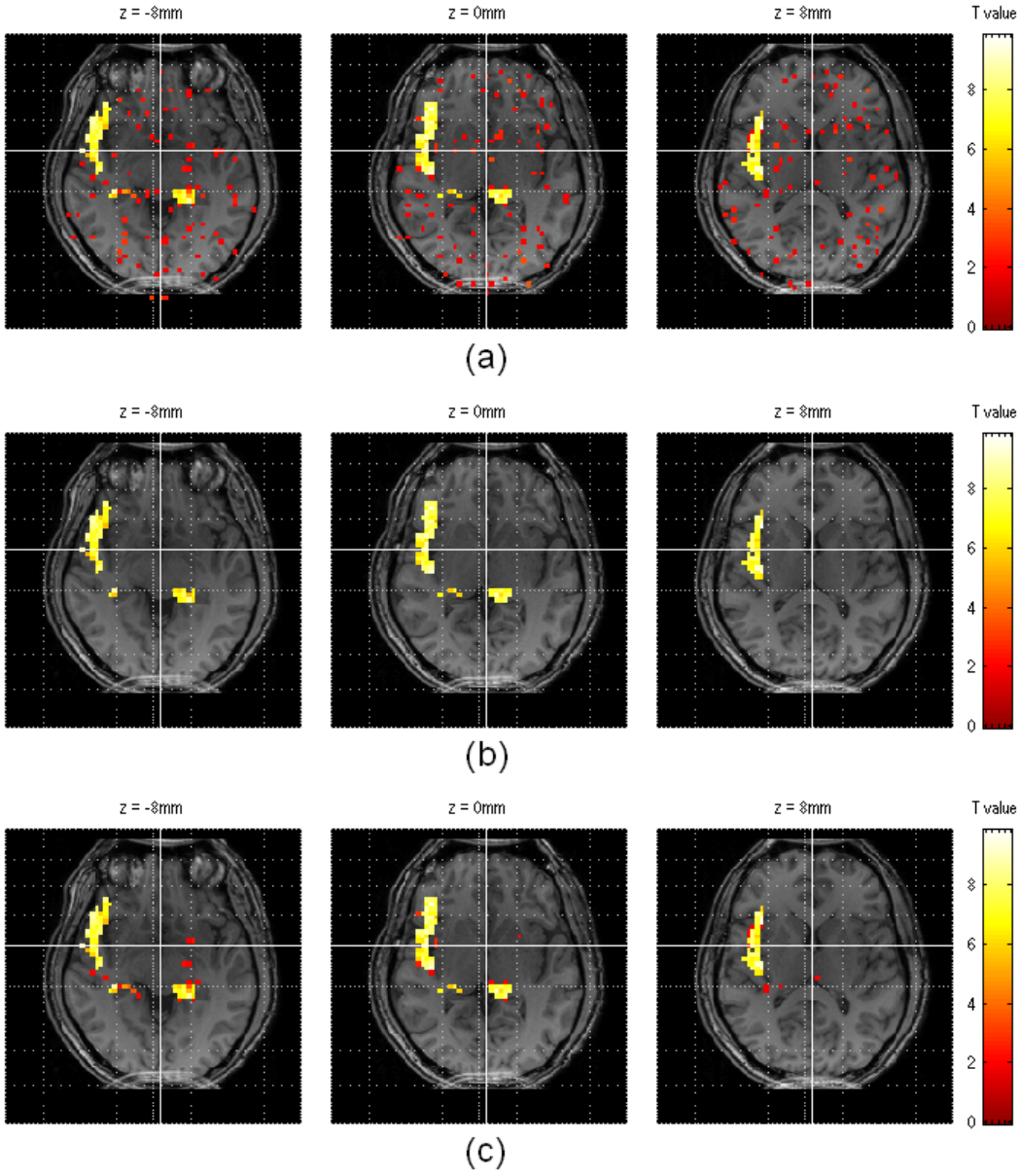

Figure A.2 Axial slices of an anatomical image with the same superimposed SPM{t} thresholded at various heights and cluster sizes. (a) Significant activations found for an uncorrected $p < 0.05$ with minimum cluster size > 0 voxels. (b) Significant activations found for $p < 0.05$ with FWE correction and minimum cluster size > 0 voxels. (c) Significant activations found for an uncorrected $p < 0.05$ and minimum cluster size > 100 voxels.

As mentioned previously, a prediction must be made about what the functional response will be when analyzing the results of functional activation studies using SPM analysis. The expected BOLD or perfusion response can be determined by convolving the reference time course, i.e., a signal representing the timings of stimulus occurrences, with the hemodynamic response function model as demonstrated in Figure A.3. Block designs involve trials of alternating epochs of task and control (rest) conditions in order to evoke sustained functional responses. The resting conditions are designed to induce the same response as the task, except for the evoked response of interest; therefore, any differences in response between the task and rest conditions can be attributed to the effect under investigation. Event-related designs allow one to study the effects of individual, brief stimuli, not prolonged stimuli like in block studies. This type of design is useful for studying spontaneous brain activity like interictal bursts or other pathological events.

Once the predicted response is known, the SPM analysis methods discussed previously can be applied to both types of data. The main difference between the two paradigms is in the importance of the hemodynamic model. Slight changes to the model will have little effect on the block response due to the additive effects of the sustained responses, but if the model is not accurate when performing an event-related analysis, the models of the individual stimuli will greatly differ from the true response. Figure A.3 illustrates how the modeled response to the block design has a square wave-like characteristic, while the event-related response resembles a downsampled version of the HRF model around the times that the events occur.

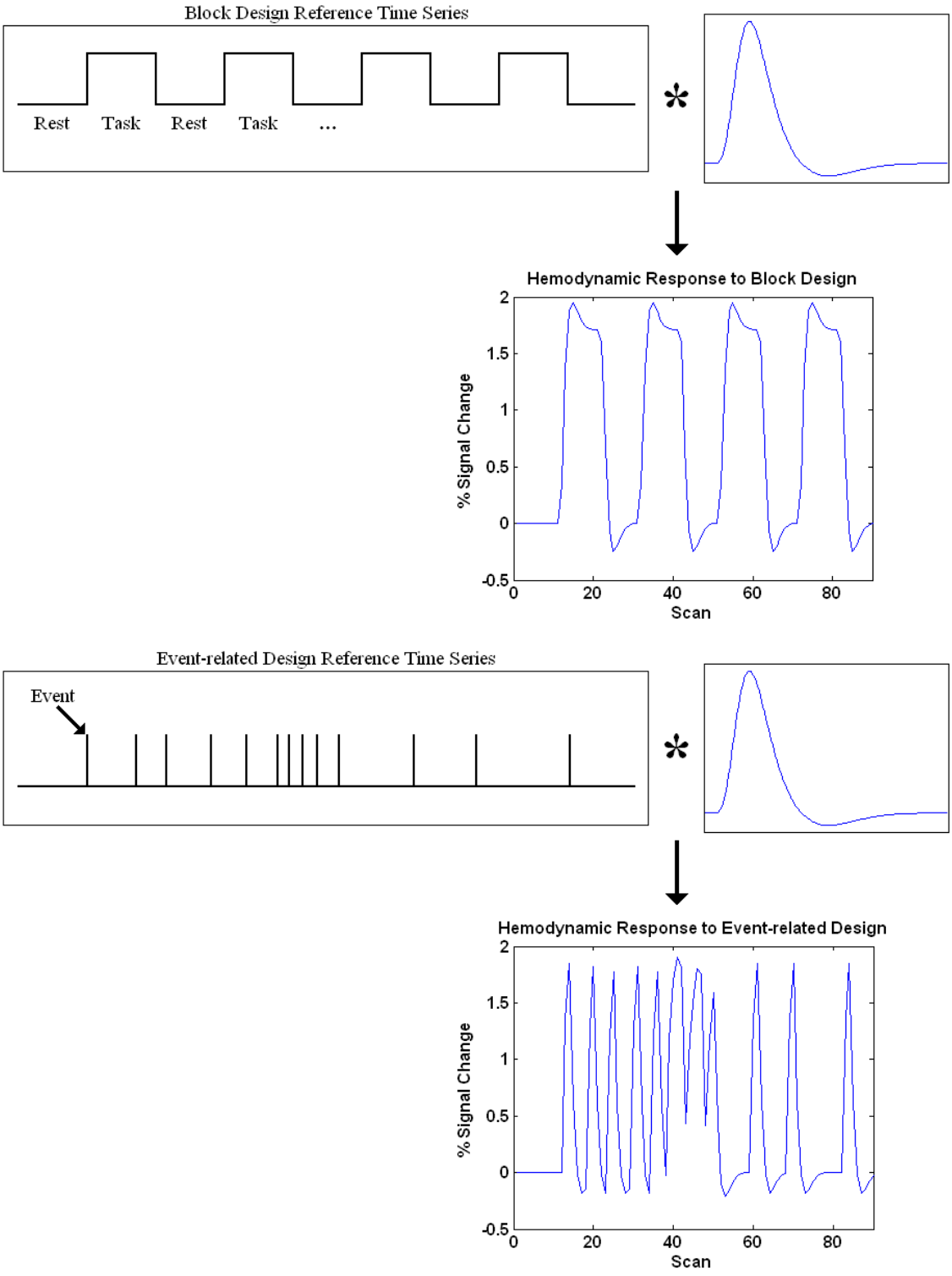

Figure A.3 Illustration of the procedure to estimate the hemodynamic response for both block and event-related studies. The reference time series are convolved with the hemodynamic model to obtain expected response.

REFERENCES

[1] J. F. Wilson, "Searching for Epilepsy Solutions," *Annals of Internal Medicine*, vol. 141, pp. 329-332, 2004.

[2] C. W. Bazil, "Comprehensive Care of the Epilepsy Patient — Control, Comorbidity, and Cost," *Epilepsia*, vol. 45, pp. 3-12, 2004.

[3] J. S. Khoury, R. S. Winokur, J. I. Tracy, and M. R. Sperling, "Predicting seizure frequency after epilepsy surgery," *Epilepsy Research*, vol. 67, pp. 89-99, 2005.

[4] F. Rosenow and H. Luders, "Presurgical evaluation of epilepsy," *Brain*, vol. 124, pp. 1683-1700, 2001.

[5] K. J. Friston, A. P. Holmes, K. J. Worsley, J. P. Poline, C. D. Frith, and R. S. J. Frackowiak, "Statistical parametric maps in functional imaging: A general linear approach," *Human Brain Mapping*, vol. 2, pp. 189-210, 1994.

[6] R. S. J. Frackowiak, K. J. Friston, C. Frith, R. Dolan, C. J. Price, S. Zeki, J. Ashburner, and W. D. Penny, *Human Brain Function*, 2nd ed: Academic Press, 2003.

[7] Epilepsy Foundation of America, "Understanding Epilepsy," 2007.

[8] Commission on Classification and Terminology of the International League Against Epilepsy, "Proposal for revised clinical and electroencephalographic classification of epileptic seizures," *Epilepsia*, vol. 22, pp. 489-501, 1981.

[9] J. M. Freeman, E. P. G. Vining, D. J. Pillas, P. L. Pyzik, J. C. Casey, and M. T. Kelly, "The Efficacy of the Ketogenic Diet—1998: A Prospective Evaluation of Intervention in 150 Children," *Pediatrics*, vol. 102, pp. 1358-1363, 1998.

[10] S. Wiebe, W. T. Blume, J. P. Girvin, and M. Eliasziw., "A randomized, controlled trial of surgery for temporal-lobe epilepsy," *The New England Journal of Medicine*, vol. 345, pp. 311-318, 2001.

[11] National Institute of Neurological Disorders and Stroke, "Curing Epilepsy: The Promise of Research." Bethesda, MD. National Institutes of Health.

[12] R. V. Patwardhan, B. Stong, E. M. Bebin, J. Mathisen, and P. A. Grabb, "Efficacy of Vagal Nerve Stimulation in Children with Medically Refractory Epilepsy," *Neurosurgery*, vol. 47, pp. 1353-1358, 2000.

[13] A. L. Bernstein, H. Barkan, and T. Hess, "Vagus nerve stimulation therapy for pharmacoresistant epilepsy: Effect on health care utilization," *Epilepsy & Behavior*, vol. 10, pp. 134-137, 2007.

[14] C. M. DeGiorgio, A. Shewmon, D. Murray, and T. Whitehurst, "Pilot Study of Trigeminal Nerve Stimulation (TNS) for Epilepsy: A Proof-of-Concept Trial," *Epilepsia*, vol. 47, pp. 1213-1215, 2006.

[15] B. Litt and G. Baltuch, "Brain Stimulation for Epilepsy," *Epilepsy & Behavior*, vol. 2, pp. S61-S67, 2001.

[16] J. F. Kerrigan, B. Litt, R. S. Fisher, S. Cranstoun, J. A. French, D. E. Blum, M. Dichter, A. Shetter, G. Baltuch, J. Jaggi, S. Krone, M. Brodie, M. Rise, and N. Graves, "Electrical Stimulation of the Anterior Nucleus of the Thalamus for the Treatment of Intractable Epilepsy," *Epilepsia*, vol. 45, pp. 346-354, 2004.

[17] I. Osorio, M. G. Frei, S. Sunderam, J. Giftakis, N. C. Bhavaraju, S. F. Schaffner, and S. B. Wilkinson, "Automated seizure abatement in humans using electrical stimulation," *Annals of Neurology*, vol. 57, pp. 258-268, 2005.

[18] K. Vonck, P. Boon, P. Claeys, S. Dedeurwaerdere, R. Achten, and D. Van Roost, "Long-term Deep Brain Stimulation for Refractory Temporal Lobe Epilepsy," *Epilepsia*, vol. 46, pp. 98-99, 2005.

[19] E. H. Bae, L. M. Schrader, K. Machii, M. Alonso-Alonso, J. J. Riviello Jr, A. Pascual-Leone, and A. Rotenberg, "Safety and tolerability of repetitive transcranial magnetic stimulation in patients with epilepsy: a review of the literature," *Epilepsy & Behavior*, vol. 10, pp. 521-528, 2007.

[20] E. Y. Joo, S. J. Han, S.-H. Chung, J.-W. Cho, D. W. Seo, and S. B. Hong, "Antiepileptic effects of low-frequency repetitive transcranial magnetic stimulation by different stimulation durations and locations," *Clinical Neurophysiology*, vol. 118, pp. 702-708, 2007.

[21] X.-F. Yang and S. M. Rothman, "Focal cooling rapidly terminates experimental neocortical seizures," *Annals of Neurology*, vol. 49, pp. 721-726, 2001.

[22] X.-F. Yang, J. H. Chang, and S. M. Rothman, "Long-lasting Anticonvulsant Effect of Focal Cooling on Experimental Neocortical Seizures," *Epilepsia*, vol. 44, pp. 1500-1505, 2003.

[23] S. M. Rothman, M. D. Smyth, X.-F. Yang, and G. P. Peterson, "Focal cooling for epilepsy: An alternative therapy that might actually work," *Epilepsy & Behavior*, vol. 7, pp. 214-221, 2005.

[24] B. E. Swartz and E. S. Goldensohn, "Timeline of the history of EEG and associated fields," *Electroencephalography and Clinical Neurophysiology*, vol. 106, pp. 173-176, 1998.

[25] P. Gloor, "Neuronal generators and the problem of localization in electroencephalography: application of volume conductor theory to

electroencephalography," *Journal of Clinical Neurophysiology*, vol. 2, pp. 327-54, 1985.

[26] B. Litt, R. Esteller, J. Echauz, M. D'Alessandro, R. Shor, T. Henry, P. Pennell, C. Epstein, R. Bakay, M. Dichter, and G. Vachtsevanos, "Epileptic Seizures May Begin Hours in Advance of Clinical Onset: A Report of Five Patients," *Neuron*, vol. 30, pp. 51-64, 2001.

[27] A. Bragin, J. Engel, C. L. Wilson, I. Fried, and G. W. Mathern, "Hippocampal and Entorhinal Cortex High-Frequency Oscillations (100-500 Hz) in Human Epileptic Brain and in Kainic Acid-Treated Rats with Chronic Seizures," *Epilepsia*, vol. 40, pp. 127-137, 1999.

[28] A. Bragin, C. L. Wilson, R. J. Staba, M. Reddick, I. Fried, and J. Engel, Jr., "Interictal high-frequency oscillations (80-500Hz) in the human epileptic brain: Entorhinal cortex," *Annals of Neurology*, vol. 52, pp. 407-415, 2002.

[29] B. Litt and J. Echauz, "Prediction of Epileptic Seizures," *The Lancet Neurology*, vol. 1, pp. 22-30, 2002.

[30] R. J. Staba, C. L. Wilson, A. Bragin, I. Fried, and J. Engel, Jr., "Quantitative Analysis of High-Frequency Oscillations (80-500 Hz) Recorded in Human Epileptic Hippocampus and Entorhinal Cortex," *Journal of Neurophysiology*, vol. 88, pp. 1743-1752, 2002.

[31] H. Witte, L. D. Iasemidis, and B. Litt, "Special issue on epileptic seizure prediction," *IEEE Transactions on Biomedical Engineering*, vol. 50, pp. 537-539, 2003.

[32] M. Adjouadi, D. Sanchez, M. Cabrerizo, M. Ayala, P. Jayakar, I. Yaylali, and A. Barreto, "Interictal spike detection using the Walsh transform," *IEEE Transactions on Biomedical Engineering*, vol. 51, pp. 868-872, 2004.

[33] A. Bragin, C. L. Wilson, J. Almajano, I. Mody, and J. Engel, "High-frequency Oscillations after Status Epilepticus: Epileptogenesis and Seizure Genesis," *Epilepsia*, vol. 45, pp. 1017-1023, 2004.

[34] H. Hassanpour, M. Mesbah, and B. Boashash, "EEG spike detection using time-frequency signal analysis," in *Proceedings of IEEE International Conference on Acoustics, Speech, and Signal Processing (ICASSP '04)*, vol. 5, pp. V-421-V-424, 2004.

[35] J. A. Detre and T. F. Floyd, "Functional MRI and Its Applications to the Clinical Neurosciences," *Neuroscientist*, vol. 7, pp. 64-79, 2001.

[36] J. A. Detre and J. Wang, "Technical aspects and utility of fMRI using BOLD and ASL," *Clinical Neurophysiology*, vol. 113, pp. 621-634, 2002.

[37] D. Cohen, "Magnetoencephalography: Evidence of Magnetic Fields Produced by Alpha-Rhythm Currents," *Science*, vol. 161, pp. 784-786, 1968.

[38] J. Parra, S. N. Kalitzin, and F. H. Lopes da Silva, "Magnetoencephalography: an investigational tool or a routine clinical technique?," *Epilepsy & Behavior*, vol. 5, pp. 277-285, 2004.

[39] D. S. Barth, W. Sutherling, J. Engel, and J. Beatty, "Neuromagnetic Localization of Epileptiform Spike Activity in the Human Brain," *Science*, vol. 218, pp. 891-894, 1982.

[40] G. L. Barkley and C. Baumgartner, "MEG and EEG in Epilepsy," *Journal of Clinical Neurophysiology*, vol. 20, pp. 163-178, 2003.

[41] C. Baumgartner, E. Pataraia, G. Lindinger, and L. Deecke, "Neuromagnetic Recordings in Temporal Lobe Epilepsy," *Journal of Clinical Neurophysiology*, vol. 17, pp. 177-189, 2000.

[42] F. S. S. Leijten, G.-J. M. Huiskamp, I. Hilgersom, and A. C. van Huffelen, "High-resolution Source Imaging in Mesiotemporal Lobe Epilepsy: A Comparison Between MEG and Simultaneous EEG," *Journal of Clinical Neurophysiology*, vol. 20, pp. 227-238, 2003.

[43] J. Engel Jr, D. E. Kuhl, M. E. Phelps, and P. H. Crandall, "Comparative localization of epileptic foci in partial epilepsy by PCT and EEG," *Annals of Neurology*, vol. 12, pp. 529-537, 1982.

[44] J. Engel Jr, D. E. Kuhl, M. E. Phelps, and J. C. Mazziotta, "Interictal cerebral glucose metabolism in partial epilepsy and its relation to EEG changes," *Annals of Neurology*, vol. 12, pp. 510-517, 1982.

[45] S. S. Spencer, "The relative contributions of MRI, SPECT, and PET imaging in epilepsy," *Epilepsia*, vol. 35, pp. S72-S89, 1994.

[46] J. E. Desmond, J. M. Sum, A. D. Wagner, J. B. Demb, P. K. Shear, G. H. Glover, J. D. E. Gabrieli, and M. J. Morrell, "Functional MRI measurement of language Lateralization in Wada-tested patients," *Brain*, vol. 118, pp. 1411-1419, 1995.

[47] J. R. Binder, S. J. Swanson, T. A. Hammeke, G. L. Morris, W. M. Mueller, M. Fischer, S. Benbadis, J. A. Frost, S. M. Rao, and V. M. Haughton, "Determination of language dominance using functional MRI: a comparison with the Wada test," *Neurology*, vol. 46, pp. 978-984, 1996.

[48] J. A. Detre, L. Maccotta, D. King, D. C. Alsop, G. Glosser, M. D'Esposito, E. Zarahn, G. K. Aguirre, and J. A. French, "Functional MRI lateralization of memory in temporal lobe epilepsy," *Neurology*, vol. 50, pp. 926-932, 1998.

[49] J. A. Detre, J. I. Sirven, D. C. Alsop, M. J. O'Connor, and J. A. French, "Localization of subclinical ictal activity by functional magnetic resonance imaging: Correlation with invasive monitoring," *Annals of Neurology*, vol. 38, pp. 618-624, 1995.

[50] T. Krings, R. Topper, M. H. T. Reinges, H. Foltys, U. Spetzger, K. H. Chiappa, J. M. Gilsbach, and A. Thron, "Hemodynamic changes in simple partial epilepsy: A functional MRI study," *Neurology*, vol. 54, pp. 524-527, 2000.

[51] R. L. Wolf, D. C. Alsop, I. Levy-Reis, P. T. Meyer, J. A. Maldjian, J. Gonzalez-Atavales, J. A. French, A. Alavi, and J. A. Detre, "Detection of Mesial Temporal Lobe Hypoperfusion in Patients with Temporal Lobe Epilepsy by Use of Arterial Spin Labeled Perfusion MR Imaging," *American Journal of Neuroradiology*, vol. 22, pp. 1334-1341, 2001.

[52] A. Salek-Haddadi, K. J. Friston, L. Lemieux, and D. R. Fish, "Studying spontaneous EEG activity with fMRI," *Brain Research Reviews*, vol. 43, pp. 110, 2003.

[53] S. Warach, J. R. Ives, G. Schlaug, M. R. Patel, D. G. Darby, V. Thangaraj, R. R. Edelman, and D. L. Schomer, "EEG-triggered echo-planar functional MRI in epilepsy," *Neurology*, vol. 47, pp. 89-93, 1996.

[54] M. Seeck, F. Lazeyras, C. M. Michel, O. Blanke, C. A. Gericke, J. Ives, J. Delavelle, X. Golay, C. A. Haenggeli, N. de Tribolet, and T. Landis, "Non-invasive epileptic focus localization using EEG-triggered functional MRI and electromagnetic tomography," *Electroencephalography and Clinical Neurophysiology*, vol. 106, pp. 508-512, 1998.

[55] K. Krakow, F. G. Woermann, M. R. Symms, P. J. Allen, L. Lemieux, G. J. Barker, J. S. Duncan, and D. R. Fish, "EEG-triggered functional MRI of interictal epileptiform activity in patients with partial seizures," *Brain*, vol. 122, pp. 1679-1688, 1999.

[56] M. R. Symms, P. J. Allen, F. G. Woermann, G. Polizzi, K. Krakow, G. J. Barker, D. R. Fish, and J. S. Duncan, "Reproducible localization of interictal epileptiform discharges using EEG-triggered fMRI," *Physics in Medicine and Biology*, vol. 44, pp. N161-N168, 1999.

[57] L. Jäger, K. J. Werhahn, A. Hoffmann, S. Berthold, V. Scholz, J. Weber, S. Noachtar, and M. Reiser, "Focal Epileptiform Activity in the Brain: Detection with Spike-related Functional MR Imaging—Preliminary Results," *Radiology*, vol. 223, pp. 860-869, 2002.

[58] C.-G. Bénar, Y. Aghakhani, Y. Wang, A. Izenberg, A. Al-Asmi, F. Dubeau, and J. Gotman, "Quality of EEG in simultaneous EEG-fMRI for epilepsy," *Clinical Neurophysiology*, vol. 114, pp. 569, 2003.

[59] P. J. Allen, G. Polizzi, K. Krakow, D. R. Fish, and L. Lemieux, "Identification of EEG Events in the MR Scanner: The Problem of Pulse Artifact and a Method for Its Subtraction," *NeuroImage*, vol. 8, pp. 229, 1998.

[60] A. Hoffmann, L. Jäger, K. J. Werhahn, M. Jaschke, S. Noachtar, and M. Reiser, "Electroencephalography during functional echo-planar imaging: Detection of epileptic spikes using post-processing methods," *Magnetic Resonance in Medicine*, vol. 44, pp. 791-798, 2000.

[61] J. Baudewig, H. J. Bittermann, W. Paulus, and J. Frahm, "Simultaneous EEG and functional MRI of epileptic activity: a case report," *Clinical Neurophysiology*, vol. 112, pp. 1196, 2001.

[62] A. Al-Asmi, C.-G. Bénar, D. W. Gross, Y. A. Khani, F. Andermann, B. Pike, F. Dubeau, and J. Gotman, "fMRI Activation in Continuous and Spike-triggered EEG-fMRI Studies of Epileptic Spikes," *Epilepsia*, vol. 44, pp. 1328-1339, 2003.

[63] B. Diehl, A. Salek-Haddadi, D. R. Fish, and L. Lemieux, "Mapping of spikes, slow waves, and motor tasks in a patient with malformation of cortical development using simultaneous EEG and fMRI," *Magnetic Resonance Imaging*, vol. 21, pp. 1167-1173, 2003.

[64] J. Gotman, C.-G. Bénar, and F. Dubeau, "Combining EEG and fMRI in Epilepsy: Methodological Challenges and Clinical Results," *Journal of Clinical Neurophysiology*, vol. 21, pp. 229-240, 2004.

[65] A. P. Bagshaw, Y. Aghakhani, C.-G. Bénar, E. Kobayashi, C. Hawco, F. Dubeau, G. B. Pike, and J. Gotman, "EEG-fMRI of focal epileptic spikes: Analysis with multiple haemodynamic functions and comparison with gadolinium-enhanced MR angiograms," *Human Brain Mapping*, vol. 22, pp. 179-192, 2004.

[66] P. Federico, J. S. Archer, D. F. Abbott, and G. D. Jackson, "Cortical/subcortical BOLD changes associated with epileptic discharges: An EEG-fMRI study at 3 T," *Neurology*, vol. 64, pp. 1125-1130, 2005.

[67] A. Salek-Haddadi, B. Diehl, K. Hamandi, M. Merschhemke, A. Liston, K. Friston, J. S. Duncan, D. R. Fish, and L. Lemieux, "Hemodynamic correlates of epileptiform discharges: An EEG-fMRI study of 63 patients with focal epilepsy," *Brain Research*, vol. 1088, pp. 148-166, 2006.

[68] E. Kobayashi, A. P. Bagshaw, C.-G. Bénar, Y. Aghakhani, F. Andermann, F. Dubeau, and J. Gotman, "Temporal and Extratemporal BOLD Responses to Temporal Lobe Interictal Spikes," *Epilepsia*, vol. 47, pp. 343-354, 2006.

[69] U. Lengler, I. Kafadar, B. A. Neubauer, and K. Krakow, "fMRI correlates of interictal epileptic activity in patients with idiopathic benign focal epilepsy of childhood: A simultaneous EEG-functional MRI study," *Epilepsy Research*, vol. 75, pp. 29-38, 2007.

[70] J. S. Archer, D. F. Abbott, A. B. Waites, and G. D. Jackson, "fMRI "deactivation" of the posterior cingulate during generalized spike and wave," *NeuroImage*, vol. 20, pp. 1915-1922, 2003.

[71] Y. Aghakhani, A. P. Bagshaw, C. G. Bénar, C. Hawco, F. Andermann, F. Dubeau, and J. Gotman, "fMRI activation during spike and wave discharges in idiopathic generalized epilepsy," *Brain*, vol. 127, pp. 1127-1144, 2004.

[72] K. Hamandi, A. Salek-Haddadi, H. Laufs, A. Liston, K. Friston, D. R. Fish, J. S. Duncan, and L. Lemieux, "EEG-fMRI of idiopathic and secondarily generalized epilepsies," *NeuroImage*, vol. 31, pp. 1700-1710, 2006.

[73] H. Laufs, U. Lengler, K. Hamandi, A. Kleinschmidt, and K. Krakow, "Linking Generalized Spike-and-Wave Discharges and Resting State Brain Activity by Using EEG/fMRI in a Patient with Absence Seizures," *Epilepsia*, vol. 47, pp. 444-448, 2006.

[74] X. Zhao, D. Glahn, L. H. Tan, N. Li, J. Xiong, and J.-H. Gao, "Comparison of TCA and ICA techniques in fMRI data processing," *Journal of Magnetic Resonance Imaging*, vol. 19, pp. 397-402, 2004.

[75] V. L. Morgan, J. C. Gore, and B. Abou-Khalil, "Cluster analysis detection of functional MRI activity in temporal lobe epilepsy," *Epilepsy Research*, vol. 76, pp. 22-33, 2007.

[76] V. L. Morgan, Y. Li, B. Abou-Khalil, and J. C. Gore, "Development of 2dTCA for the detection of irregular, transient bold activity," *Human Brain Mapping (online)*, 2007.

[77] V. L. Morgan, R. R. Price, A. Arain, P. Modur, and B. Abou-Khalil, "Resting functional MRI with temporal clustering analysis for localization of epileptic activity without EEG," *NeuroImage*, vol. 21, pp. 473-481, 2004.

[78] Y. Liu, J.-H. Gao, H.-L. Liu, and P. T. Fox, "The temporal response of the brain after eating revealed by functional MRI," *Nature*, vol. 405, pp. 1058-1062, 2000.

[79] S.-H. Yee and J.-H. Gao, "Improved detection of time windows of brain responses in fMRI using modified temporal clustering analysis," *Magnetic Resonance Imaging*, vol. 20, pp. 17-26, 2002.

[80] J.-H. Gao and S.-H. Yee, "Iterative temporal clustering analysis for the detection of multiple response peaks in fMRI," *Magnetic Resonance Imaging*, vol. 21, pp. 51-53, 2003.

[81] K. Hamandi, A. Salek Haddadi, A. Liston, H. Laufs, D. R. Fish, and L. Lemieux, "fMRI temporal clustering analysis in patients with frequent interictal epileptiform discharges: Comparison with EEG-driven analysis," *NeuroImage*, vol. 26, pp. 309-316, 2005.

[82] S. T. Herman, T. S. Walczak, and C. W. Bazil, "Distribution of partial seizures during the sleep-wake cycle: Differences by seizure onset site," *Neurology*, vol. 56, pp. 1453-1459, 2001.

[83] G. K. Aguirre, E. Zarahn, and M. D'Esposito, "The Variability of Human, BOLD Hemodynamic Responses," *NeuroImage*, vol. 8, pp. 360-369, 1998.

[84] H.-L. Liu, Y. Pu, L. D. Nickerson, Y. Liu, P. T. Fox, and J.-H. Gao, "Comparison of the temporal response in perfusion and BOLD-based event-related functional MRI," *Magnetic Resonance in Medicine*, vol. 43, pp. 768-772, 2000.

[85] D. A. Handwerker, J. M. Ollinger, and M. D'Esposito, "Variation of BOLD hemodynamic responses across subjects and brain regions and their effects on statistical analyses," *NeuroImage*, vol. 21, pp. 1639-1651, 2004.

[86] K. J. Friston, P. Jezzard, and R. Turner, "Analysis of functional MRI time-series," *Human Brain Mapping*, vol. 1, pp. 153-171, 1994.

[87] G. M. Boynton, S. A. Engel, G. H. Glover, and D. J. Heeger, "Linear Systems Analysis of Functional Magnetic Resonance Imaging in Human V1," *Journal of Neuroscience*, vol. 16, pp. 4207-4221, 1996.

[88] J. Kim, J. Whyte, J. Wang, H. Rao, K. Z. Tang, and J. A. Detre, "Continuous ASL perfusion fMRI investigation of higher cognition: Quantification of tonic CBF changes during sustained attention and working memory tasks," *NeuroImage*, vol. In Press, Corrected Proof, 2005.

[89] B. A. Ardekani, A. H. Bachman, and J. A. Helpern, "A quantitative comparison of motion detection algorithms in fMRI," *Magnetic Resonance Imaging*, vol. 19, pp. 959-963, 2001.

[90] K. J. Friston, J. Ashburner, C. D. Frith, J. B. Poline, J. D. Heather, and R. S. J. Frackowiak, "Spatial registration and normalization of images," *Human Brain Mapping*, vol. 3, pp. 165-189, 1995.

[91] K. J. Friston, S. Williams, R. Howard, R. S. J. Frackowiak, and R. Turner, "Movement-related effects in fMRI time-series," *Magnetic Resonance in Medicine*, vol. 35, pp. 346-355, 1996.

[92] H. Gudbjartsson and S. Patz, "The rician distribution of noisy MRI data," *Magnetic Resonance in Medicine*, vol. 34, pp. 910-914, 1995.

[93] A. M. Wink and J. B. T. M. Roerdink, "BOLD Noise Assumptions in fMRI," *International Journal of Biomedical Imaging*, vol. 2006, Article ID 12014, pp. 1-11, 2006.

[94] R. D. Nowak, "Wavelet-based Rician noise removal for magnetic resonance imaging," *Image Processing, IEEE Transactions on*, vol. 8, pp. 1408-1419, 1999.

[95] D. R. Pickens, Y. Li, V. L. Morgan, and B. M. Dawant, "Development of computer-generated phantoms for FMRI software evaluation," *Magnetic Resonance Imaging*, vol. 23, pp. 653-663, 2005.

[96] P. Perona and J. Malik, "Scale-space and edge detection using anisotropic diffusion," *Pattern Analysis and Machine Intelligence, IEEE Transactions on*, vol. 12, pp. 629-639, 1990.

[97] G. Gerig, O. Kubler, R. Kikinis, and F. A. Jolesz, "Nonlinear anisotropic filtering of MRI data," *Medical Imaging, IEEE Transactions on*, vol. 11, pp. 221-232, 1992.

[98] A. Pižurica, W. Philips, I. Lemahieu, and M. Acheroy, "A versatile wavelet domain noise filtration technique for medical imaging," *IEEE Transactions on Medical Imaging*, vol. 22, pp. 323-331, 2003.

[99] J. Wang, Y. Zhang, R. L. Wolf, A. C. Roc, D. C. Alsop, and J. A. Detre, "Amplitude-modulated Continuous Arterial Spin-labeling 3.0-T Perfusion MR Imaging with a Single Coil: Feasibility Study," *Radiology*, vol. 235, pp. 218-228, 2005.

[100] R. Duda, P. Hart, and D. Stork, *Pattern Classification*, 2nd ed. New York: Wiley-Interscience, 2001.

[101] R. Esteller, J. Echauz, T. Tcheng, B. Litt, and B. Pless, "Line length: An efficient feature for seizure onset detection," in *Proceedings of the 23th Annual International Conference of the IEEE Engineering in Medicine and Biology Society 2001*, pp. 1707-1710, 2001.

[102] R. Esteller, G. Vachtsevanos, J. Echauz, T. Henry, P. Pennell, C. Epstein, R. Bakay, C. Bowen, and B. Litt, "Fractal dimension characterizes seizure onset in epileptic patients," in *Proceedings IEEE International Conference on Acoustics, Speech, and Signal Processing 1999*, vol. 4, pp. 2343 – 2346, 1999.

[103] M. D'Alessandro, R. Esteller, G. Vachtsevanos, A. Hinson, J. Echauz, and B. Litt, "Epileptic seizure prediction using hybrid feature selection over multiple intracranial EEG electrode contacts: a report of four patients," *Biomedical Engineering, IEEE Transactions on*, vol. 50, pp. 603-615, 2003.

[104] E. N. Bruce, *Biomedical Signal Processing and Signal Modeling*. New York: Wiley, 2001.

[105] R. Esteller, G. Vachtsevanos, J. Echauz, and B. Litt, "A comparison of waveform fractal dimension algorithms," *Circuits and Systems I: Fundamental Theory and Applications, IEEE Transactions on [see also Circuits and Systems I: Regular Papers, IEEE Transactions on]*, vol. 48, pp. 177-183, 2001.

[106] M. J. Katz, "Fractals and the analysis of waveforms," *Computers in Biology and Medicine*, vol. 18, pp. 145-156, 1988.

[107] X.-S. Zhang, Y.-S. Zhu, N. V. Thakor, and Z.-Z. Wang, "Detecting ventricular tachycardia and fibrillation by complexity measure," *IEEE Transactions on Biomedical Engineering*, vol. 46, pp. 548-555, 1999.

[108] P. Somol, P. Pudil, and J. Kittler, "Fast branch & bound algorithms for optimal feature selection," *Pattern Analysis and Machine Intelligence, IEEE Transactions on*, vol. 26, pp. 900-912, 2004.

[109] J. R. Koza, *Genetic Programming: On Programming of Computers by Means of Natural Selection*. Cambridge, MA: MIT Press, 1992.

[110] W. Banzhaf, P. Nordin, R. E. Keller, and F. D. Francone, *Genetic Programming: An Introduction: On the Automatic Evolution of Computer Programs and Its Applications*. San Francisco, CA: Morgan Kaufmann Publishers, Inc., 1998.

[111] N. Tzourio-Mazoyer, B. Landeau, D. Papathanassiou, F. Crivello, O. Etard, N. Delcroix, B. Mazoyer, and M. Joliot, "Automated Anatomical Labeling of Activations in SPM Using a Macroscopic Anatomical Parcellation of the MNI MRI Single-Subject Brain," *NeuroImage*, vol. 15, pp. 273-289, 2002.

[112] J. A. Maldjian, P. J. Laurienti, R. A. Kraft, and J. H. Burdette, "An automated method for neuroanatomic and cytoarchitectonic atlas-based interrogation of fMRI data sets," *NeuroImage*, vol. 19, pp. 1233-1239, 2003.

[113] J. A. Maldjian, P. J. Laurienti, and J. H. Burdette, "Precentral gyrus discrepancy in electronic versions of the Talairach atlas," *NeuroImage*, vol. 21, pp. 450-455, 2004.

[114] L. Zelnik-Manor and P. Perona, "Self-tuning spectral clustering," *Advances in Neural Information Processing Systems*, vol. 17, 2004.

[115] T. Nichols and S. Hayasaka, "Controlling the familywise error rate in functional neuroimaging: a comparative review," *Statistical Methods in Medical Research*, vol. 12, pp. 419-446, 2003.